

5-2019

Local and Central Controllers for Microgrids

Edgar Ariel Escala Calame
University of Arkansas, Fayetteville

Follow this and additional works at: <https://scholarworks.uark.edu/etd>



Part of the [Controls and Control Theory Commons](#), and the [Power and Energy Commons](#)

Recommended Citation

Escala Calame, Edgar Ariel, "Local and Central Controllers for Microgrids" (2019). *Theses and Dissertations*. 3193.
<https://scholarworks.uark.edu/etd/3193>

This Thesis is brought to you for free and open access by ScholarWorks@UARK. It has been accepted for inclusion in Theses and Dissertations by an authorized administrator of ScholarWorks@UARK. For more information, please contact ccmiddle@uark.edu.

Local and Central Controllers for Microgrids

A thesis submitted in partial fulfillment
of the requirements for the degree of
Master of Science in Electrical Engineering

by

Edgar Ariel Escala Calame
University of Arkansas
Bachelor of Science in Electrical Engineering, 2016

May 2019
University of Arkansas

This thesis is approved for recommendation to the Graduate Council.

Juan Carlos Balda, Ph.D.
Thesis Director

Roy A. McCann, Ph.D.
Committee Member

Simon Ang, Ph.D.
Committee Member

ABSTRACT

The main objective of this thesis is to serve as a guide, so readers are able to learn about microgrids and to design simple controllers for different AC microgrid applications. In addition, this thesis has the objective to provide examples of simulation cases for the hierarchical structure of a basic AC microgrid which can be used as a foundation to build upon, and achieve more complex microgrid structures as well as more sophisticated power-converter control techniques.

To achieve these objectives, the modeling of voltage source converters and control design in the z-domain are presented. Moreover, the implementation and transient analysis of the power-converter operating modes are executed through MATLAB/SimulinkTM simulations. Then, an energy management case for the central controller of the AC microgrid is performed utilizing real-time simulation tools, Typhoon HIL software and hardware devices in addition to Texas instruments digital signal processors as local controllers.

ACKNOWLEDGMENTS

First of all, I would like to express my gratitude to God for giving me the strength and wisdom to continue forward each day.

I would also like to thank my advisor Dr. Juan Carlos Balda for giving me the opportunity to further my Electrical Engineering knowledge and for all his time, support and guidance. Also, I would like to thank Dr. Roy McCann and Dr. Simon Ang for being part of my thesis committee.

I am especially grateful to Vinson Jones for his endless patience and excellent guidance. I would also like to show my gratitude to David Carballo, Waleed Alhosaini, Dr. Sebastian Gomez and Dr. Roberto Carballo for their collaboration and support in the microgrid project. Finally, I would like to thank my friends and fellow lab mates Rafael Franceschi, Luciano García, Obaid Aldosari, Tyler Adamson and Hazzaz Mahmud for their support and motivation.

DEDICATION

This thesis is dedicated to my beloved parents, Edgar Enrique Escala Castillo and Elvira Maritza Calame de Escala, to all my family members and friends who were always there for me and provided unconditional love and support in the pursuit of this academic achievement.

TABLE OF CONTENTS

CHAPTER 1

INTRODUCTION	1
1.1. Microgrids and Power Systems	1
1.2. Hierarchical Microgrid Control	4
1.3. Thesis Objectives	10
1.4. Thesis Organization	11
1.5. References	12

CHAPTER 2

MODELING OF VOLTAGE SOURCE CONVERTERS AND CONTROL DESIGN IN THE S-DOMAIN

2.1. Introduction	14
2.2. Modeling of Two-Level Grid-Connected VSC with LC Filter	14
2.3. Space Vector Pulse Width Modulation	15
2.4. Direct-Quadrature-Zero Synchronous Reference Frame	20
2.5. Synchronous Frame Phase Lock Loop Design in the S-Domain	23
2.6. Current Control Loop Design in the S-Domain	27
2.7. Active/Reactive Power Reference Derivation	32
2.8. DC Bus Voltage Control Loop Design in the S-Domain	35
2.9. AC Voltage Control Loop Design in the S-Domain	40
2.10. Concluding Remarks	46
2.11. References	46

CHAPTER 3

CONTROL DESIGN IN THE Z-DOMAIN

3.1.	Introduction	48
3.2.	Synchronous Frame Phase Lock Loop in the Z-Domain	48
3.3.	Current Control Loop Design in the Z-Domain	54
3.4.	DC-Bus Voltage Control Loop Design in the Z-Domain	62
3.5.	AC Voltage Control Loop Discrete Design in the Z-Domain	69
3.6.	Concluding Remarks	76
3.7.	References	76

CHAPTER 4

MICROGRID PRIMARY AND SECONDARY CONTROLLERS

4.1.	Introduction	77
4.2.	Grid-Feeding Mode	78
4.2.1.	PQ Open-loop Control	78
4.2.2.	DC Voltage Regulator Control	81
4.3.	Grid-Forming Mode	85
4.4.	Grid-Supporting Mode	87
4.4.1.	Current Source	90
4.4.2.	Voltage Source	91
4.5.	Volt/VAR Control	95
4.6.	Concluding Remarks	100
4.7.	References	101

CHAPTER 5

MICROGRID CENTRAL CONTROLLER

5.1.	Introduction	103
5.2.	Tertiary Control Layer	104
5.3.	Central Controller Implementation	106
5.4.	Concluding Remarks	111
5.5.	References	112

CHAPTER 6

CONCLUSION AND RECOMMENDATIONS FOR FUTURE WORK

6.1.	Conclusions	114
6.2.	Recommendations for Future Work	115
6.3.	References	116

CHAPTER 1

INTRODUCTION

1.1 Microgrids and Power Systems

Electricity has become vital for the modern society due to its important role in the operation of its many applications such as lighting, heating, communication and powering of everyday devices that have shaped the way we live and do things. Traditional electrical power systems have delivered the energy consumed by all these devices for over one hundred years since the first electric power station, Pearl Street Electric Station, went into operation in 1882 [1]. Consequently, reliability, resiliency, security and power quality are fundamental factors in electrical power systems due to high dependence and growing demand of electricity by our modern society [2].

Traditional power systems can be divided into three main areas: generation, transmission and distribution which are connected by power substations. The generation is done usually far away from the point of consumption, so a transformer is used to step up the voltage to reduce the losses in the transmission system which then connects to distributions systems that step down the voltage and deliver the electric power to industrial, commercial and residential consumers at their respective voltage levels [3]. Moreover, conventional electric power systems make use of few active equipment such as static synchronous compensators and static var compensators; hence, it is thought as a passive system with unidirectional power flows. This fact raises concerns regarding reliability and resiliency due to unexpected outages, mayor disruptions or natural disasters [4].

Consequently, traditional electric power systems are facing continuous and rapid changes to alleviate environmental concerns, respond to growing consumer demands, and address governmental incentives that aim to mitigate these problems, converting these systems from unidirectional power flows to bidirectional ones by having more active components. The notion of the smart grid has recently emerged to introduce an intelligent electric network with improved reliability and sustainability [5]. Thus, electricity will be delivered from suppliers to consumers using digital technology to control consumers loads to save energy using the concept of microgrids as its building block, thus reducing cost and increasing reliability. This concept has been developed to manage the increasing penetration of Distributed Energy Resources (DERs), and empower final users with the ability to generate, store, control, and manage part of their energy consumption.

Microgrids are small groupings that connect distributed generation (DG), energy storage, power distribution lines and local loads with control technologies that can operate connected or disconnected from the main grid. Hence, microgrids allow bidirectional flows of electricity with the main distribution network, making the whole system active. Furthermore, this integration of DG which is mainly based on renewables that can reduce the transmission and distribution losses faced by the traditional power systems.

Microgrids have two main modes of operation: grid connected and island mode. In the first one, the microgrid imports or exports power from or to the main grid. In the case of a disruption in the main grid, the microgrid switches over to the island mode and supplies power to the loads based on priority. Additionally, microgrids can be classified in two types; on the one hand, distribution microgrids that comprise medium voltage lines that can extend for many miles such as neighborhood, a military base or an industrial park. On the other hand, facility or low-

voltage microgrids that cover smaller areas such as a house, one building or a group of buildings close to each other [6].

Fig 1.1 illustrates an AC microgrids that is connected to the main power grid at the point of common coupling (PCC) where a circuit breaker can be used to disconnect the microgrid from the grid for island operation. Since microgrids make renewable, storage, and efficient technologies more attractive by integrating them into a unified energy system, a variety of fuel and energy sources can be used to make the system more flexible and efficient when supplying non-critical and critical loads in case of emergency. Moreover, power electronics interfaces are usually integrated between certain DERs and the rest of the microgrid, making the ac-dc converter the fundamental power interface in DG as well as the critical element for reliable control of microgrid systems.

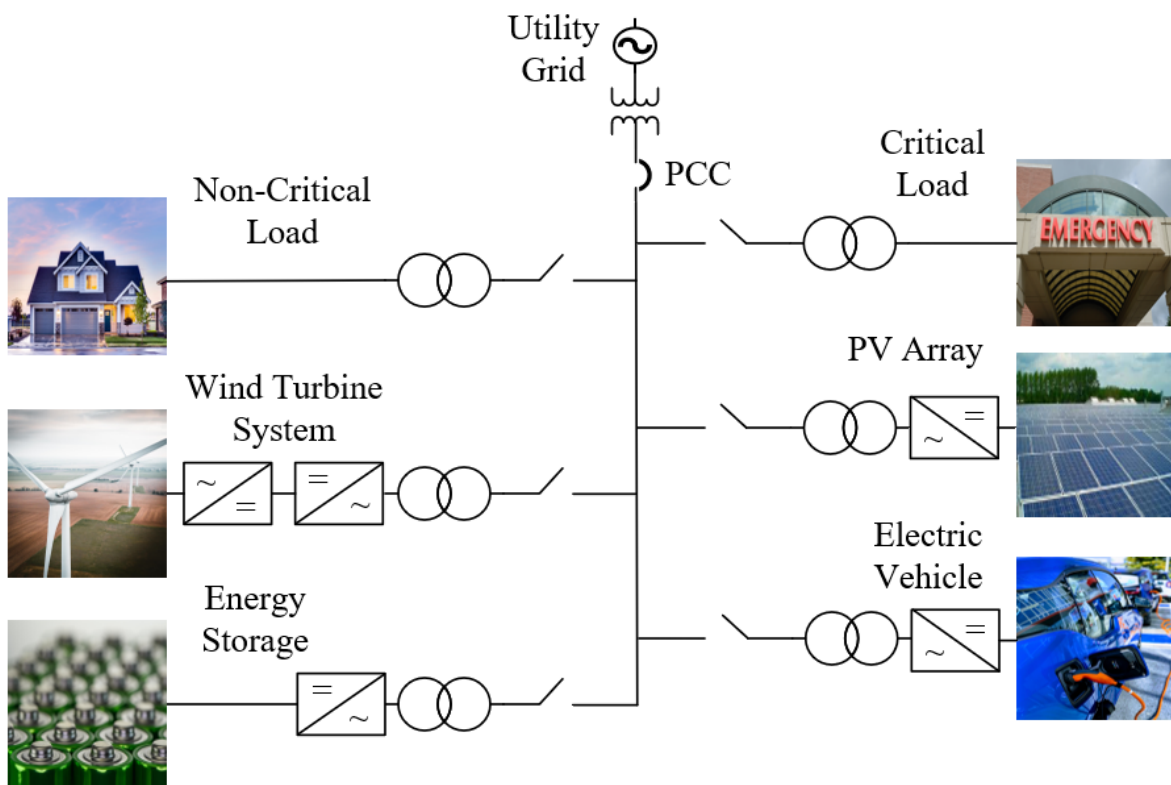


Figure 1.1: A typical AC microgrid structure

1.2 Hierarchical Microgrid Control

Microgrids can be very complex systems just as the main grid; hence, proper control and coordination of its components is required for stable and efficient operation. Thus, a microgrid becomes a single controlled aggregated system of many DGs that can interact with the main grid and turns out to be a fundamental component in the implementation of the smart grid to ensure reliability, security, power quality and energy output [7]. The microgrid control structure must be in charge of the following functions [5]:

- Frequency and voltage regulation in both operating modes;
- Microgrid resynchronization with the main grid;
- DER coordination for proper load sharing techniques;
- Power flow control between the microgrid and the main grid;
- Economical optimization of microgrid resources.

A hierarchical control structure is implemented to address each of these functions. This strategy divides the microgrid control into three layers: primary, secondary and tertiary controllers as presented in Fig. 1.2. The primary control layer is in charge of regulating locally low-level variables such as frequency, power and voltage output of DC/AC converters to the microgrid. Additionally, it implements load sharing techniques that are crucial when communication from higher control layers is lost or the microgrid switches from one operating mode to another one.

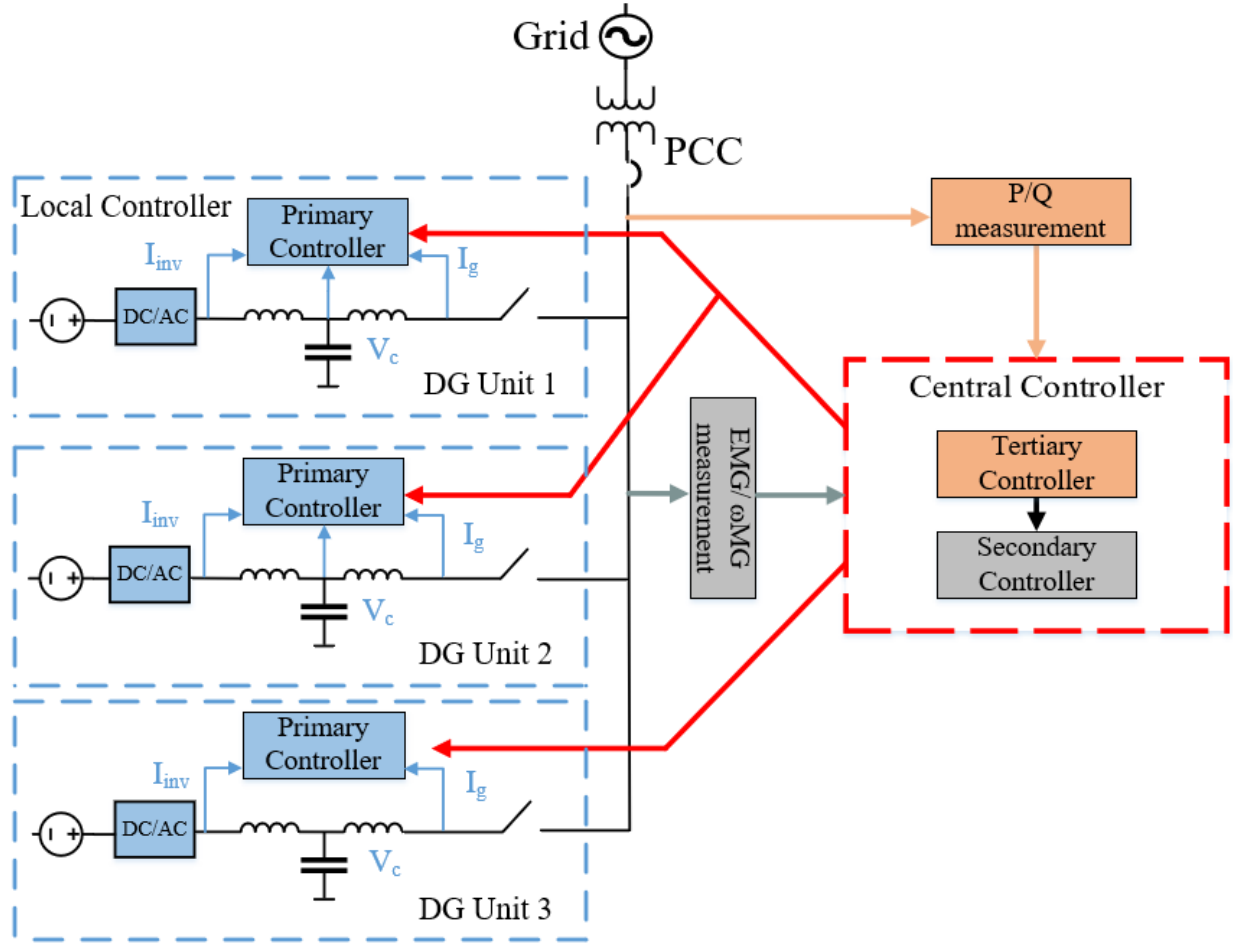


Figure 1.2: Hierarchical Microgrid Control

Alternatively, the secondary control layer is responsible for compensating the steady-state error produced by the primary controllers and ensuring that all points along the microgrid are within the required frequency and voltage margins which include the task of transition between grid-connected and island modes. Lastly, the tertiary control layer deals with the power flow between the microgrid and the main grid as well as the economical optimization of the microgrid operation [8].

These roles are of different significances and time scales, so local and centralized controllers are implemented to address each task in different control layers. The local controller implements the primary control layer of a single DG unit depending on its operation mode, role

in the microgrid and DER control technique. Thus, this controller manages the power flows of the DG unit autonomously by using Maximum Power Point Tracking, energy storage management method or load sharing techniques being its time response in the range of milliseconds. Otherwise, the local controller receives power flow commands from the central controller for power quality or economical optimization purposes [6]. The primary controller is also in charge of the “zero level control” that comprises the power converter control with respect of local variables such as current, frequency and voltage. There are many control methods for the regulation of local variables, some of the most common controllers are presented in Fig. 1.3. The converter control techniques can be classified into linear and non-linear ones [9,10].

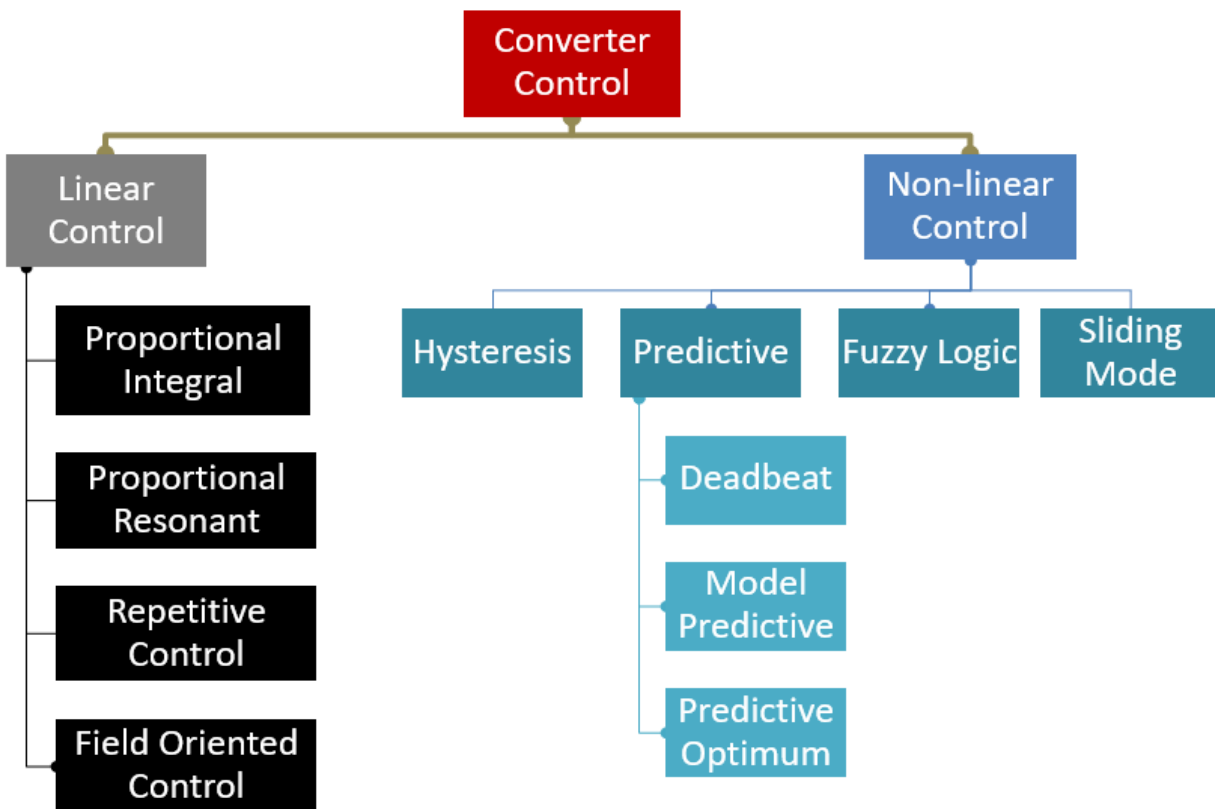


Figure 1.3: Power Converter Control Techniques

Among the linear controllers, the proportional-integral (PI) and the proportional-resonant (PR) controller can be highlighted since there are some of the most popular controllers [11,12]. On one hand, the PI controller is low-bandwidth linear that can be used to guarantee null steady-state error with acceptable performance. As a consequence, the control variables are required to be dc signals which remarkably facilitates the compensator design, especially in variable-frequency scenarios, and independent control of active and reactive power injections. However, a synchronous reference transformation is required to achieve these DC constants with the help of phase and angle information obtained from the control variables, which are time-varying waveforms that lead to difficulties in achieving zero steady-state error [13]. On the other hand, the PR controller has gained a large popularity in the last decade due to its capability of eliminating the steady-state error when regulating sinusoidal signals due to its infinite gain at the resonant frequency which is designed to be the same as that of the control signals [9]. Moreover, this controller allows a straightforward implementation of a harmonic compensator for low-order harmonics without disrupting its controller dynamics [11].

Some of the nonlinear control structures such as those based on hysteresis, sliding, or predictive controllers, can be also used to control power converters that require fast and robust tracking of sinusoidal currents [10,12]. Hysteresis control is a simple method that controls the output current by comparing the control variable with a reference signal with an error width called hysteresis band. Therefore, this robust and straightforward technique changes the switching state of the converter every time the current reaches any of the boundaries of the hysteresis band [14].

Predictive control comprises a very wide family of controllers with very different approaches such as hysteresis based, trajectory based, model predictive control, predictive optimum control and deadbeat control [15-16]. The main ideas behind predictive control is the use of a model of the system for calculating predictions of the future behavior of the controlled variables, and the use of an optimization criterion for selecting the proper actuation [12]. One of the most common predictive control schemes is deadbeat control, which uses a model of the system to calculate the voltage that makes the error zero in one sample time. Therefore, this controller has been proven to have superior performance in limiting the peak current for sudden power variation in the case of voltage sags due to grid faults than other controllers such as PI and PR [11]. However, the deadbeat controller is very sensitive to model and parameter mismatches.

Fuzzy logic control is a heuristic approach that combines the knowledge of experimentation and key elements of human thinking in the design of nonlinear controllers [17]. These considerations are implemented in a systematic form to compensate the inability of the classic control theory for covering complex systems with uncertainties and inaccuracies, presenting greater disturbance insensitivity than most nonlinear controllers. Fuzzy logic controllers are based on fuzzy sets, which are a collection of objects that have partial membership in a set, making the transition from membership to nonmembership smooth rather than abrupt. Therefore, boundaries of fuzzy sets can be vague and ambiguous, making them useful for approximation models in complex, nonlinear, or undefined systems for which a good practical knowledge exists [18]. However, fuzzy controller might be difficult to implement and if a control task can be accomplished with a PI or some equally simple controller, that controller should be used instead of a fuzzy one [17].

Sliding mode control is a nonlinear regulator method that alters the dynamics of a system with a high-frequency variable switching control as a form of variable structure control to force the system to slide along a cross-section of different control behaviors. This achieves the inherent robustness capability of system order reduction, and suitability to the on/off switching of the power converter [19]. Since sliding mode control laws are not continuous, it has the ability to drive trajectories toward an adjacent region with a different control structures so the ultimate trajectory will not lie completely within one control structure and the transition can be achieved smoothly in a finite time. [20]. Even though there is a wide variety of more complex and higher performance controller techniques than the PI, the PI is one of the most common and simple controllers used for the control of power converters. Therefore, there is a substantial amount of research papers, books and application notes on the implementation of this controller in microgrid applications. The PI-based control technique has been chosen to design the primary controllers developed in this thesis.

The central controller executes the overall control of the microgrid as a single entity and uses a SCADA interface to oversee microgrid operation, having a control response in the range of seconds and minutes. This includes microgrid local balance, import and export control, technical performance maintenance and emission level monitoring [2]. The secondary and tertiary control layers can be implemented in a central controller because it receives the most critical measurement signals for proper microgrid operation. This is suitable to provide acceptable power quality and economic optimization by setting the references for active and reactive powers of the local controllers of all DG units connected to the microgrid. The central controller is also in charge of controlling the protection devices of the microgrid to ensure correct protection to the grid faults and loss of grid scenarios [7].

The main tasks of the central controller in the grid-connected operating mode are summarized as follows [21]:

- Ensuring synchronized operation with the main grid;
- Monitoring system diagnostics by collecting information from the DG units and loads;
- Performing state estimation and security assessment evaluation, economic generation
- scheduling and active and reactive power control;

Moreover, the tasks of the central controller in the island mode are as follows [21]:

- Frequency and voltage regulation at all points of the microgrid by adjusting active and reactive power control of the DG units;
- Adapting load-shedding strategies using demand-side management with storage device support for maintaining power balance;
- Initiation of a local black start to ensure improved reliability and continuity of service;
- Switching the microgrid back to grid-connected mode after main grid supply is restored without hindering the stability of either grid;

Finally, it must be noted that the whole hierarchical microgrid structure can be implemented in a decentralized manner as done in [22-25].

1.3 Thesis Objectives

The main objective of this thesis is to serve as a guide, so readers are able to learn about microgrids and design simple controllers for different microgrid applications in both operating modes. Another objective of this thesis is to provide examples of simulation cases for the hierarchical structure of a basic AC microgrid which can be used as a starting point in the control of microgrid field. Consequently, this thesis can be used a foundation to build upon and achieve

more complex microgrid structures and more sophisticated power-converter control techniques as the ones mentioned in section 1.2.

1.4 Thesis Organization

This thesis is divided into six chapters organized as follows:

- Chapter 2: Modeling of Voltage Source Converters and Control Design in the s-domain - The fundamental circuit model of the DC/AC converter and associated LC filter are reviewed. The Space Vector Pulse Width Modulation technique and the reference frame theory are presented. Also, the design of a PI controller in the s-domain for current and voltage loops is derived.
- Chapter 3: Control Design in the Z-domain - The design of PI controller in the z-domain for current and voltage loops is derived. A step response comparison between the s-domain and z-domain control design is performed.
- Chapter 4: Microgrid Primary and Secondary Controllers – The implementation of the primary controller for different AC microgrid applications and a secondary control case are presented.
- Chapter 5: Microgrid Central Controller – The implementation of a real-time hardware-in-the-loop simulation of an AC microgrid with a central controller is addressed.
- Chapter 6: Conclusion and Recommendations for Future Work – The conclusions of this thesis and recommendations for future work are presented.

1.5 References

- [1] T. Gonen, "Chapter 1: Distribution System Planning and Automation," in *Electric Power Distribution Engineering*, New York: CRC Press, 2014.
- [2] Nikos Hatziaargyriou, "The Microgrids Concept," in *Microgrids: Architectures and Control*, IEEE, 2014.
- [3] X. Yu, C. Cecati, T. Dillon and M. G. Simões, "The New Frontier of Smart Grids," in *IEEE Industrial Electronics Magazine*, vol. 5, no. 3, pp. 49-63, Sept. 2011.
- [4] Haitham Abu-Rub; Mariusz Malinowski; Kamal Al-Haddad, "An Overview on Distributed Generation and Smart Grid Concepts and Technologies," in *Power Electronics for Renewable Energy Systems, Transportation and Industrial Applications*, IEEE, 2014.
- [5] A. Bidram and A. Davoudi, "Hierarchical Structure of Microgrids Control System," in *IEEE Transactions on Smart Grid*, vol. 3, no. 4, pp. 1963-1976, Dec. 2012.
- [6] T. L. Vandoorn, J. C. Vasquez, J. De Kooning, J. M. Guerrero and L. Vandevelde, "Microgrids: Hierarchical Control and an Overview of the Control and Reserve Management Strategies," in *IEEE Industrial Electronics Magazine*, vol. 7, no. 4, pp. 42-55, Dec. 2013.
- [7] T. Gönen, "Chapter 13: Distributed Generation and Renewable Energy," in *Electric power distribution engineering*, New York: CRC Press, 2014.
- [8] J. Rocabert, A. Luna, F. Blaabjerg and P. Rodríguez, "Control of Power Converters in AC Microgrids," in *IEEE Transactions on Power Electronics*, vol. 27, no. 11, pp. 4734-4749, Nov. 2012.
- [9] Remus Teodorescu; Marco Liserre; Pedro Rodriguez, "Grid Current Control," in *Grid Converters for Photovoltaic and Wind Power Systems*, IEEE, 2007.
- [10] M. P. Kazmierkowski and L. Malesani, "Current control techniques for three-phase voltage-source PWM converters: a survey," in *IEEE Transactions on Industrial Electronics*, vol. 45, no. 5, pp. 691-703, Oct. 1998.
- [11] A. Timbus, M. Liserre, R. Teodorescu, P. Rodriguez and F. Blaabjerg, "Evaluation of Current Controllers for Distributed Power Generation Systems," in *IEEE Transactions on Power Electronics*, vol. 24, no. 3, pp. 654-664, March 2009.
- [12] Jose Rodriguez; Patricio Cortes, "Introduction," in *Predictive Control of Power Converters and Electrical Drives*, IEEE, 2012.

- [13] B. Bahrani, S. Kenzelmann and A. Rufer, "Multivariable-PI-Based dq-Current Control of Voltage Source Converters with Superior Axis Decoupling Capability," in *IEEE Transactions on Industrial Electronics*, vol. 58, no. 7, pp. 3016-3026, July 2011.
- [14] Jose Rodriguez; Patricio Cortes, "Classical Control Methods for Power Converters and Drives," in *Predictive Control of Power Converters and Electrical Drives*, IEEE, 2012.
- [15] P. Cortes, M. P. Kazmierkowski, R. M. Kennel, D. E. Quevedo and J. Rodriguez, "Predictive Control in Power Electronics and Drives," in *IEEE Transactions on Industrial Electronics*, vol. 55, no. 12, pp. 4312-4324, Dec. 2008.
- [16] Jose Rodriguez; Patricio Cortes, " Model Predictive Control," in *Predictive Control of Power Converters and Electrical Drives*, IEEE, 2012.
- [17] John H. Lilly, "Introduction," in *Fuzzy Control and Identification*, IEEE, 2010.
- [18] M. H. Rashid, "Advanced Control of Switching Power Converters: Fuzzy Logic Control of Switching Converters," in *Power electronics handbook: devices, circuits, and applications*, 3rd ed., Burlington, MA: Butterworth-Heinemann, 2011.
- [19] M. H. Rashid, "Advanced Control of Switching Power Converters: Sliding-Mode Control of Switching Converters," in *Power electronics handbook: devices, circuits, and applications*, 3rd ed., Burlington, MA: Butterworth-Heinemann, 2011.
- [20] Yu Zhang and Zhenhua Jiang, "Sliding mode based zero-sequence current mitigation of parallel-connected power converters," *2009 IEEE International Electric Machines and Drives Conference*, Miami, FL, 2009, pp. 1658-1663.
- [21] S. Chowdhury, S. P. Chowdhury and P. Crossley, "Chapter 4: Microgrid and active distribution network management system," in *Microgrids and active distribution networks*, London: Institution of Engineering and Technology, 2009.
- [22] K. De Brabandere, K. Vanthournout, J. Driesen, G. Deconinck and R. Belmans, "Control of Microgrids," *2007 IEEE Power Engineering Society General Meeting*, Tampa, FL, 2007, pp. 1-7.
- [23] A. Bani-Ahmed, A. Nasiri and H. Hosseini, "Design and development of a true decentralized control architecture for microgrid," *2016 IEEE Energy Conversion Congress and Exposition (ECCE)*, Milwaukee, WI, 2016, pp. 1-5.
- [24] J. M. Guerrero, M. Chandorkar, T. Lee and P. C. Loh, "Advanced Control Architectures for Intelligent Microgrids—Part I: Decentralized and Hierarchical Control," in *IEEE Transactions on Industrial Electronics*, vol. 60, no. 4, pp. 1254-1262, April 2013.
- [25] A. Vaccaro, V. Loia, G. Formato, P. Wall and V. Terzija, "A Self-Organizing Architecture for Decentralized Smart Microgrids Synchronization, Control, and Monitoring," in *IEEE Transactions on Industrial Informatics*, vol. 11, no. 1, pp. 289-298, Feb. 2015.

CHAPTER 2

MODELING OF VOLTAGE SOURCE CONVERTERS AND CONTROL DESIGN IN THE S-DOMAIN

2.1 Introduction

The ac-dc converter is the fundamental power interface between a distributed energy resources (DERs) and a microgrid as well as the critical element for reliable microgrid systems. This chapter reviews the fundamental circuit model of the voltage source converter (VSC) with an output LC filter. The necessary background knowledge to operate the VSC as an active rectifier with DC bus control and as an inverter in grid-feeding and grid-forming modes utilizing the different control loops. Space vector pulse width modulation (SVPWM), Direct-quadrature-zero (DQ0) synchronous frame and phase lock loop methods are also covered to provide a complete guide to build the primary controllers of the VSC for microgrids applications.

2.2 Modeling of Two-Level Grid-Connected VSC with LC Filter

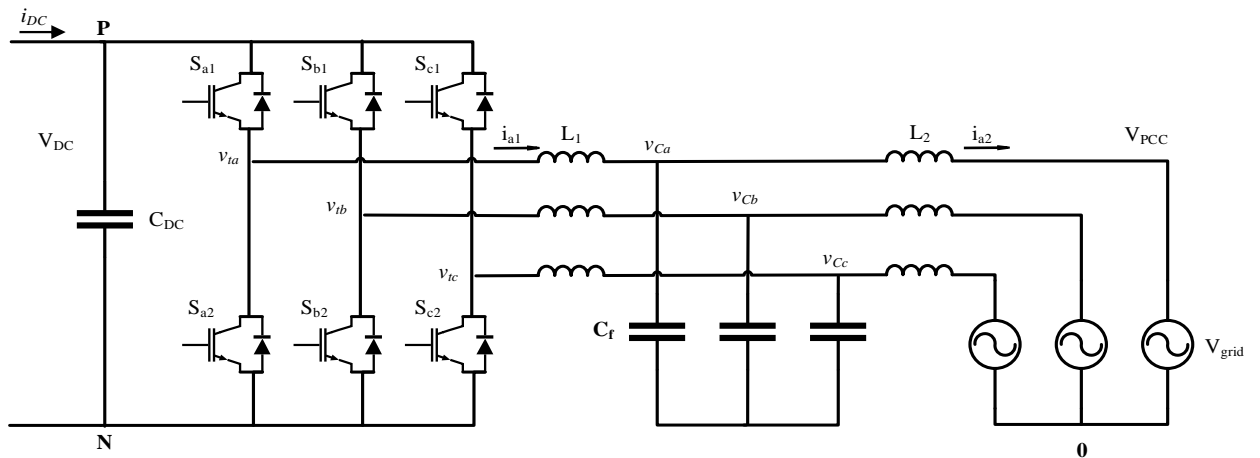


Figure 2.1: Two-level VSC with an LC filter

A basic circuit topology of a three-phase two-level VSC with an LC filter is shown in Fig. 2.1 where L_1 is the converter side filter inductance, C_f is the filter capacitor and L_2 is the grid side inductance including the grid and transformer equivalent inductance. This topology is made of six switches that are composed by sets of insulated-gate bipolar transistors (IGBTs) and anti-parallel diodes. This VSC circuit is composed of three half-bridge converters, one for each phase and the AC-side terminal of each phase (V_{tn}) can assume two voltage levels $-V_{DC}/2$ and $+V_{DC}/2$ which makes it a two-level converter.

Moreover, this VSC can provide a bidirectional power-flow path between the DC-side voltage source and the three-phase AC system. Therefore, it can operate in inverter (DC/AC) mode or rectifier (AC/DC) mode.

2.3 Space Vector Pulse Width Modulation

In order to control the output voltage of the converter, pulse width modulation is used to coordinate the switching of the transistors (S_{a1} , S_{b1} , S_{c1} , S_{a2} , S_{b2} and S_{c2}). Space Vector Pulse Width Modulation (SVPWM) has been selected because it provides 15% higher AC voltage amplitude and lower voltage and current THD than sinusoidal PWM method [1]. SVPWM refers to a special switching sequence of the three upper switches (S_{a1} , S_{b1} and S_{c1}) of the VSC shown in Fig. 2.1. These upper switches produce eight switching states, six of them are active states that produce a voltage vector of a given magnitude and two null states that produce a voltage vector of zero magnitude as shown in Table 2.1. Therefore, the main objective of this technique is to approximate the reference voltage vector V_{ref} using the eight switching patterns.

Table 2.1: Switching states and instantaneous output voltages

Voltage Vectors	Switching Vectors			Line to neutral voltage			Line to line voltage		
	a	b	c	V_{an}	V_{bn}	V_{cn}	V_{ab}	V_{bc}	V_{ca}
\vec{V}_0	0	0	0	0	0	0	0	0	0
\vec{V}_1	1	0	0	$\frac{2}{3}V_{DC}$	$-\frac{1}{3}V_{DC}$	$-\frac{1}{3}V_{DC}$	V_{DC}	0	$-V_{DC}$
\vec{V}_2	1	1	0	$\frac{1}{3}V_{DC}$	$\frac{1}{3}V_{DC}$	$-\frac{2}{3}V_{DC}$	0	V_{DC}	$-V_{DC}$
\vec{V}_3	0	1	0	$-\frac{1}{3}V_{DC}$	$\frac{2}{3}V_{DC}$	$-\frac{1}{3}V_{DC}$	$-V_{DC}$	V_{DC}	0
\vec{V}_4	0	1	1	$-\frac{2}{3}V_{DC}$	$\frac{1}{3}V_{DC}$	$\frac{1}{3}V_{dc}$	$-V_{DC}$	0	V_{DC}
\vec{V}_5	0	0	1	$-\frac{1}{3}V_{DC}$	$-\frac{1}{3}V_{DC}$	$\frac{2}{3}V_{DC}$	0	$-V_{DC}$	V_{DC}
\vec{V}_6	1	0	1	$\frac{1}{3}V_{DC}$	$-\frac{2}{3}V_{DC}$	$\frac{1}{3}V_{DC}$	V_{DC}	$-V_{DC}$	0
\vec{V}_7	1	1	1	0	0	0	0	0	0

In the SVPWM method, V_{ref} is provided by a rotating reference vector, which can be projected as a function of the voltage vectors of the respective sector in which V_{ref} falls within a particular sub cycle so that the maximum load line voltage is maximized, and the switching frequency is minimized [2]. Fig. 2.2 shows the SVPWM diagram for a two-level converter where the reference voltage vector of magnitude V_{ref} is in sector I and the dwell times (T_1 , T_2 and T_0) for which active voltage vector 1 (\vec{V}_1) active voltage vector 2 (\vec{V}_2) and the null vector (\vec{V}_0) are applied in the sub cycle T_s .

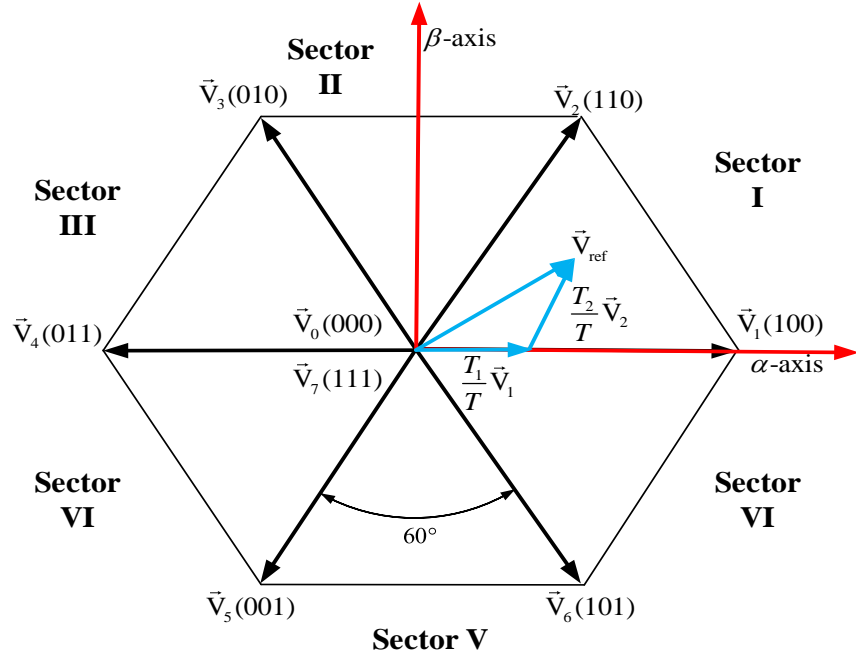


Figure 2.2: Conventional SVPWM diagram of two-level VSI

To determine the dwell time duration at sector I, let

$$T_s = T_1 + T_2 + T_0 \quad (2.1)$$

The reference voltage vector \vec{V}_{ref} as a function of the vectors at sector I is given by:

$$\vec{V}_{ref} = \frac{T_1}{T_s} \vec{V}_1 + \frac{T_2}{T_s} \vec{V}_2 \quad (2.2)$$

$$|\vec{V}_{ref}| \begin{bmatrix} \cos \alpha \\ \sin \alpha \end{bmatrix} = \frac{T_1}{T_s} |\vec{V}_1| \begin{bmatrix} \cos(0) \\ \sin(0) \end{bmatrix} + \frac{T_2}{T_s} |\vec{V}_2| \begin{bmatrix} \cos(\pi/3) \\ \sin(\pi/3) \end{bmatrix} \quad (2.3)$$

Splitting (2.3) into two equations yields:

$$T_s |\vec{V}_{ref}| \cos \alpha = T_1 |\vec{V}_1| \cos(0) + T_2 |\vec{V}_2| \cos(\pi/3) \quad (2.4)$$

$$T_s |\vec{V}_{ref}| \sin \alpha = T_1 |\vec{V}_1| \sin(0) + T_2 |\vec{V}_2| \sin(\pi/3) \quad (2.5)$$

Solving for T_2 using (2.5) and substituting the results into (2.4), the dwell time equations are determined as follows:

$$T_1 = mT_s \frac{\sin(\pi/3 - \alpha)}{\sin(\pi/3)} \quad (2.6)$$

$$T_2 = mT_s \frac{\sin(\alpha)}{\sin(\pi/3)} \quad (2.7)$$

$$T_0 = T_s - T_1 - T_2 \quad (2.8)$$

where $0 \leq \alpha \leq 60^\circ$, m : modulation index $m = \frac{V_{ref}}{V_{dc}}$ and T_s : half-carrier switching period.

Therefore, the dwell time for any sector are given by the following equations:

$$T_1 = mT_s \sin(n\pi/3 - \alpha) \quad (2.9)$$

$$T_2 = mT_s \sin(\alpha - \pi(n-1)/3) \quad (2.10)$$

$$T_0 = T_s - T_1 - T_2 \quad (2.11)$$

The ON/OFF time period for each switch in sector I is shown in Fig. 2.3.

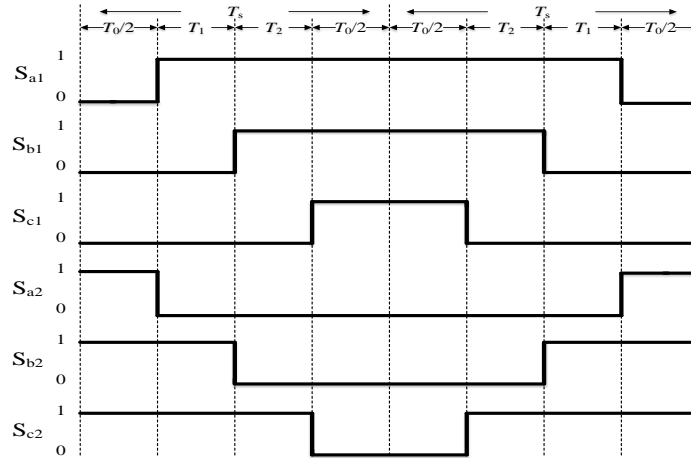


Figure 2.3: Switching patterns at Sector I

The switching patterns for all sectors using the resultant dwell times from the above equations are shown in Table 2.2 [3].

Table 2.2: Switching time calculation at each sector

Sector	Upper Switches	Lower switches
I	$S_{a1} = T_1 + T_2 + T_0/2$ $S_{b1} = T_2 + T_0/2$ $S_{c1} = T_0/2$	$S_{a2} = T_0/2$ $S_{b2} = T_1 + T_0/2$ $S_{c2} = T_1 + T_2 + T_0/2$
II	$S_{a1} = T_1 + T_0/2$ $S_{b1} = T_1 + T_2 + T_0/2$ $S_{c1} = T_0/2$	$S_{a2} = T_2 + T_0/2$ $S_{b2} = T_0/2$ $S_{c2} = T_1 + T_2 + T_0/2$
III	$S_{a1} = T_0/2$ $S_{b1} = T_1 + T_2 + T_0/2$ $S_{c1} = T_2 + T_0/2$	$S_{a2} = T_1 + T_2 + T_0/2$ $S_{b2} = T_0/2$ $S_{c2} = T_1 + T_0/2$
IV	$S_{a1} = T_0/2$ $S_{b1} = T_1 + T_0/2$ $S_{c1} = T_1 + T_2 + T_0/2$	$S_{a2} = T_1 + T_2 + T_0/2$ $S_{b2} = T_2 + T_0/2$ $S_{c2} = T_0/2$
V	$S_{a1} = T_2 + T_0/2$ $S_{b1} = T_0/2$ $S_{c1} = T_1 + T_2 + T_0/2$	$S_{a2} = T_1 + T_0/2$ $S_{b2} = T_1 + T_2 + T_0/2$ $S_{c2} = T_0/2$
VI	$S_{a1} = T_1 + T_2 + T_0/2$ $S_{b1} = T_0/2$ $S_{c1} = T_1 + T_0/2$	$S_{a2} = T_0/2$ $S_{b2} = T_1 + T_2 + T_0/2$ $S_{c2} = T_2 + T_0/2$

2.4 Direct-Quadrature-Zero Synchronous Reference Frame

Since the three-phase VSC shown in Fig. 2.1 outputs ABC reference frame signals, the number of signals must be reduced for a controller to track the reference. Therefore, the DQ-frame is selected to decrease the number of variables from three to two variables by transforming the three-half-bridge-converter system into two subsystems with ideal DC signals. As a result, a sinusoidal reference tracking task becomes an equivalent DC reference tracking task which can be performed by a proportional-integral (PI) compensator [4].

The DQ0 transformation is the product of the Park's transformation and the Clarke's transformation or the α - β -0 transformation that changes the reference axis that is used to measure the phasor values in a three-phase system into the $\alpha\beta 0$ axes [5].

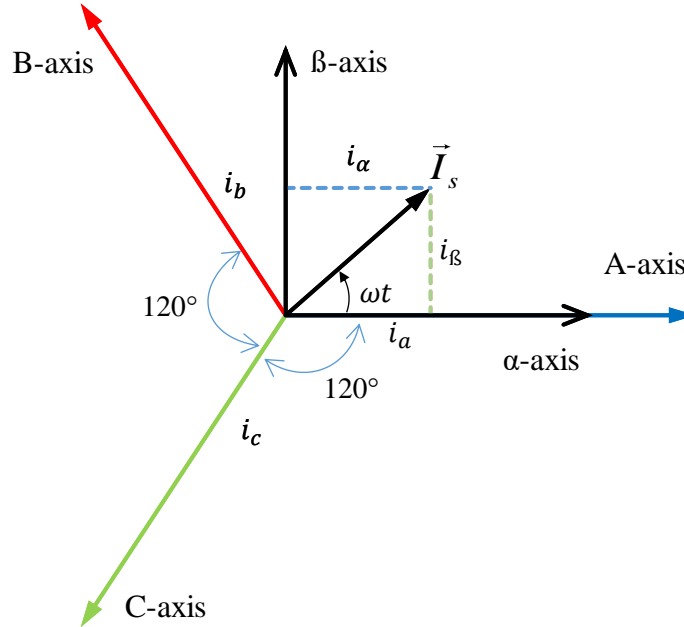


Figure 2.4: ABC and $\alpha\beta 0$ reference frames

The new values for the three phase currents (i_a , i_b , i_c) are their reflections upon the new reference axes (i_α , i_β) as shown in Fig. 2. Thus, all the phase current in a balanced three-wire three-phase system cancel out on the zero axis which is the common-mode component. Consequently, a system defined in the ABC reference frame can be fully described by the variables α and β .

Let the ABC output variables be:

$$i_a = I_M \cos(\omega t); i_b = I_M \cos\left(\omega t - \frac{2\pi}{3}\right); i_c = I_M \cos\left(\omega t + \frac{2\pi}{3}\right) \quad (2.12)$$

The $\alpha\beta 0$ transformation is given by [4] and is shown in complex (2.13) and in matrix forms (2.14) below:

$$\vec{I}_s = i_\alpha + j i_\beta = \frac{2}{3} \left(i_a + i_b e^{\frac{j2\pi}{3}} + i_c e^{\frac{-j2\pi}{3}} \right) \quad (2.13)$$

$$\begin{bmatrix} i_\alpha \\ i_\beta \\ i_0 \end{bmatrix} = \frac{2}{3} \begin{bmatrix} 1 & -1/2 & -1/2 \\ 0 & \sqrt{3}/2 & -\sqrt{3}/2 \\ 1/2 & 1/2 & 1/2 \end{bmatrix} \begin{bmatrix} i_a \\ i_b \\ i_c \end{bmatrix} \quad (2.14)$$

With the system in the $\alpha\beta 0$ reference frame, the Park transform with a -90° offset is applied to rotate the reference frame about the 0-axis at same frequency as the sinusoids that define the phasors. The α component becomes the Q component, which is at a quadrature angle (90°) to the direct component, and the $-\beta$ component becomes the D component, which is in direct alignment with the vector of rotation as shown in Fig. 2.5.

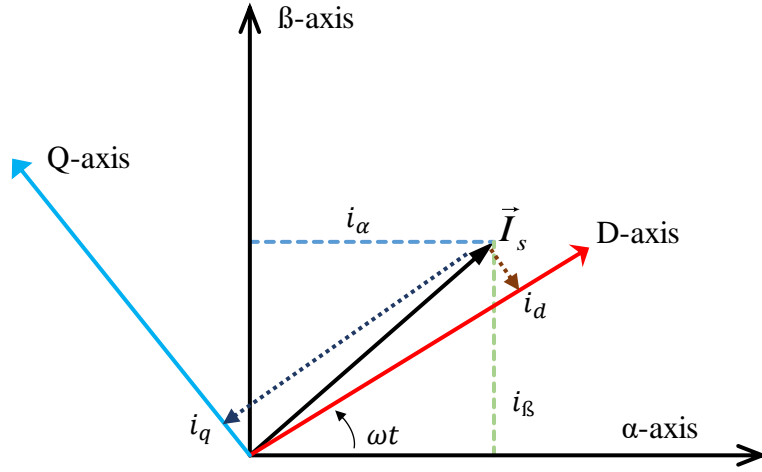


Figure 2.5: $\alpha\beta 0$ and DQ0 reference frames

$$\vec{I}_s = i_d + ji_q = (i_\alpha + ji_\beta) e^{-j(\omega t - \pi/2)} \quad (2.15)$$

$$\begin{bmatrix} i_d \\ i_q \\ i_0 \end{bmatrix} = \begin{bmatrix} \sin(\omega t) & -\cos(\omega t) & 0 \\ \cos(\omega t) & \sin(\omega t) & 0 \\ 0 & 0 & 1 \end{bmatrix} \begin{bmatrix} i_\alpha \\ i_\beta \\ i_0 \end{bmatrix} \quad (2.16)$$

The result of this rotation leads to the periodic signals becoming dc values. The rotating frame is aligned 90 degrees behind the α -axis, so that the Q-axis is aligned with the α -axis at $t = 0$. Thus, the DQ0 components are $i_d = 1$, $i_q = 0$, and $i_0 = 0$ when I_s is completely in phase with the reference angle ωt .

The full DQ0 to ABC transformation and its inverse are shown below:

$$\begin{bmatrix} i_d \\ i_q \\ i_0 \end{bmatrix} = \frac{2}{3} \begin{bmatrix} \sin(\omega t) & \sin\left(\omega t - \frac{2\pi}{3}\right) & \sin\left(\omega t + \frac{2\pi}{3}\right) \\ \cos(\omega t) & \cos\left(\omega t - \frac{2\pi}{3}\right) & \cos\left(\omega t + \frac{2\pi}{3}\right) \\ \frac{1}{2} & \frac{1}{2} & \frac{1}{2} \end{bmatrix} \begin{bmatrix} i_a \\ i_b \\ i_c \end{bmatrix} \quad (2.17)$$

$$\begin{bmatrix} i_a \\ i_b \\ i_c \end{bmatrix} = \frac{2}{3} \begin{bmatrix} \sin(\omega t) & \cos(\omega t) & 1 \\ \sin\left(\omega t - \frac{2\pi}{3}\right) & \cos\left(\omega t - \frac{2\pi}{3}\right) & 1 \\ \sin\left(\omega t + \frac{2\pi}{3}\right) & \cos\left(\omega t + \frac{2\pi}{3}\right) & 1 \end{bmatrix} \begin{bmatrix} i_d \\ i_q \\ i_0 \end{bmatrix} \quad (2.18)$$

2.5 Synchronous Frame Phase Lock Loop Design in the S-Domain

Proper synchronization with the voltage at the PCC is one of the most important tasks in the control of grid-feeding power converters to inject the desired amount of power at the desired phase angle. As a result, a Phase Lock Loop (PLL) algorithm is used to determine the instantaneous angle of one of the PCC phase voltages (usually phase A) that serves as a reference for the current control loop. A basic PLL consists of three building blocks: a phase detector, a loop filter, and a voltage-controlled oscillator. The main difference among the various PLL methods typically lies in the implementation of the phase detector block [6]. The synchronous reference frame phase-locked loop (SRF-PLL) will be presented in this section due its ease of implementation and robust performance for grid-connected applications.

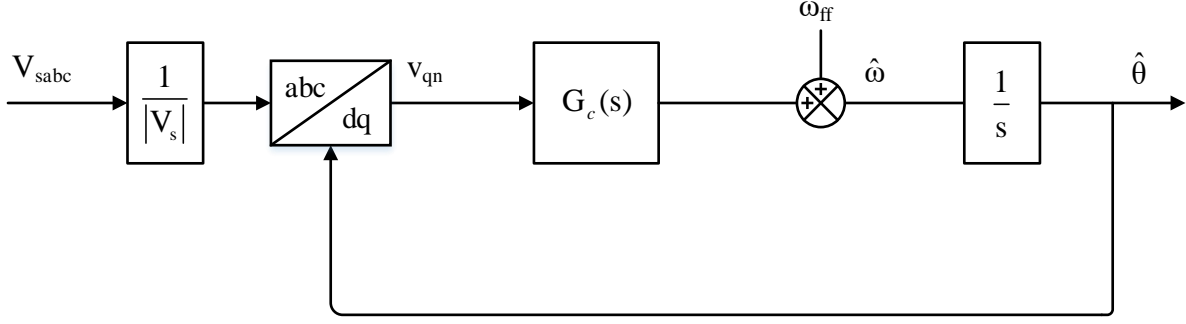


Figure 2.6: Synchronous reference frame phase-locked loop control diagram

The basic configuration of the SRF-PLL is based on a closed-loop configuration as shown in Fig. 2.6. The ABC-DQ transform is used for phase detector, a PI controller as a loop filter and an integrator as voltage-controlled oscillator. The closed-loop control is implemented with the variables in the DQ0-reference frame. The PCC quadrature voltage is used as the error between the reference and measured angle of closed-loop system. In this way, the PI controller will vary the instantaneous angle until the error $v_q = 0$ which means that for a balanced three-phase system, the measured angle is in phase with the PCC voltage phase A. The PLL is said to be locked when the q-axis component in the rotating reference frame is zero and when it is not locked the q-axis component is linearly proportional to the error [7].

Let the input sinusoidal voltages be:

$$v_{sa} = \hat{V}_s \cos(\omega t); v_{sb} = \hat{V}_s \cos\left(\omega t + \frac{2\pi}{3}\right); v_{sc} = \hat{V}_s \cos\left(\omega t - \frac{2\pi}{3}\right) \quad (2.19)$$

Let the reference voltage V_s be determined by the following equation:

$$\vec{V}_s = \hat{V}_s e^{j\theta(s)} \quad (2.20)$$

Converting (2.20) to its $\alpha\beta 0$ equivalent using (2.13) and (2.21) yields:

$$\vec{V}_s = \frac{2}{3} \left(v_{sa} + v_{sb} e^{\frac{j2\pi}{3}} + v_{sc} e^{\frac{-j2\pi}{3}} \right) = v_{s\alpha} + jv_{s\beta} = v_{s,\alpha\beta}(s) \quad (2.21)$$

Applying the dq0 transformation shown in (2.15) towards (2.21) gives:

$$v_{s,dq}(s) = v_{s,\alpha\beta}(s) e^{-j\hat{\theta}(s)} \quad (2.22)$$

Assuming the voltage instantaneous angle $\theta(s)$ is constant and the PLL angle is close to the actual angle that is $\theta(s) \approx \hat{\theta}(s)$, the q-component of (2.22) becomes:

$$v_{sq} \approx \hat{V}_s (\theta(s) - \hat{\theta}(s)) \quad (2.23)$$

Let the error between $\theta(s)$ and $\hat{\theta}(s)$ be:

$$v_{qn} = \frac{v_{sq}}{\hat{V}_s} \quad (2.24)$$

Let the estimated angle which is the output of the PLL be:

$$\hat{\theta}(s) = \frac{1}{s} \hat{\omega}(s) \quad (2.25)$$

where $\hat{\omega}(s)$ is the control action. Therefore, the control plant is:

$$G_P(s) = \frac{1}{s} \quad (2.26)$$

Let the compensator be a PI controller with gain:

$$G_C(s) = \frac{k_p s + k_i}{s} \quad (2.27)$$

The open-loop gain of the control diagram shown in Fig. 2.6 is:

$$G_{ol}(s) = G_C(s) G_P(s)$$

$$G_{ol}(s) = \frac{k_p s + k_i}{s} \cdot \frac{1}{s} = \frac{k_p s + k_i}{s^2} \quad (2.28)$$

Then, the closed-loop gain is given by:

$$G_{cl}(s) = \frac{G_{ol}(s)}{1 + G_{ol}(s)}$$

$$G_{cl}(s) = \frac{k_p s + k_i}{s^2 + k_p s + k_i} \quad (2.29)$$

A pre-filter cannot be used because the actual $\theta(s)$ would need to be filtered. As a result, the damping factor cannot be guaranteed because of the zero in the closed-loop transfer function. However, an approximate time response can be obtained by matching the denominator coefficients of the closed-loop transfer function with those of the standard second-order transfer function which is given by:

$$\frac{\omega_n^2}{s^2 + 2\zeta\omega_n s + \omega_n^2} \quad (2.30)$$

with

$$\omega_n = \frac{4.6}{\zeta t_{\text{settling}}} \quad (2.31)$$

where ω_n : natural frequency and ζ : damping factor

Matching the denominator coefficients of (2.29) with those of (2.30) and solving for the proportional and integral controller gains results in:

$$k_p = 2\zeta\omega_n \quad (2.32)$$

$$k_i = \omega_n^2 \quad (2.33)$$

2.6 Current Control Loop Design in the S-Domain

After grid synchronization has been achieved, the current control loop design can be performed. The control varies the inverter side output voltage in order to inject the desired current into the grid. The LC filter of the circuit shown in Fig. 2.1 can be approximated by an L filter for the design of the current control loop because the LC behaves as an L filter at lower frequencies which is the case for the grid-feeding mode where the capacitor acts solely to diminish high frequency components produced by the switching of the transistors [7].

The basic circuit topology of the three-phase two-level VSC with an L filter is shown in Fig. 2.7 where R_f is the resistance between the switches of the converter and the PCC, and L_f is the inductance between the switches of the converter and the PCC. Applying Kirchhoff's Voltage Law (KVL) to the circuit shown above, the simplified per-phase equivalent circuit can be derived as shown in Fig. 2.8.

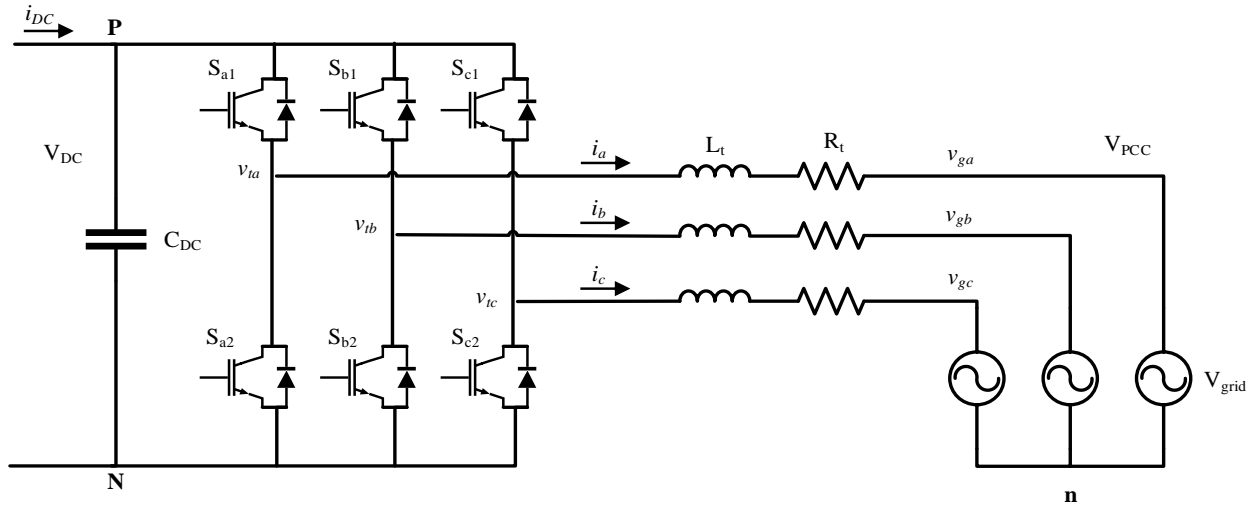


Figure 2.7: Two-level VSC with an L filter

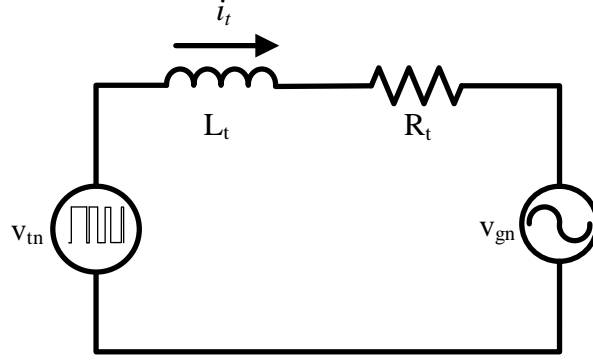


Figure 2.8: Simplified per-phase circuit of a VSC with an L filter

From Fig. 2.8, the current i_m can be controlled by adjusting the inverter output voltage v_{tn} since the grid voltage v_{gn} is a fairly constant value and can be regarded as a disturbance. Therefore, the VSC acts as a current source injecting power into the grid v_{gn} .

Applying KVL to all three per-phase circuits yields:

$$\begin{aligned} v_{tan} &= L_f \frac{di_a}{dt} + R_f i_a + v_{gan} \\ v_{tbn} &= L_f \frac{di_b}{dt} + R_f i_b + v_{gbn} \\ v_{tcn} &= L_f \frac{di_c}{dt} + R_f i_c + v_{gcn} \end{aligned} \quad (2.34)$$

Grouping all three equations of (2.34) into one equation results in:

$$v_{t,abc} = L_f \frac{di_{abc}}{dt} + R_f i_{abc} + v_{g,abc} \quad (2.35)$$

Converting ABC- $\alpha\beta$ 0 using (2.14) gives:

$$v_{t,\alpha\beta} = L_f \frac{di_{\alpha\beta}}{dt} + R_f i_{\alpha\beta} + v_{g,\alpha\beta} \quad (2.36)$$

Converting $\alpha\beta$ 0-dq0 transform using (2.15) yields:

$$v_{t,dq} = v_{t,\alpha\beta} e^{-j(\omega t - \pi/2)}$$

$$v_{t,dq} = L_f \frac{di_{dq}}{dt} + R_f i_{dq} + v_{g,dq} \quad (2.37)$$

Therefore, the ABC frame can be separated in the two subsystems d and q as explained in section 2.3:

$$L_f \frac{di_d}{dt} = v_{id} + L_f \omega i_q - R_f i_d - v_{gd} \quad (2.38)$$

$$L_f \frac{di_q}{dt} = v_{iq} - L_f \omega i_d - R_f i_q - v_{gq} \quad (2.39)$$

where, $v_{id} = \frac{V_{DC}}{\sqrt{3}} m_d$ and $v_{iq} = \frac{V_{DC}}{\sqrt{3}} m_q$; m_{dq} : modulation index ; $V_{DC}/\sqrt{3}$

: SVPWM converter gain

Due to the presence of $L_f \omega$ terms in (2.38) and (2.39), the dynamics of i_d and i_q are coupled. To decouple these dynamics and compensate for the grid disturbance inputs v_{gd} and v_{gq} , the modulation index for the d- and q-subsystem must be:

$$m_d = \frac{\sqrt{3}}{V_{DC}} (u_d - L_f \omega i_q + v_{gd}) \quad (2.40)$$

$$m_q = \frac{\sqrt{3}}{V_{DC}} (u_q + L_f \omega i_d + v_{gq}) \quad (2.41)$$

The feedforward terms are: $-L_f \omega i_q + v_{gd}$ for the d-subsystem and $L_f \omega i_d + v_{gq}$ for the q-subsystem. Substituting (2.40) into (2.38) produces:

$$L_f \frac{di_d}{dt} = u_d - R_f i_d \quad (2.42)$$

Similarly, substituting (2.41) into (2.39) yields:

$$L \frac{di_q}{dt} = u_q - R i_q \quad (2.43)$$

where u_d : output of PI compensator

As seen from (2.42) and (2.43), the control plants in the d- and q-axis current control loops are identical. As a result, the corresponding compensators can also be identical [8]. Thus, only d-axis current control compensator gains will be derived.

Applying Laplace transform to (2.42) yields:

$$L_f s I_d(s) = u_d(s) - R_f I_d(s)$$

$$I_d(s) = \frac{u_d(s)}{L_f s + R_f} \quad (2.44)$$

Therefore, the control plant becomes:

$$G_p(s) = \frac{1}{L_f s + R_f} \quad (2.45)$$

Let the compensator be a PI controller of the following form:

$$G_c(s) = \frac{k_p s + k_i}{s} \quad (2.46)$$

Next, the d-axis closed-loop transfer function will be derived with reference to Fig. 2.9:

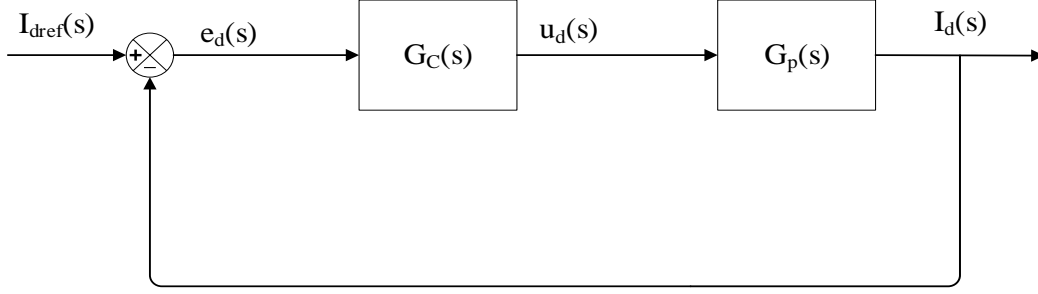


Figure 2.9: Simplified block diagram for current controlled VSC system

Then, the open-loop gain is:

$$G_{ol}(s) = G_C(s)G_p(s)$$

$$G_{ol}(s) = \frac{k_p s + k_i}{s} \cdot \frac{1}{L_f s + R_f} = \frac{k_p s + k_i}{L_f s^2 + R_f s} = \left(\frac{k_p}{L_f s} \right) \frac{s + \cancel{k_i/k_p}}{s + \cancel{R_f/L_f}} \quad (2.47)$$

Using the pole cancellation method where $\cancel{k_i/k_p} = \cancel{R_f/L_f}$, the open-loop gain (2.47)

reduces from a second-order transfer function to a first-order transfer function [8]:

$$G_{ol}(s) = \frac{k_p}{L_f s} \quad (2.48)$$

Then, the closed-loop gain of the d-axis current control is given by:

$$G_i(s) = G_{cl}(s) = \frac{G_{ol}(s)}{1 + G_{ol}(s)}$$

$$\frac{I_d(s)}{I_{dref}(s)} = G_i(s) = \frac{k_p}{k_p + L_f s} \quad (2.49)$$

If $k_p = \frac{L_f}{\tau_i}$ and $k_i = \frac{R_f}{\tau_i}$,

$$G_i(s) = \frac{1}{\tau_i s + 1} \quad (2.50)$$

where τ_i is the time constant of the resultant closed-loop system. Therefore, the settling time of this first-order closed-loop system will be:

$$t_{i,settling} = 4.6\tau_i \quad (2.51)$$

2.6 Active/Reactive Power Reference Derivations

Once the current loop has been designed, a reference generator should be derived to relate the desired active and reactive powers to be injected into the grid with the corresponding d- and q-axis reference currents. This cascading of the current control and reference generator compose the grid-feeding control mode.

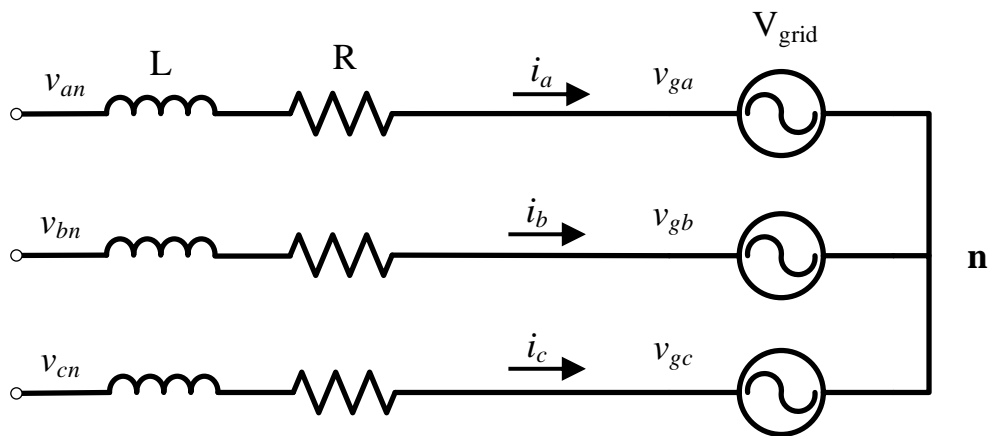


Figure 2.10: Grid power injection diagram

Considering the three-phase network of Fig. 2.10 as a balanced network where v_{an} , v_{bn} , and v_{cn} are the inverter output terminal voltages with respect to the system's neutral, v_{gan} , v_{gbn} and v_{gcn} are the grid line to neutral terminal voltages and the phase currents i_a , i_b and i_c are the current injected into the grid such that $i_a + i_b + i_c = 0$ [4]. Hence, the instantaneous total real power in the time domain is expressed as follows:

$$P_{3\phi} = v_{gan} i_a + v_{gbn} i_b + v_{gcn} i_c \quad (2.52)$$

Expressing (2.52) in space phasor notation yields:

$$P_{3\phi} = \text{Re}\left\{\vec{V}_{gn} e^{j0}\right\} \text{Re}\left\{\vec{I}_t e^{j0}\right\} + \text{Re}\left\{\vec{V}_{gn} e^{-j\frac{2\pi}{3}}\right\} \text{Re}\left\{\vec{I}_t e^{-j\frac{2\pi}{3}}\right\} + \text{Re}\left\{\vec{V}_{gn} e^{j\frac{2\pi}{3}}\right\} \text{Re}\left\{\vec{I}_t e^{j\frac{2\pi}{3}}\right\} \quad (2.53)$$

Applying the identity $\text{Re}\{x\} \text{Re}\{y\} = \frac{\text{Re}\{xy\} + \text{Re}\{xy^*\}}{2}$ to (2.53) produces:

$$P_{3\phi} = \frac{\text{Re}\left\{\vec{V}_{gn} \vec{I}_t\right\} + \text{Re}\left\{\vec{V}_{gn} \vec{I}_t^*\right\}}{2} + \frac{\text{Re}\left\{\vec{V}_{gn} \vec{I}_t e^{-j\frac{2\pi}{3}} e^{-j\frac{2\pi}{3}}\right\} + \text{Re}\left\{\vec{V}_{gn} \vec{I}_t^* e^{-j\frac{2\pi}{3}} e^{j\frac{2\pi}{3}}\right\}}{2} \\ + \frac{\text{Re}\left\{\vec{V}_{gn} \vec{I}_t e^{j\frac{2\pi}{3}} e^{j\frac{2\pi}{3}}\right\} + \text{Re}\left\{\vec{V}_{gn} \vec{I}_t^* e^{-j\frac{2\pi}{3}} e^{j\frac{2\pi}{3}}\right\}}{2} \quad (2.54)$$

Since $e^{j0} + e^{-j\frac{2\pi}{3}} + e^{j\frac{2\pi}{3}} = 0$, (2.54) becomes:

$$P_{3\phi} = \text{Re}\left\{\frac{3}{2} \vec{V}_{gn} \vec{I}_t^*\right\} \quad (2.55)$$

Since the instantaneous reactive power assumes the same expression as that for the conventional reactive power under steady-state sinusoidal balanced conditions, the complex power can be defined as follows:

$$S_{3\phi} = P_{3\phi} + jQ_{3\phi} = \frac{3}{2} \vec{V}_{gn} \vec{I}_t^* \quad (2.56)$$

Let $\vec{V}_{gn} = v_{gd} + jv_{gq}$ and $\vec{I}_t^* = i_d + j i_q$ using (2.15) and substituting into (2.56) gives:

$$S_{3\phi} = \frac{3}{2} (v_{gd} + jv_{gq}) \cdot (i_d + j i_q) \quad (2.57)$$

Applying complex multiplication yields:

$$S_{3\phi} = \frac{3}{2} \left[(v_{gd} i_d + v_{gq} i_q) + j(-v_{gd} i_q + v_{gq} i_d) \right] \quad (2.58)$$

Taking the real part of (2.58) results in:

$$P_{3\phi} = \frac{3}{2} (v_{gd} i_d + v_{gq} i_q) \quad (2.59)$$

Taking the imaginary part of (2.58) gives:

$$Q_{3\phi} = \frac{3}{2} (-v_{gd} i_q + v_{gq} i_d) \quad (2.60)$$

Using (2.59) and (2.60) to solve for i_d and i_q produces:

$$i_d = \frac{2}{3} \left(\frac{P_{3\phi} v_{gd} + Q_{3\phi} v_{gq}}{v_{gd}^2 + v_{gq}^2} \right) \quad (2.61)$$

$$i_q = \frac{2}{3} \left(\frac{P_{3\phi} v_{gq} - Q_{3\phi} v_{gd}}{v_{gd}^2 + v_{gq}^2} \right) \quad (2.62)$$

The resultant (2.61) and (2.62) can be simplified if the PLL is locked in the steady state resulting in $v_{gq} = 0$. Moreover, these equations can be used to provide the current loop with references to inject the desired active and reactive powers to the grid; that is:

$$i_{dref} = i_d = \frac{2}{3} \frac{P_{ref}}{v_{gd}} \quad (2.63)$$

$$i_{qref} = i_q = -\frac{2}{3} \frac{Q_{ref}}{v_{gd}} \quad (2.64)$$

2.8 DC Bus Voltage Control Loop Design in the S-Domain

DC bus voltage control will need to be implemented for the VSC to act in the rectifier mode converting AC to DC power and controlling the voltage of the DC link capacitor so that an output load can be supplied by this converter. Moreover, this control structure can be used to vary the current reference of the current control loop in order to control the DC power input from an intermittent DC power source such as a photovoltaic array. The control of the DC-link voltage is a crucial part of static compensators, back-to-back converters, and variable-speed wind-power-units [9].

The circuit topology of Fig. 2.7 has been modified with the addition of a bleeding resistor R_B and more feedback signals (i_{DC} , i_L) to facilitate the modeling of a DC-control plant as shown in Fig. 2.11, where R_f is the resistance between the output of the inverter and the PCC, and L_f is the inductance between the output of the inverter and the PCC.

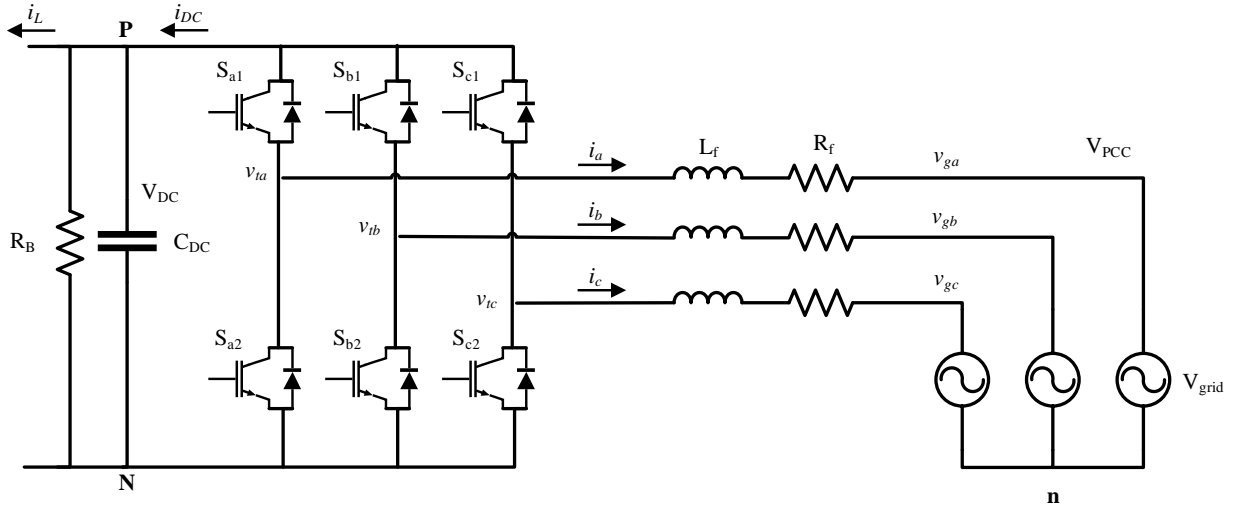


Figure 2.11: Two-level VSC with an L filter and DC-link bleeding resistor

Modeling the circuit in Fig. 2.11 into the DQ synchronous reference frame representation only considers the d-axis component because the DC-link capacitor can only be charged or discharged when there is active power transfer. Therefore, no instantaneous reactive current is involved in the process and the q-axis component is not needed in this task as shown in Fig. 2.12.

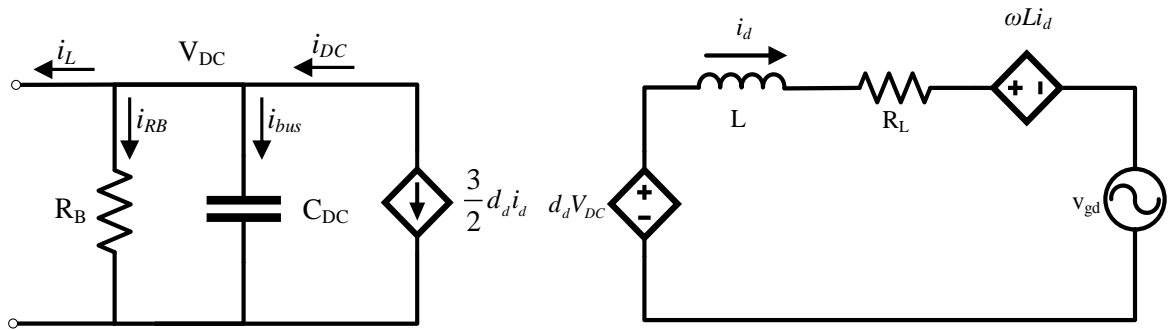


Figure 2.12: D-axis component representation of the VSC with an L filter and a bleeding resistor

The dynamic equation of the DC-link capacitor voltage is presented as follows:

$$\begin{aligned}
 i_{DC} &= i_{bus} + i_{RB} + i_L \\
 i_{bus} &= i_{DC} - i_{RB} - i_L \\
 C_{DC} \frac{dv_{DC}}{dt} &= i_{DC} - \frac{v_{DC}}{R_B} - i_L
 \end{aligned} \tag{2.65}$$

Applying the Laplace transform to (2.65) yields:

$$\begin{aligned}
 \left[sC_{DC} + \frac{1}{R_B} \right] V_{DC}(s) &= I_{DC}(s) - I_L(s) \\
 V_{DC}(s) &= \frac{1}{\left[sC_{DC} + \frac{1}{R_B} \right]} u_d(s) = \frac{R_B}{sC_{DC}R_B + 1} u_d(s)
 \end{aligned} \tag{2.66}$$

Let $u_d(s) = I_{DC}(s) - I_L(s)$: output of PI compensator. The feedforward term is: $I_{Ld}(s)$ so that the controller does not have to compensate for a measured value.

Therefore, the control plant becomes:

$$G_P(s) = \frac{R_B}{sC_{DC}R_B + 1} \tag{2.67}$$

Since i_{DC} cannot be controlled directly but through the current drawn from the grid and assuming a lossless converter, the relationship between these currents is [10]:

$$P_{3\phi} = P_{DC} \tag{2.68}$$

Substituting (2.59) into (2.68) and substituting for the DC-bus power yields:

$$\frac{3}{2} v_{gd} i_d = -i_{DC} V_{DC} \quad (2.69)$$

Let the time constant of the current control loop τ_i and the time constant of the DC bus voltage control loop τ_{DC} have the following relationship,

$$\tau_i \ll \tau_{DC} \quad (2.70)$$

If the condition in (2.70) is fulfilled, $\dot{i}_d = I_{dref}$ and both control loops are decoupled, the relationship between these control loops can be derived as follows:

$$\begin{aligned} I_{dref} &= -\frac{2}{3} \frac{V_{DC}}{v_{gd}} I_{DC} \\ K_{inner} &= \frac{I_{DC}}{I_{dref}} = -\frac{3}{2} \frac{v_{gd}}{V_{DC}} \end{aligned} \quad (2.71)$$

Let the compensator be a PI controller of the following form:

$$G_C(s) = \frac{k_p s + k_i}{s} \quad (2.72)$$

The selected approach to control the DC voltage will be a cascade implementation of an outer loop for the DC bus voltage control and an inner loop for the current control as derived in section 2.5 in such a way that the DC voltage controller time response is much slower than that of the current controller in order to fulfilled (2.70). In other words, the current loop is seen as a constant gain by the DC-voltage loop, and the current reference will change slowly enough for the current controller to respond without error. A typical separation factor between the current loop and the DC-bus control loop is around 10 times as implemented in [11]. Therefore, the dynamics of both circuits shown in Fig. 2.12 are clearly decoupled.

Next, the d-axis DC-bus voltage control compensators gains will be derived with reference to Fig. 2.13:

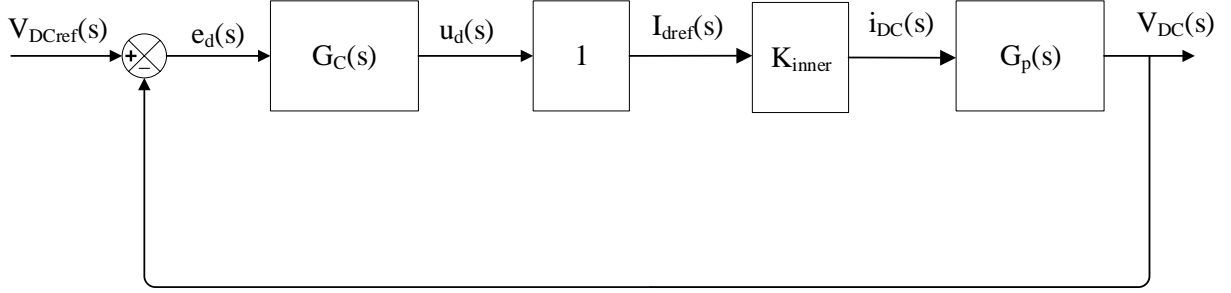


Figure 2.13: Simplified block diagram for the DC-Link Voltage loop of the VSC System

Then, the open-loop gain is:

$$G_{ol}(s) = G_C(s) G_P(s) K_{inner}$$

$$G_{ol}(s) = \frac{k_p s + k_i}{s} \cdot \frac{R_B}{s C_{DC} R_B + 1} \cdot K_{inner} = \frac{K_{inner} R_B (k_p s + k_i)}{s^2 C_{DC} R_B + s} \quad (2.73)$$

Then, the closed-loop gain of the d-axis current control is:

$$G_{DC}(s) = G_{cl}(s) = \frac{G_{ol}(s)}{1 + G_{ol}(s)}$$

$$G_{DC}(s) = \frac{K_{inner} (k_p s + k_i) / C_{DC}}{s^2 + \left(\frac{K_{inner} R_B k_p + 1}{C_{DC} R_B} \right) s + \frac{K_{inner} k_i}{C_{DC}}} \quad (2.74)$$

Since (2.74) has a numerator of first order, a pre-filter will be implemented to cancel this term and be able to match (2.74) with the standard second-order transfer function which was given by (2.30); that is:

$$G_{PF}(s) = \frac{G_{DC,desired}(s)}{G_{DC,old}(s)} = \frac{k_i}{(k_p s + k_i)} \quad (2.75)$$

Consequently multiplying (2.74) and (2.75) yields:

$$G_{DC}(s) = \frac{\frac{K_{inner} k_i}{C_{DC}}}{s^2 + \left(\frac{K_{inner} R_B k_p + 1}{C_{DC} R_B} \right) s + \frac{K_{inner} k_i}{C_{DC}}} \quad (2.76)$$

Matching the denominator coefficients of (2.76) with those of (2.30) and solving for the proportional and integral controller gains results in:

$$k_p = \frac{2\zeta\omega_n C_{DC} R_B - 1}{K_{inner} R_B} \quad (2.77)$$

$$k_i = \frac{\omega_n^2 C_{DC}}{K_{inner}} \quad (2.78)$$

Therefore, the settling time of this second closed-loop system is:

$$\tau_{DC} = \frac{1}{\zeta\omega_n}$$

$$t_{DC,settling} = 4.6 \cdot \tau_{DC} \quad (2.79)$$

2.9 AC Voltage Control Loop Design in the S-Domain

In islanded mode, a VSC can be operated in grid-forming mode to create a grid reference for the islanded microgrid and transfer active or reactive powers so that the microgrid can continue to function when the main grid is not available due to a power outage or a fault. The grid-forming mode is achieved by cascading the AC voltage control loop and the current control

loop in order to vary the inverter side output voltage with the intention of regulating the frequency and amplitude of the filter capacitor voltage which is connected to the PCC as shown in the figure below.

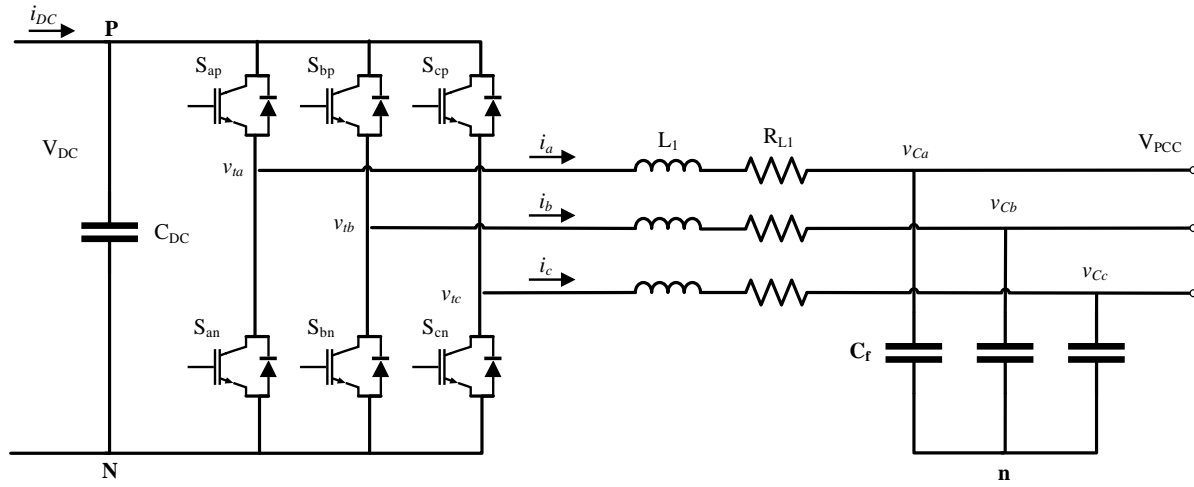


Figure 2.14: Two-level VSC with an LC filter

The circuit topology of the three-phase two-level VSC with an LC filter to be derived for the grid-forming mode is shown in Fig. 2.14 where R_{L1} and L_1 are the resistance between the converter and the filter capacitor, respectively. Applying KVL, the simplified per-phase equivalent circuit can be derived as shown in Fig. 2.15.

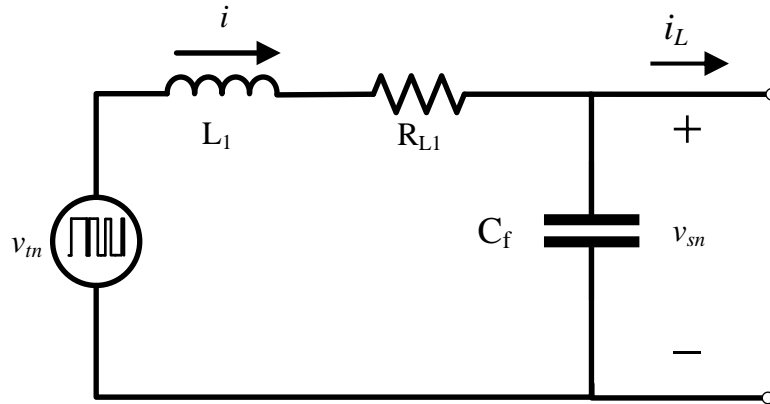


Figure 2.15: Simplified per-phase circuit of a VSC with an LC filter

Applying Kirchhoff's current law (KCL) to all three per-phase circuits yields:

$$\begin{aligned} i_a &= i_{Cfa} + i_{La} \\ i_b &= i_{Cfb} + i_{Lb} \\ i_c &= i_{Cfc} + i_{Lc} \end{aligned} \quad (2.80)$$

Grouping all three equations of (2.80) into one equation gives:

$$\begin{aligned} i_{abc} &= i_{Cf,abc} + i_{L,abc} \\ i_{abc} &= i_{Cf,abc} + i_{L,abc} \end{aligned} \quad (2.81)$$

Converting ABC- $\alpha\beta$ using (2.14) results in:

$$i_{Cf,\alpha\beta} = i_{\alpha\beta} - i_{L,\alpha\beta} \quad (2.82)$$

Converting $\alpha\beta$ -dq0 transform using (2.15) yields:

$$\begin{aligned} i_{Cf,dq} &= i_{Cf,\alpha\beta} e^{-j(\omega t - \pi/2)} \\ i_{C,dq} &= i_{dq} - i_{L,dq} \end{aligned} \quad (2.83)$$

Therefore, the ABC frame can be separated in the two subsystems d and q as explained in section 2.3 and be cascaded to the d- and q-axis current control loops producing the following:

$$C_f \frac{dv_{sd}}{dt} = C_f \omega v_{sq} + i_d - i_{Ld} \quad (2.84)$$

$$C_f \frac{dv_{sq}}{dt} = -C_f \omega v_{sd} + i_q - i_{Lq} \quad (2.85)$$

The dynamics of V_{sd} and V_{sq} are coupled due to the presence of $C_f \omega$ terms in (2.84) and (2.85). To decouple these dynamics and compensate for the load disturbance inputs i_{Ld} and i_{Lq} , the feedforward terms $(-C_f \omega V_{sq} + i_{Ld})$ for the d-axis subsystem and $(C_f \omega V_{sd} + i_{Lq})$ for the q-axis subsystem are added. Moreover, it can be seen from (2.84) and (2.85) that the control plants of both d- and q-axis subsystems are identical; thus:

$$\frac{dV_{sd}}{dt} = \frac{1}{C_f} [u_d] \quad (2.86)$$

where u_d : output of PI compensator. Applying the Laplace transform to (2.86) yields,

$$V_{sd}(s) = \frac{u_d(s)}{sC_f} \quad (2.87)$$

Therefore, the control plant is given by:

$$G_p(s) = \frac{1}{sC_f} \quad (2.88)$$

Additionally, the time constant of the AC voltage control loop τ_v is chosen to be 5 times larger than the time constant of the current control loop τ_i so by fulfilling the following both control loops are decoupled,

$$\tau_i \ll \tau_v \quad (2.89)$$

Consequently $I_{dq}(s) = I_{dqref}(s)$ for the AC voltage control loop and the inputs to the current control loops are:

$$I_{dref}(s) = u_d(s) - C_f \omega V_{sq}(s) + I_{Ld}(s) \quad (2.90)$$

$$I_{qref}(s) = u_q(s) + C_f \omega V_{sd}(s) + I_{Lq}(s) \quad (2.91)$$

Let the compensator be a PI controller gain of the following form:

$$G_C(s) = \frac{k_p s + k_i}{s} \quad (2.92)$$

Since the control plant of (2.88) is identical for both subsystems, the corresponding compensators can also be identical and only the d-axis voltage control compensators gains will be derived next with reference to Fig. 2.16:

Then, the open-loop gain is:

$$G_{ol}(s) = G_C(s) G_P(s) \quad (2.93)$$

$$G_{ol}(s) = \frac{k_p s + k_i}{s} \cdot \frac{1}{s C_f} = \frac{k_p s + k_i}{s^2 C_f}$$

Then, the closed-loop gain of the d-axis current control is:

$$G_v(s) = G_{cl}(s) = \frac{G_{ol}(s)}{1 + G_{ol}(s)}$$

$$G_v(s) = \frac{\frac{(k_p s + k_i)}{C_f}}{s^2 + (\frac{k_p}{C_f})s + \frac{k_i}{C_f}} \quad (2.94)$$

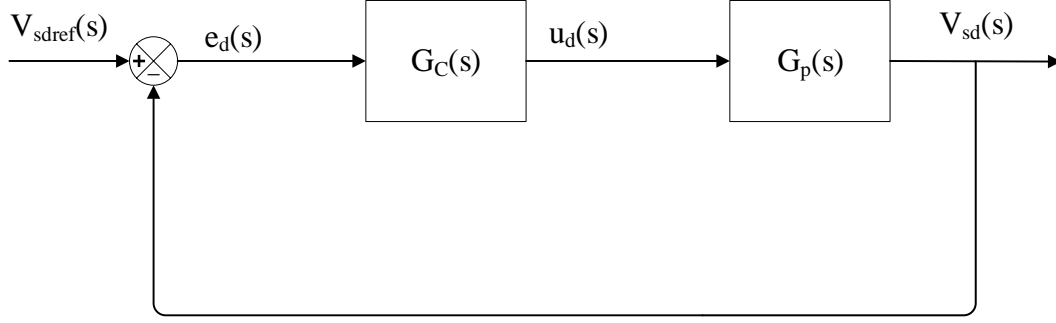


Figure 2.16: Simplified block diagram for AC voltage loop of the VSC system

Since (2.94) has a numerator of first order, a pre-filter will be implemented to cancel this term and be able to match (2.94) with the standard second-order transfer function which was given in (2.30). A pre-filter is required as follows:

$$G_{PF}(s) = \frac{G_{DC,desired}(s)}{G_{DC,old}(s)} = \frac{k_i}{k_p s + k_i} \quad (2.95)$$

Consequently, multiplying (2.94) and (2.95) yields:

$$G_v(s) = \frac{k_i}{s^2 C_f + k_p s + k_i} \quad (2.96)$$

Matching the denominator coefficients of (2.96) with those of (2.30) and solving for the proportional and integral controller gains results in:

$$k_p = 2\zeta\omega_n C_f \quad (2.97)$$

$$k_i = \omega_n^2 C_f \quad (2.98)$$

Therefore,

$$\tau_v = \frac{1}{\zeta\omega_n} \quad (2.99)$$

The settling time of this second-order closed-loop system will be 5 times larger than the settling time of the current control loop of section 2.5 in order to decouple both control loops as explained previously. That is:

$$t_{v,settling} = \frac{4.6}{\zeta\omega_n} = 4.6 \cdot \tau_v = 4.6 \cdot 5 \cdot \tau_i = 5 \cdot t_{i,settling} \quad (2.100)$$

2.10 Concluding Remarks

This chapter has reviewed the fundamental circuit model of the VSC with an output LC filter. The underlying theory and design behind the operation of the VSC as an active rectifier with DC bus control and as an inverter in grid-feeding and grid-forming modes combining the derived control loops has been also presented. This included the reference frames, space vector modulation and phase lock loop that the controller relies upon. The next chapter will focus on converting the s-domain control loops derived in this chapter into the z-domain.

2.11 References

- [1] A. Kumar and D. Chatterjee, "A survey on space vector pulse width modulation technique for a two-level inverter," *2017 National Power Electronics Conference (NPEC)*, Pune, 2017, pp. 78-83.
- [2] M. Rashid, *Power Electronics Handbook*. S.I.: Butterworth-Heinemann Ltd, 2017.
- [3] Kubeitari, M., Alhusayn, A., Alnahr, M. (2012). 'Space Vector PWM Simulation for Three Phase DC/AC Inverter'. World Academy of Science, Engineering and Technology, International Science Index 72, *International Journal of Electrical, Computer, Energetic, Electronic and Communication Engineering*, 6(12), 1402 - 1407.
- [4] Amirnaser Yazdani; Reza Iravani, "Space Phasors and Two-Dimensional Frames," in *Voltage-Sourced Converters in Power Systems: Modeling, Control, and Applications*, , IEEE, 2010.

- [5] Paul Krause; Oleg Wasynczuk; Scott D. Sudhoff; Steven Pekarek, "Reference-Frame Theory," in *Analysis of Electric Machinery and Drive Systems*, , IEEE, 2013.
- [6] S. Golestan, M. Monfared and F. D. Freijedo, "Design-Oriented Study of Advanced Synchronous Reference Frame Phase-Locked Loops," in *IEEE Transactions on Power Electronics*, vol. 28, no. 2, pp. 765-778, Feb. 2013.
- [7] M. Bhardwaj, (2013). *Software Phase Locked Loop Design Using C2000™ Microcontrollers for Three Phase Grid Connected Applications* (Application Report No. SPRABT4A). Retrieved from Texas Instruments website: <http://www.ti.com/lit/an/sprabt4a/sprabt4a.pdf>
- [8] M. Liserre, F. Blaabjerg and S. Hansen, "Design and control of an LCL-filter-based three-phase active rectifier," in *IEEE Transactions on Industry Applications*, vol. 41, no. 5, pp. 1281-1291, Sept.-Oct. 2005.
- [9] Amirnaser Yazdani; Reza Iravani, " Grid-Imposed Frequency VSC System Control in dq-Frame," in *Voltage-Sourced Converters in Power Systems: Modeling, Control, and Applications*, , IEEE, 2010.
- [10] Remus Teodorescu; Marco Liserre; Pedro Rodriguez, "Grid Converter Control for WTS," in *Grid Converters for Photovoltaic and Wind Power Systems*
- [11] H. M. A. Antunes, S. M. Silva, D. I. Brandao, R. V. Ferreira and B. d. J. C. Filho, "Analysis of a grid-forming converter based on repetitive control in centralized AC microgrid," *2017 IEEE 8th International Symposium on Power Electronics for Distributed Generation Systems (PEDG)*, Florianopolis, 2017, pp. 1-8.

CHAPTER 3

CONTROL DESIGN IN THE Z-DOMAIN

3.1 Introduction

Generally, the control implementation of the VSC is performed by digital signal processors (DSPs), FPGA or some kind of digital microprocessor. Therefore, the design of control loops that are used to drive the VSC into the different operation modes need to be implemented in the discrete-time domain. The control design in the z-domain and conversion from the s-domain to the z-domain will be covered in this chapter. This includes the phase lock loop, current control loop, DC-bus control loop and AC voltage control loop designs. Moreover, the step response comparison between the continuous- and discrete-time domain implementations of the control loops will be carried out.

3.2 Synchronous Frame Phase Lock Loop in the Z-Domain

As stated in Chapter 2, proper synchronization with the voltage at the point of common coupling (PCC) is one of the most crucial tasks in the control of voltage source converters (VSC) due to the need of the reference angle to calculate correct values with respect to the PCC. As a result, the synchronous reference frame phase-locked loop (SRF-PLL) algorithm derived in Chapter 2 will be converted to the z-domain for determining accurate digital representations of the continuous values in the necessary reference frame at a particular sampling instant.

Let the reference voltage V_s be determined by the following equation:

$$\vec{V}_s(t) = \hat{V}_s e^{j\theta(t)} \quad (3.1)$$

Converting (3.1) to its $\alpha\beta 0$ equivalent using (2.21) yields:

$$\vec{V}_s[k] = v_{s,\alpha\beta}[k] \quad (3.2)$$

Applying the dq0 transformation shown in (2.15) to (3.2) gives:

$$v_{s,dq}[k] = v_{s,\alpha\beta}[k] e^{-j\hat{\theta}(k)} \quad (3.3)$$

Assuming the voltage instantaneous angle $\theta[k]$ is constant and the PLL angle is close to the actual angle that is $\theta[k] \approx \hat{\theta}[k]$, the q-component of (3.3) becomes:

$$v_{sq}[k] \approx \hat{V}_s (\theta[k] - \hat{\theta}[k]) \quad (3.4)$$

Let the error between $\theta[k]$ and $\hat{\theta}[k]$ be:

$$v_{qn}[k] = \frac{v_{sq}[k]}{\hat{V}_s} \quad (3.5)$$

Applying the z-transformation to (3.5) yields:

$$v_{qn}(z) = \frac{v_{sq}(z)}{\hat{V}_s} \quad (3.6)$$

The forward Euler discretization method to transform from the s-domain to the z-domain is given by [1]:

$$s \rightarrow \frac{z-1}{T_s} \quad (3.7)$$

Let the estimated angle of (2.25) be converted to the discrete z-domain by applying (3.7):

$$\hat{\theta}(s) = \frac{T_s}{z-1} \hat{\omega}(z) \quad (3.8)$$

where $\hat{\omega}(s)$ is the control action and T_s is the sampling period. Therefore, the control plant is:

$$G_p(z) = \frac{T_s}{z-1} \quad (3.9)$$

Let the compensator be a PI controller with gain:

$$G_{Cd}(z) = k_{pd} + \frac{k_{id}}{T_s / (z-1)} = \frac{k_{pd}(z-1) + k_{id}T_s}{z-1} \quad (3.10)$$

Next, the PLL closed-loop transfer function will be derived with reference to Fig. 3.1. Thus, the open-loop is determined by:

$$G_{ol}(z) = G_{Cd}(z)G_{Pd}(z)$$

$$G_{ol}(z) = \frac{k_{pd}(z-1) + k_{id}T_s}{z-1} \cdot \frac{T_s}{z-1} = \frac{(k_{pd}T_s)z + (k_{id}T_s^2 - k_{pd}T_s)}{z^2 - 2z + 1} \quad (3.11)$$

Then, the closed-loop gain is given by:

$$G_{cl}(z) = \frac{G_{ol}(z)}{1 + G_{ol}(z)}$$

$$G_{cl}(s) = \frac{(k_{pd}T_s)z + (k_{id}T_s^2 - k_{pd}T_s)}{z^2 + (k_{pd}T_s - 2)z + (k_{id}T_s^2 - k_{pd}T_s + 1)} \quad (3.12)$$

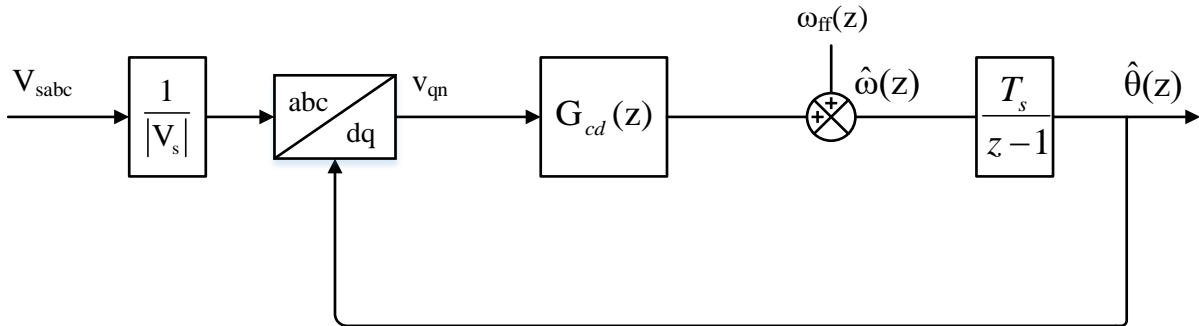


Figure 3.1: SRF-PLL block diagram in the z-domain

A pre-filter cannot be used because the actual $\theta[k]$ would need to be filtered. As a result, the damping factor cannot be guaranteed because of the zero in the closed-loop transfer function as stated in Chapter 2. However, an approximate time response can be obtained by matching the denominator coefficients of (3.11) with those of (2.30) converted to the z-domain. Hence, the poles of (2.30) are given by:

$$\begin{aligned} p_1(s) &= \omega_n \left(\zeta + j\sqrt{1-\zeta^2} \right) \\ p_2(s) &= \omega_n \left(\zeta - j\sqrt{1-\zeta^2} \right) \end{aligned} \quad (3.13)$$

Applying the matched z-transform method $z \rightarrow e^{sT_s}$ to (3.13) results in:

$$\begin{aligned} p_1(z) &= e^{\omega_n \left(\zeta + j\sqrt{1-\zeta^2} \right) T_s} \\ p_2(z) &= e^{\omega_n \left(\zeta - j\sqrt{1-\zeta^2} \right) T_s} \end{aligned} \quad (3.14)$$

Determining the denominator coefficients by multiplying the denominator factors results in:

$$\begin{aligned} [z - p_1(z)][z - p_2(z)] &= [z - p_1(z)][z - p_2(z)^*] \\ z^2 - 2 \operatorname{Re}\{p_1(z)\}z - |p_1(z)|^2 &= z^2 - 2e^{-\zeta\omega_n T_s} \cos\left(\omega_n T_s \sqrt{1-\zeta^2}\right)z + e^{-2\zeta\omega_n T_s} \end{aligned} \quad (3.15)$$

Matching the denominator coefficients of (3.12) with the coefficients of (3.15) and solving for the proportional and integral controller gains yields:

$$k_{pd} = \frac{-2e^{-\zeta\omega_n T_s} \cos\left(\omega_n T_s \sqrt{1-\zeta^2}\right) + 2}{T_s} \quad (3.16)$$

$$k_{id} = \frac{e^{-2\zeta\omega_n T_s} + k_{pd} T_s - 1}{T_s^2} \quad (3.17)$$

Now that the controller gains have been derived in the discrete-time domain, a simulation to compare the response of the continuous PLL designed in Chapter 2 and its discrete counterpart will be performed using MATLAB/SimulinkTM. The step response test consists on having both PLL controller designs measure the voltage of a three-phase balanced source supplying power to a balanced resistive load, then the frequency of the source performs a step change at a specified time. For a second-order continuous systems, the resultant value at the settling time should be within 2% of the final value [2]. Since the angle $\theta(t)$ is changing continuously, a measurement of the frequency is performed in order to better demonstrate the controller response with a constant value.

Figs. 3.2 and 3.3 shows the Simulink model of the continuous and discrete controllers, respectively. The test parameters are presented in Table 3.1 where it can be highlighted the base frequency, settling time, step change time, step magnitude and controllers' gains. The controller's gains are very close in both designs due to the high sampling frequency. The initial frequency is 60 Hz at $t = 0$ s and steps 20% to 72 Hz at $t = 0.2$ s.

Table 3.1 PLL step response test parameters

Parameter	Symbol	Value
Base Voltage	V_B	480 V
Base Frequency	f_B	60 Hz
Sampling Frequency	T_s	8 kHz
Settling Time	$T_{PLL,settling}$	100 μ s
Percentage Overshoot	PO	5%
Natural Frequency	ω_n	65.06 rad/s
Damping Factor	ζ	0.707
Proportional Gain – Continuous Controller	K_p	92
Integral Gain – Continuous Controller	K_i	4233
Proportional Gain – Discrete Controller	K_{pd}	91.99
Integral Gain – Discrete Controller	K_{id}	4209
Step Change Time	T_{step}	0.2 s
Step Magnitude	M_{step}	12 Hz

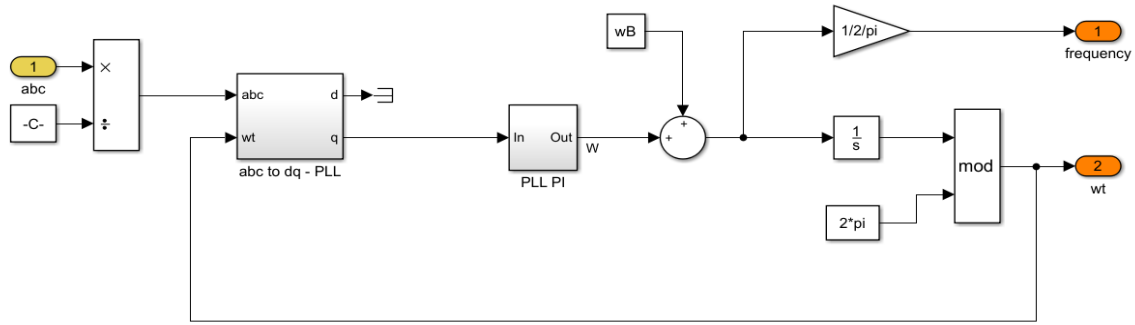


Figure 3.2: SRF-PLL control diagram in the s-domain

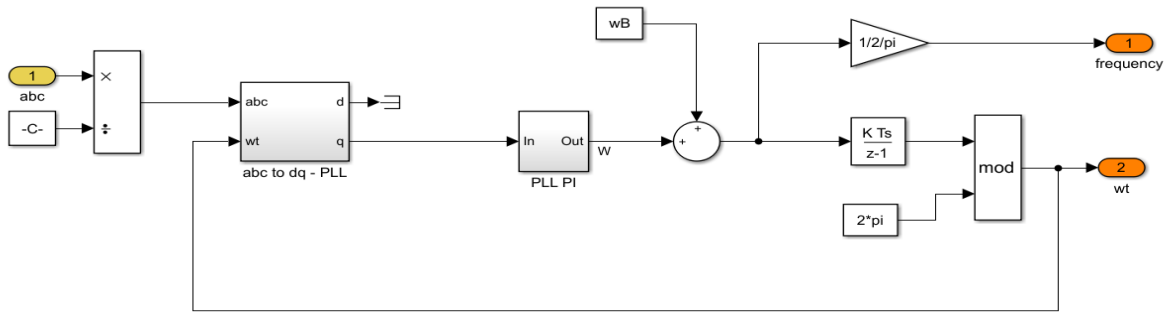


Figure 3.3: SRF-PLL control diagram in the z-domain

Fig. 3.4 shows that the maximum value achieved in the step response is 74.62 Hz which corresponds to a 3.63% percent overshoot, which is lower than the desired 5%. The desired 5% overshoot was not be achieved because a prefilter could not be used which resulted in a closed-loop transfer function with first order numerator instead of a zero-order. On the contrary, both controllers have very similar time responses to the step change and are able to settle to over 98% of the final value at $t = 0.3$ s in the desired $100 \mu\text{s}$ settling time after the step change. Hence, it can be concluded that the discrete controller design is a good approximation of the continuous controller design that can be implemented in a digital controller.

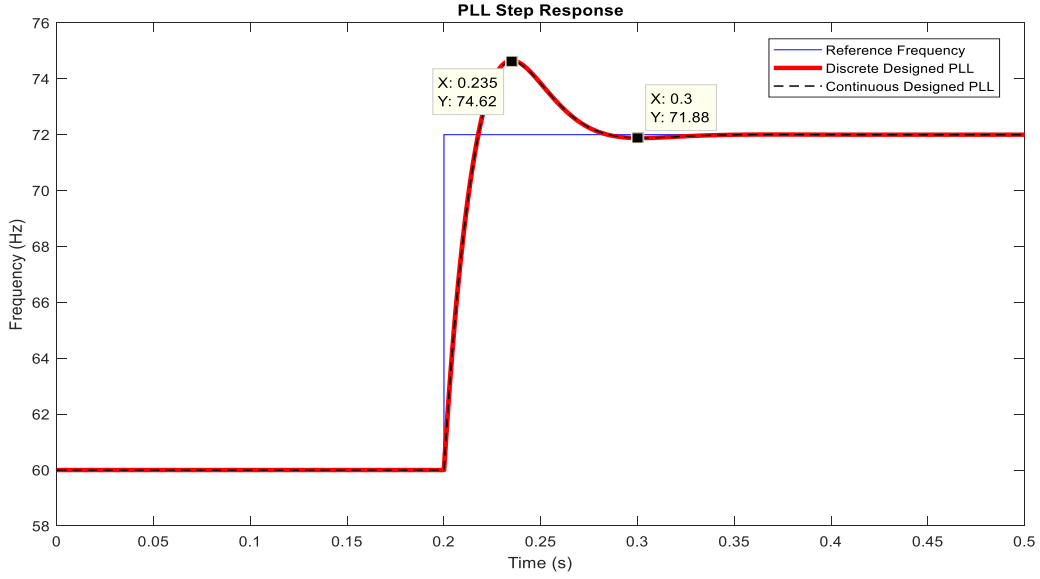


Figure 3.4: SRF-PLL controllers' step response test

3.3 Current Control Loop Design in the Z-Domain

Since the current control loop acts as the inner loop for the several VSC operating modes, it is imperative that the current control design be implemented in the z-domain, so it can be used by digital controllers. The derivation of the current control loop in the z-domain is more complicated than the PLL derived in the previous section due to the plant not being a simple discrete integrator and the existence of coupling between the d- and q-axis components.

The first step to discretize the continuous control plant is to derive the plant state-space equation in the $\alpha\beta$ frame in the continuous-time domain from (2.36) so it can be converted to the DQ frame in the discrete time domain. That is,

$$\begin{aligned}
 v_{t,\alpha\beta} &= L_f \frac{di_{\alpha\beta}}{dt} + R_f i_{\alpha\beta} + v_{g,\alpha\beta} \\
 \frac{di_{\alpha\beta}}{dt} &= \frac{1}{L_f} (-R_f i_{\alpha\beta} + v_{t,\alpha\beta} - v_{g,\alpha\beta})
 \end{aligned} \tag{3.18}$$

Let the standard-state space equation be:

$$\dot{x}(t) = Ax(t) + Bu(t) \quad (3.19)$$

Comparing (3.18) to (3.19) yields:

$$A = \begin{bmatrix} -\frac{R_f}{L_f} \end{bmatrix} \quad B = \begin{bmatrix} \frac{1}{L_f} \end{bmatrix} \quad (3.20)$$

Applying the zero-order-hold discretization method to (3.20) by using the following property [3] gives:

$$e^{\begin{bmatrix} A & B \\ 0 & 0 \end{bmatrix} T_s} = \begin{bmatrix} Ad & Bd \\ 0 & I \end{bmatrix} \quad (3.21)$$

$$A_d = \begin{bmatrix} e^{-\frac{R_f T_s}{L_f}} \end{bmatrix} \quad B_d = \begin{bmatrix} \frac{1 - e^{-\frac{R_f T_s}{L_f}}}{R_f} \end{bmatrix}$$

Therefore, applying (3.21) to (3.19) results in:

$$x[k+1] = A_d x[k] + B_d u[k] \quad (3.22)$$

and discretizing (3.18) yields:

$$i_{\alpha\beta}[k+1] = A_d i_{\alpha\beta}[k] + B_d (v_{t,\alpha\beta}[k] - v_{g,\alpha\beta}[k]) \quad (3.23)$$

Let the following equation be the DQ to $\alpha\beta$ transform in the discrete-domain:

$$i_{dq}[k] = e^{-j\left(\omega k T_s - \frac{\pi}{2}\right)} \cdot i_{\alpha\beta}[k] = j e^{-j\omega k T_s} \cdot i_{\alpha\beta}[k] \quad (3.24)$$

Applying (3.24) to (3.23) to convert from the $\alpha\beta$ reference frame to the DQ reference frame gives:

$$i_{dq}[k+1] = j e^{-j\omega k T_s} \cdot i_{\alpha\beta}[k+1] \cdot e^{-j\omega T_s}$$

$$i_{dq}[k+1] = (A_d i_{dq}[k] + B_d v_{t,dq}[k] - B_d v_{g,dq}[k]) \cdot e^{-j\omega T_s} \quad (3.25)$$

Due to the presence of the $e^{-j\omega T_s}$ term in (3.35), the dynamics of i_d and i_q are coupled like in the continuous-time equation of Chapter 2. To decouple these dynamics and compensate for the grid disturbance inputs v_{gd} and v_{gq} , a derivation of the feedforward terms needs to be performed so (3.25) becomes:

$$i_{dq}[k+1] = A_d i_{dq}[k] + B_d u_{dq}[k] \quad (3.26)$$

where u_{dq} : output of the PI compensators

Equating (3.25) and (3.26) yields:

$$\begin{aligned} (A_d i_{dq}[k] + B_d v_{t,dq}[k] - B_d v_{g,dq}[k]) \cdot e^{-j\omega T_s} &= A_d i_{dq}[k] + B_d u_{dq}[k] \\ v_{t,dq}[k] &= \frac{1}{B_d} \left([A_d i_{dq}[k] + B_d u_{dq}[k]] \cdot e^{j\omega T_s} - A_d i_{dq}[k] \right) + v_{g,dq}[k] \\ v_{t,dq}[k] &= u_{dq}[k] e^{j\omega T_s} - \frac{A_d}{B_d} (1 - e^{j\omega T_s}) i_{dq}[k] + v_{g,dq}[k] \end{aligned} \quad (3.27)$$

Separating (3.27) and replacing $e^{j\omega t}$ for its matrix form results in:

$$\begin{aligned} v_{t,d}[k] &= u_d[k] \cos(\omega T_s) - u_q[k] \sin(\omega T_s) - \frac{A_d}{B_d} [i_d[k] (1 - \cos(\omega T_s)) + i_q[k] \sin(\omega T_s)] + v_{g,d}[k] \\ v_{t,q}[k] &= u_q[k] \cos(\omega T_s) + u_d[k] \sin(\omega T_s) - \frac{A_d}{B_d} [i_q[k] (1 - \cos(\omega T_s)) - i_d[k] \sin(\omega T_s)] + v_{g,q}[k] \end{aligned} \quad (3.28)$$

Converting (3.28) to the z-domain gives:

$$\begin{aligned} V_{t,d}(z) &= U_d(z) \cos(\omega T_s) - U_q(z) \sin(\omega T_s) - \frac{A_d}{B_d} [I_d(z) (1 - \cos(\omega T_s)) + I_q(z) \sin(\omega T_s)] + V_{g,d}(z) \\ V_{t,q}(z) &= U_q(z) \cos(\omega T_s) + U_d(z) \sin(\omega T_s) - \frac{A_d}{B_d} [I_q(z) (1 - \cos(\omega T_s)) - I_d(z) \sin(\omega T_s)] + V_{g,q}(z) \end{aligned} \quad (3.29)$$

Now that the feedforward terms have been derived, the discretized plant state-space equation in the DQ reference frame (3.26) can be used to derive the control plant in the z-domain.

Applying the z-transformation to (3.26) yields:

$$zI_{dq}(z) = A_d I_{dq}(z) + B_d U_{dq}(z)$$

$$I_{dq}(z) = \frac{B_d}{z - A_d} U_{dq}(z) \quad (3.30)$$

Therefore, the discretized control plant becomes:

$$G_{Pd}(z) = \frac{B_d}{z - A_d} = \frac{1 - e^{-\frac{R_f T_s}{L_f}}}{z - e^{-\frac{R_f T_s}{L_f}}} \quad (3.31)$$

The second step is to let the compensator be a PI controller of the following form:

$$G_{Cd}(z) = \frac{k_{pd}(z-1) + k_{id}T_s}{z-1} \quad (3.32)$$

Next, the d-axis closed-loop transfer function will be derived with reference to Fig. 3.5:

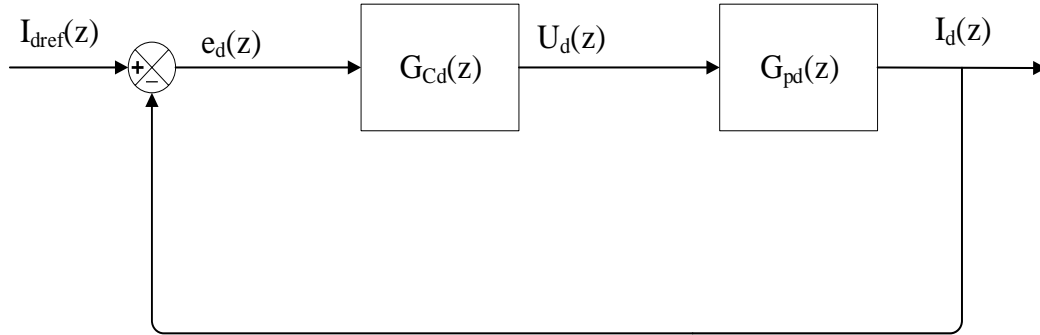


Figure 3.5: Simplified block diagram for current controlled VSC system in the z-domain

The open-loop gain of the control diagram shown in Fig. 3.5 is:

$$G_{ol}(z) = G_{Cd}(z)G_{Pd}(z)$$

$$G_{ol}(z) = \frac{k_{pd}(z-1) + k_{id}T_s}{z-1} \cdot \frac{B_d}{z-A_d} = k_{pd} \frac{(z-1 + \frac{k_{id}}{k_{pd}}T_s)}{z-1} \cdot \frac{B_d}{z-A_d} \quad (3.33)$$

Let $A_d = 1 - \frac{k_{id}}{k_{pd}}T_s$ to cancel one pole of (3.34) so that the open-loop gain reduces from a

second-order transfer function to a first-order transfer function as done in Chapter 2:

$$G_{ol}(z) = \frac{k_{pd}B_d}{z-1} \quad (3.34)$$

Then, the closed-loop gain is given by:

$$G_{cl}(z) = \frac{G_{ol}(z)}{1 + G_{ol}(z)}$$

$$G_{cl}(z) = \frac{k_{pd}B_d}{z + k_{pd}B_dT_s + 1} \quad (3.35)$$

The closed-loop pole is of the form of $e^{-\frac{T_s}{\tau_i}}$ and is a function of the system's time constant since (3.36) is a first-order transfer function. Thus, the settling time of this first-order closed-loop system will be as follows:

$$t_{i,settling} \approx 4.6\tau_i \quad (3.36)$$

Solving for the proportional and integral controller gains yields:

$$p_d(z) = 1 - k_{pd}B_dT_s = e^{-\frac{T_s}{\tau_i}}$$

$$k_{pd} = \frac{1 - e^{-\frac{T_s}{\tau_i}}}{B_d} = R_f \frac{1 - e^{-\frac{T_s}{\tau_i}}}{1 - e^{-\frac{R_f T_s}{L_f}}} \quad (3.37)$$

$$k_{id} = \frac{(1 - A_d)k_{pd}}{T_s} = R_f \frac{1 - e^{-\frac{T_s}{\tau_i}}}{T_s} \quad (3.38)$$

Now that the controller gains have been derived in the discrete domain, a simulation model is created to verify that the zero-order hold discretization method used in the derivation of Fig. 3.5 is valid. MATLAB/Simulink™ has been selected to model the simplified block diagram for current controlled VSC systems in the s-domain and z-domain to compare the responses of these systems to an input step change as shown in Fig. 3.6. The test parameters for the step response of the current loop controllers are presented in Table 3.2 where it should be noted that the discrete controller proportional and integral gains vary as a function of the sampling frequency. Fig 3.7 (a) shows satisfactory performance for all control loops when the sampling frequency is 4kHz by reaching to 98.8% of the final value at the settling time. However, utilizing the continuous control derived gains in a digitally controlled VSC can lead to poor performance when the sampling frequency is lowered as seen in Fig. 3.7(b) where overshoot is experienced which should not occur for a well-designed first order system.

Table 3.2 Test parameters for the current loop step response

Parameter	Symbol	Value
Sampling Frequency	f_s	4 kHz, 2 kHz, 1 kHz
Settling Time	$t_{i,settling}$	1.8 ms
Step Change Time	t_{step}	0.1 s
Step Magnitude	M_{step}	1 A
Filter Inductance	L_f	32.700 μ H
Filter Resistance	R_f	1.6 m Ω
Proportional Gain – Continuous Controller	K_p	0.0822
Integral Gain – Continuous Controller	K_i	4.0941
Proportional Gain – Discrete Controller	K_{pd}	0.0614, 0.0474, 0.0308
Integral Gain – Discrete Controller	K_{id}	3.0398, 2.3307, 1.4970

In fact, implementing these continuous-time derived gains results in an oscillatory response and a dramatical increase in the settling time when the sampling frequency becomes too low as shown in Fig. 3.7(c) where the response depicted by the black dashed line oscillates for much longer than the chosen settling time. In other words, the step response results presented in Fig 3.7 show that the current control designed in the z-domain, as done in the beginning of this section, has a very close response for all three switching frequencies when compared to that of the current control designed in the s-domain. Furthermore, both controllers were able to achieve a value with an error smaller than 2% at the settling time and followed a first-order transfer function response. Therefore, the derivation of the current loop in the z-domain utilizing the zero-order hold method is necessary and a valid approximation of the continuous s-domain control design.

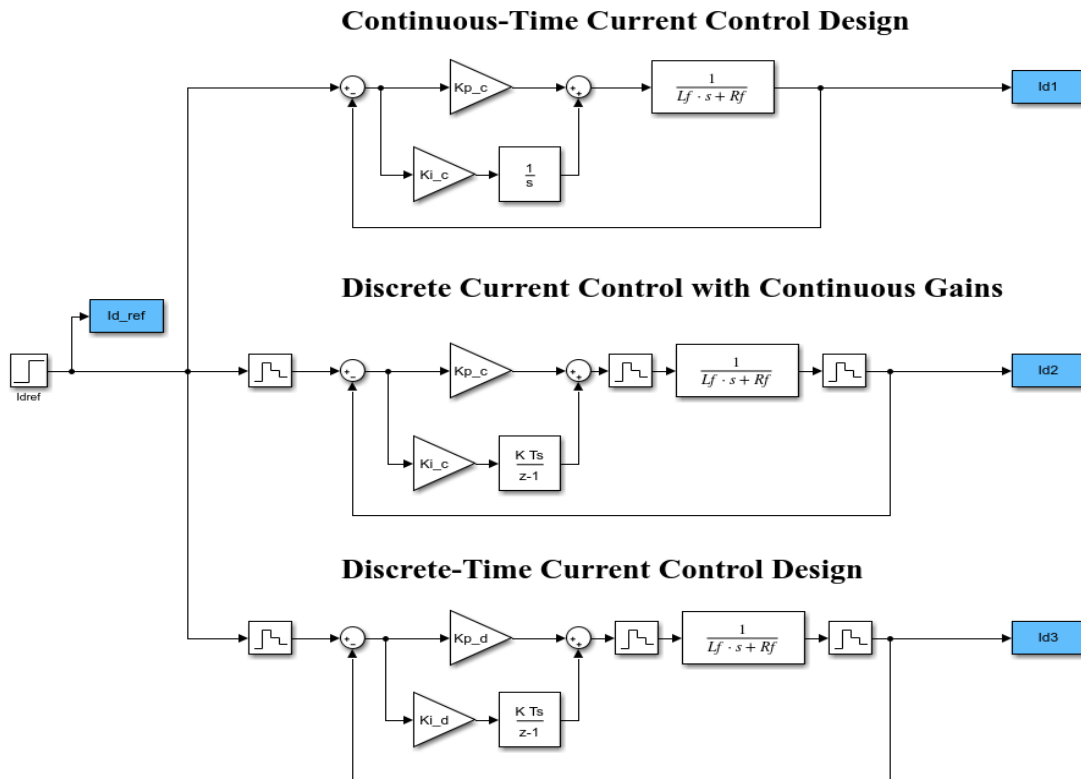
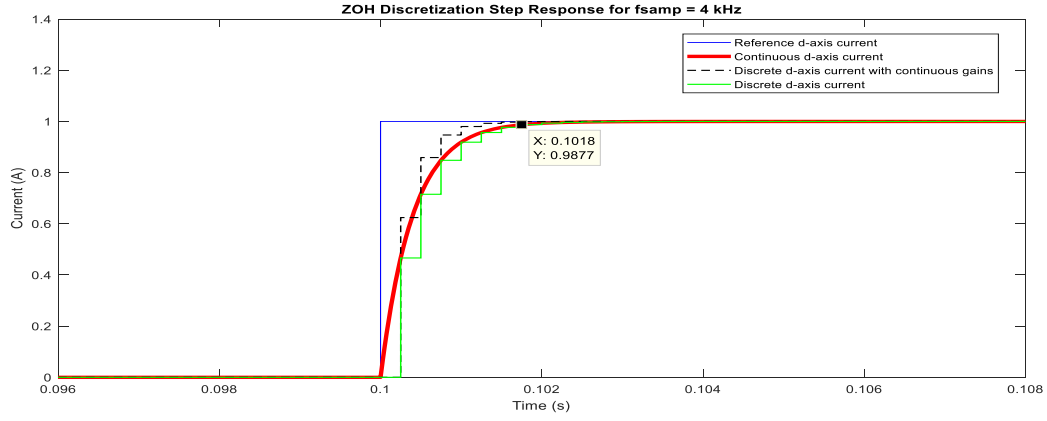
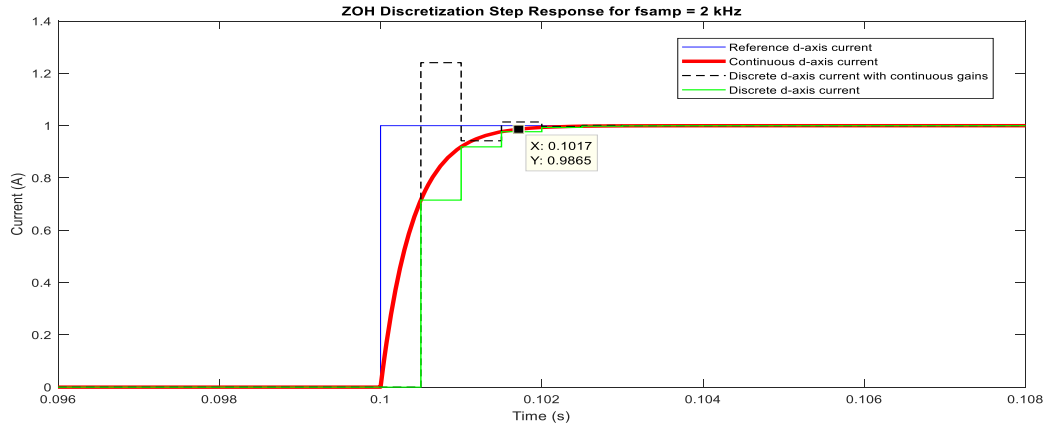


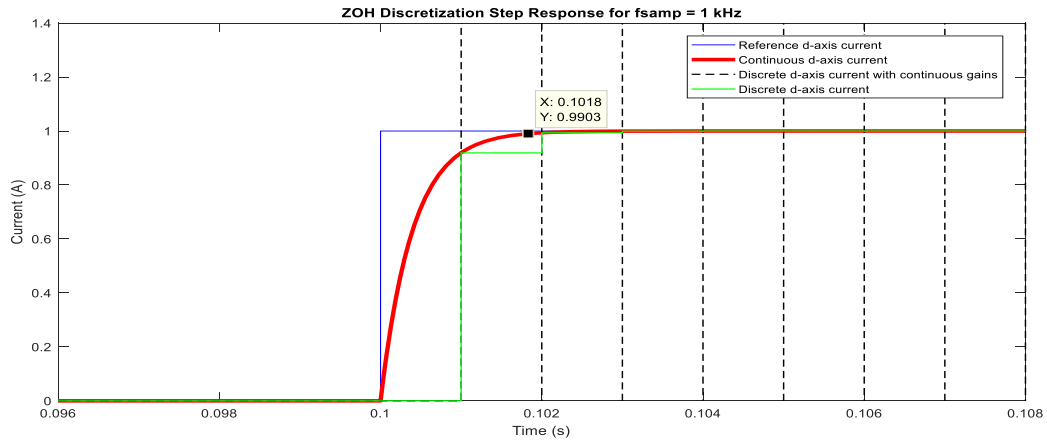
Figure 3.6: Simplified block diagram for current controlled VSC systems in Simulink



(a)



(b)



(c)

Figure 3.7: Step response comparison of the closed-loop current controls at different sampling frequencies: (a) 4 kHz, (b) 2 kHz and (c) 1 kHz

3.4 DC-Bus Voltage Control Loop Design in the Z-Domain

The control design of the DC-bus voltage controller in the z-domain is crucial for the digitally controlled VSC to work in rectifier mode. As a result, the discrete proportional and integral gains need to be derived as well as a pre-filter must be designed to ensure a second order response.

The first step to discretize the continuous control plant is to derive the plant state-space equation from (2.65) so it can be converted to the discrete-time domain.

$$\begin{aligned} C_{DC} \frac{dv_{DC}}{dt} &= i_{DC} - \frac{v_{DC}}{R_B} - i_L \\ \frac{dv_{DC}}{dt} &= -\frac{1}{C_{DC}R_B} v_{DC} + \frac{1}{C_{DC}} (i_{DC} - i_L) \end{aligned} \quad (3.39)$$

Let the standard state space-equation be:

$$\dot{x}(t) = Ax(t) + Bu(t) \quad (3.40)$$

Comparing (3.39) to (3.40) yields:

$$A = \left[-\frac{1}{C_{DC}R_B} \right] \quad B = \left[\frac{1}{C_{DC}} \right] \quad (3.41)$$

Applying the zero-order-hold discretization method to (3.40) by using the following property [3] gives:

$$\begin{aligned} e^{\begin{bmatrix} A & B \\ 0 & 0 \end{bmatrix} T_s} &= \begin{bmatrix} Ad & Bd \\ 0 & I \end{bmatrix} \\ A_d &= \left[e^{-\frac{T_s}{C_{DC}R_B}} \right] \quad B_d = \left[R_B - R_B e^{-\frac{T_s}{C_{DC}R_B}} \right] \end{aligned} \quad (3.42)$$

Therefore, applying (3.42) to (3.40) results in:

$$x[k+1] = A_d x[k] + B_d u[k] \quad (3.43)$$

and discretizing (3.39) yields:

$$\begin{aligned} v_{DC}[k+1] &= A_d v_{DC}[k] + B_d (i_{DC}[k] - i_L[k]) \\ v_{DC}[k+1] &= A_d v_{DC}[k] + B_d (u_d[k]) \end{aligned} \quad (3.44)$$

where u_d is the output of the PI compensator.

Applying the z-transformation to (3.44) yields:

$$\begin{aligned} zV_{DC}(z) &= A_d V_{DC}(z) + B_d (I_{DC}(z) - I_L(z)) \\ V_{DC}(z) &= \frac{B_d}{z - A_d} U_d(z) \end{aligned} \quad (3.45)$$

Therefore, the discretized control plant becomes:

$$G_{Pd}(z) = \frac{B_d}{z - A_d} = \frac{R_B - R_B e^{-\frac{T_s}{C_{DC} R_B}}}{z - e^{-\frac{T_s}{C_{DC} R_B}}} \quad (3.46)$$

The second step consist in deriving a relationship between the DC-bus voltage control loop and the current control loop because i_{DC} cannot be controlled directly but through the current drawn from the grid. Hence, the relationship between these systems assuming a lossless converter is [4]:

$$P_{3\phi} = P_{bus} \quad (3.47)$$

Substituting (2.59) into (3.47) and substituting for the DC-bus power yields:

$$-\frac{3}{2}v_{gd}i_d = i_{DC}V_{DC} \quad (3.48)$$

Let the time constant of the current control loop τ_i and the time constant of the DC bus voltage control loop τ_{DC} have the following relationship:

$$\tau_i \ll \tau_{DC} \quad (3.49)$$

If the condition in (3.49) is fulfilled, $i_d = I_{dref}(z)$ and both control loops are decoupled,

$$\begin{aligned} I_{dref}(z) &= -\frac{2}{3} \frac{V_{DC}}{v_{gd}} I_{DC}(z) \\ K_{inner} &= \frac{I_{DC}(z)}{I_{dref}(z)} = -\frac{3}{2} \frac{v_{gd}}{V_{DC}} \end{aligned} \quad (3.50)$$

The second step is to let the compensator be a PI controller of the following form:

$$G_{Cd}(z) = \frac{k_{pd}(z-1) + k_{id}T_s}{z-1} \quad (3.51)$$

Next, the d-axis closed-loop transfer function will be derived with reference to Fig. 3.8.

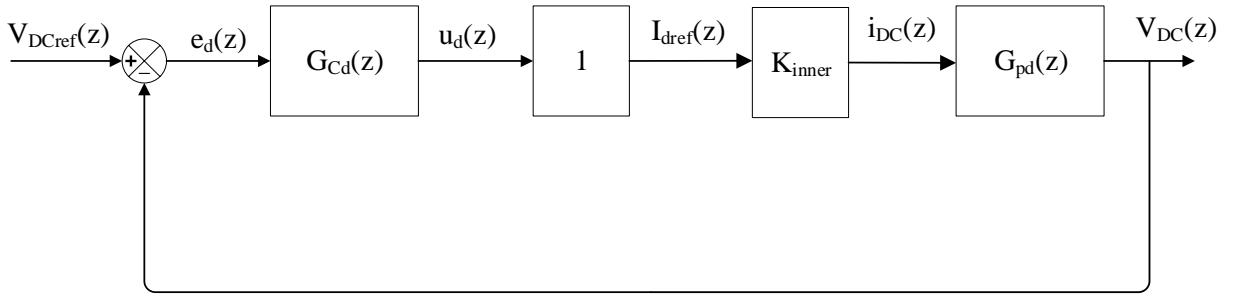


Figure 3.8: Simplified block diagram for DC-bus voltage loop of the VSC in the z-domain

Then, the open-loop gain is:

$$G_{ol}(z) = G_C(z)G_P(z)K_{inner}$$

$$G_{ol}(z) = \frac{k_{pd}(z-1) + k_{id}T_s}{z-1} \cdot \frac{B_d}{z-A_d} \cdot K_{inner} = B_d K_{inner} \frac{(k_{pd}z - k_{pd} + k_{id}T_s)}{z^2 - (A_d + 1)z + A_d} \quad (3.52)$$

and, the closed-loop gain is given by:

$$G_{cl}(z) = G_{DC}(z) = \frac{G_{ol}(z)}{1 + G_{ol}(z)} \quad (3.53)$$

$$G_{cl}(z) = \frac{B_d K_{inner} (k_{pd}z - k_{pd} + k_{id}T_s)}{z^2 + (B_d K_{inner} k_{pd} - A_d - 1)z + (A_d - B_d K_{inner} k_{pd} + B_d K_{inner} k_{id}T_s)}$$

Since (3.53) has a numerator of first order, a pre-filter will be implemented to cancel this term and be able to match (3.53) with the standard second-order transfer function which was given by (2.30); that is:

$$G_{PF}(z) = \frac{k_{id}T_s}{(k_{pd}z - k_{pd} + k_{id}T_s)} \quad (3.54)$$

Consequently multiplying (3.53) and (3.54) yields:

$$G_{DC}(z) = \frac{B_d K_{inner} k_{id}T_s}{z^2 + (B_d K_{inner} k_{pd} - A_d - 1)z + (A_d - B_d K_{inner} k_{pd} + B_d K_{inner} k_{id}T_s)} \quad (3.55)$$

Matching the denominator coefficients of (3.55) with (3.15) and solving for the proportional and integral controller gains results in:

$$k_{pd} = \frac{-2e^{-\zeta\omega_n T_s} \cos\left(\omega_n T_s \sqrt{1-\zeta^2}\right) + A_d + 1}{B_d K_{inner}} \quad (3.56)$$

$$k_{id} = \frac{e^{-2\zeta\omega_n T_s} - A_d + B_d K_{inner} k_{pd}}{B_d K_{inner} T_s} \quad (3.57)$$

Therefore, the settling time of this second-order closed-loop system is given by:

$$\tau_{DC} = \frac{1}{\zeta\omega_n} \quad (3.58)$$

$$t_{DC,settling} = 4.6 \cdot \tau_{DC}$$

To validate the derived discrete-time control gains, a Simulink model for the simplified block diagram for DC-bus voltage loop VSC systems in the s-domain and the z-domain as well as the second-order continuous transfer function is used to compare these systems as shown in Fig 3.9. The test parameters for the step response of the AC voltage controllers are presented in Table 3.3.

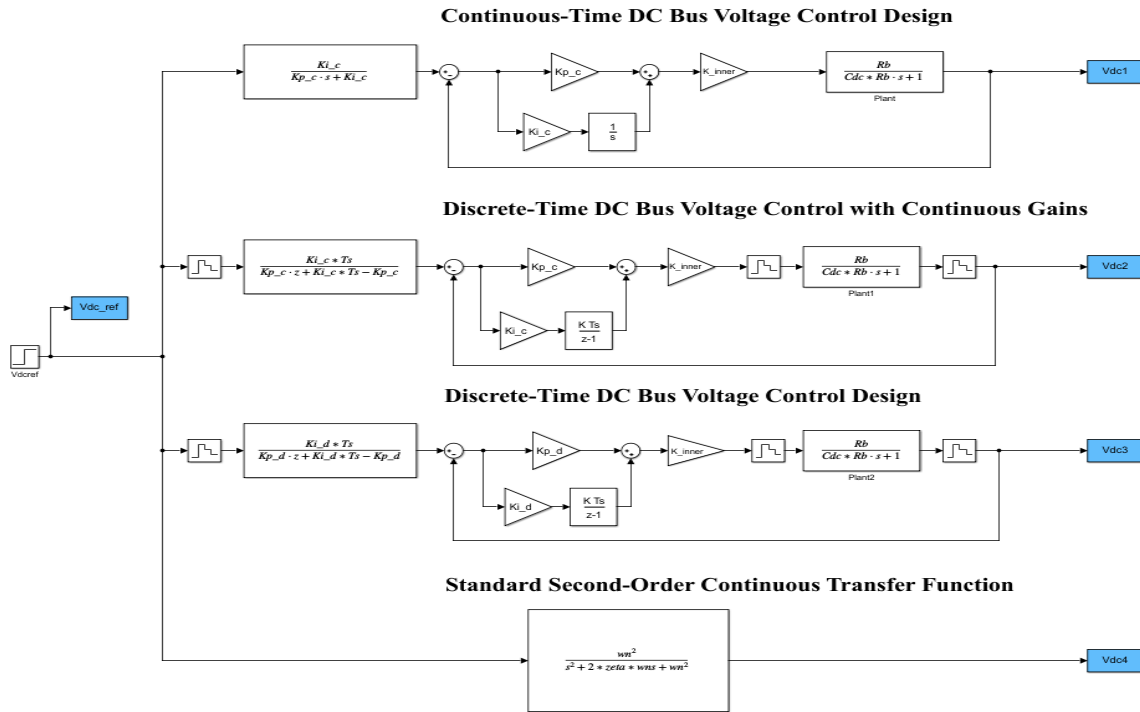


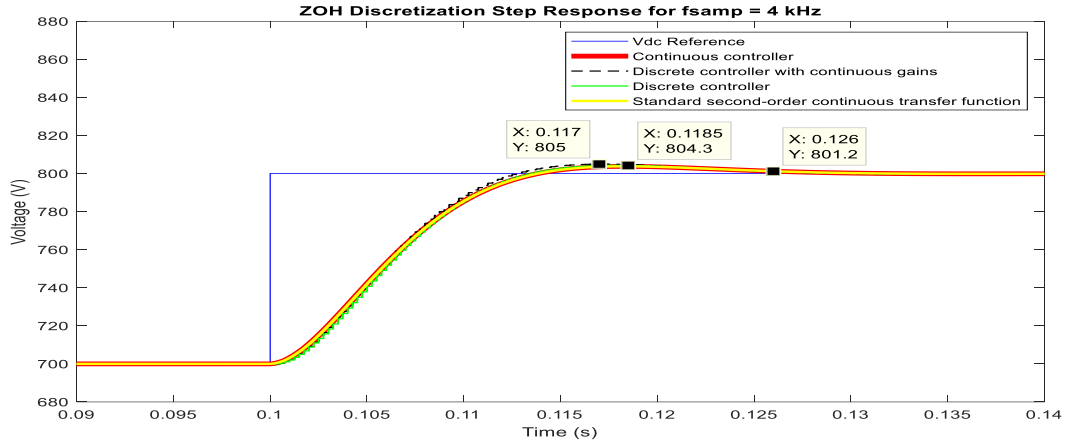
Figure 3.9: Simplified block diagram for DC-Bus voltage control loop for the VSC systems in Simulink

Table 3.3 Test parameters of the DC-bus voltage loop step response

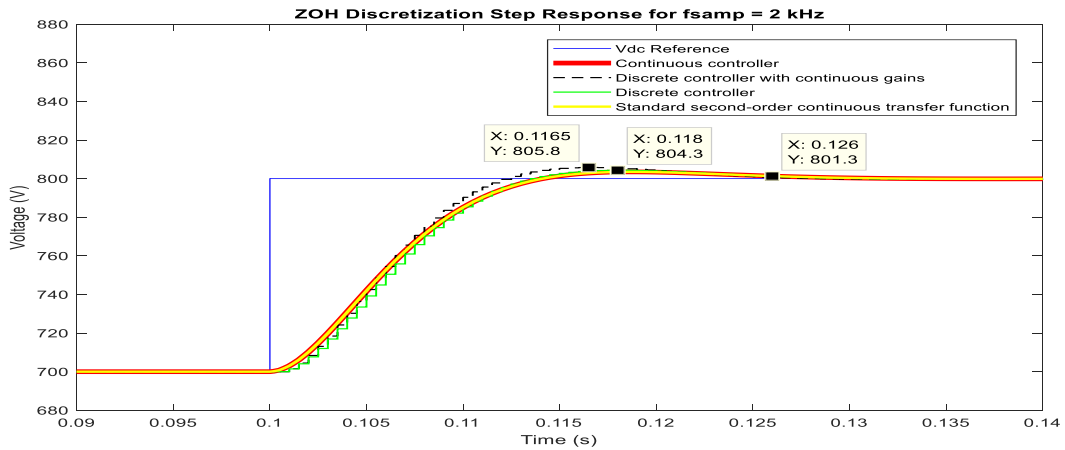
Parameter	Symbol	Value
Sampling Frequency	f_s	4 kHz, 2 kHz, 1 kHz
Settling Time	$t_{DC,settling}$	25.9 ms
Step Change Time	t_{step}	0.1 s
Step Magnitude	M_{step}	100 V
DC Bus Capacitance	C_{DC}	32.700 μ H
Bleeding Resistor	R_B	1.6 m Ω
Percentage Overshoot	PO	5%
Damping Factor	ζ	0.707
Natural Frequency	ω_n	65.06 rad/s
Proportional Gain – Continuous Controller	K_p	0.0822
Integral Gain – Continuous Controller	K_i	4.0941
Proportional Gain – Discrete Controller	K_{pd}	0.0614, 0.0474, 0.0308
Integral Gain – Discrete Controller	K_{id}	3.0398, 2.3307, 1.4970

It can be observed from the step response results shown in Fig 3.10 that the DC-bus voltage control designed in the z-domain has a very similar to that of the control designed in the s-domain. Also, both controllers were able to achieve a value with an error smaller than 2% at the settling time instant and a percentage overshoot of around 4% that followed the second-order transfer function response as shown in Fig 3.10 (a). Therefore, the derivation of DC-bus voltage control loop in the z-domain applying the zero-order hold method is needed and a valid approximation of the continuous s-domain control design.

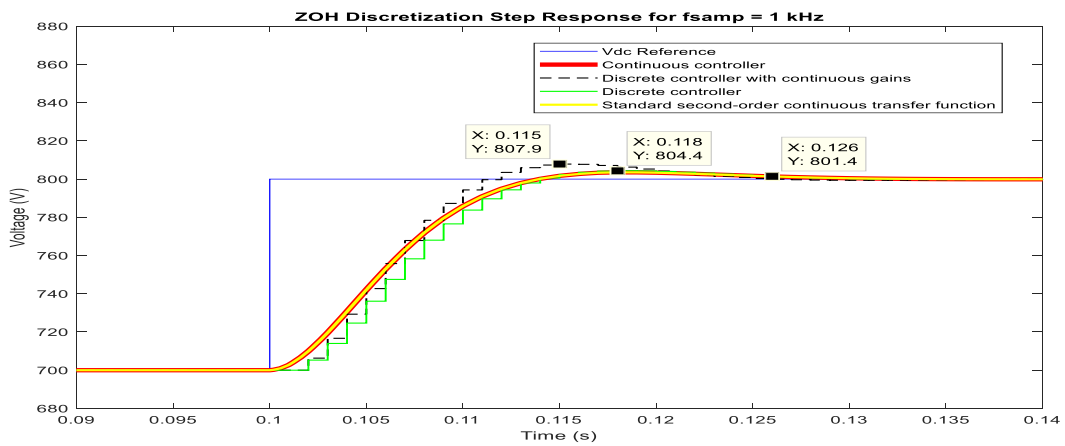
Another interesting result is that utilizing the continuous control derived gains in a digitally controlled VSC for the DC-bus voltage control loop did not perform as poorly as the case of the current control since this DC-bus voltage control loop is an outer one that is 10 times slower than the inner one. Fig. 3.7(b-c) show that the utilizing the s-domain gains in the digitally controlled system did not make the system unstable but the controller deviated from the desired response by having an overshoot of 5.8% at 2 kHz and 8% at 1 kHz unlike utilizing the z-domain derived gains.



(a)



(b)



(c)

Figure 3.10: Step response comparison of the closed-loop DC-bus voltage controls at different sampling frequencies: (a) 4 kHz, (b) 2 kHz and (c) 1 kHz

3.5 AC Voltage Control Loop Design in the Z-Domain

The control design of the AC voltage controller in the z-domain is crucial to control the VSC digitally in grid-forming mode. Consequently, the discrete proportional and integral gains need to be derived in the z-domain and a pre-filter should be designed to ensure a second-order system time response.

The continuous-time domain control plant in the $\alpha\beta$ frame (2.82) is discretized by deriving its state-space equation and then converting it to the DQ frame in the discrete-time domain as follows:

$$\begin{aligned} i_{Cf,\alpha\beta} &= i_{\alpha\beta} - i_{L,\alpha\beta} \\ \frac{d}{dt} v_{Cf,\alpha\beta} &= \frac{1}{C_f} (i_{\alpha\beta} - i_{L,\alpha\beta}) \end{aligned} \quad (3.59)$$

Let the standard state-space equation be:

$$\dot{x}(t) = Ax(t) + Bu(t) \quad (3.60)$$

Comparing (3.59) to (3.60) yields:

$$A = [0] \quad B = \left[\frac{1}{C_f} \right] \quad (3.61)$$

Applying the zero-order-hold discretization method to (3.61) by using the following property [3] gives:

$$\begin{aligned} e^{\begin{bmatrix} A & B \\ 0 & 0 \end{bmatrix} T_s} &= \begin{bmatrix} Ad & Bd \\ 0 & I \end{bmatrix} \\ A_d &= [1] \quad B_d = \left[\frac{T_s}{C_f} \right] \end{aligned} \quad (3.62)$$

Therefore, applying (3.62) to (3.60) results in:

$$x[k+1] = A_d x[k] + B_d u[k] \quad (3.63)$$

and discretizing (3.59) yields:

$$v_{Cf,\alpha\beta}[k+1] = A_d v_{Cf,\alpha\beta}[k] + B_d (i_{\alpha\beta}[k] - i_{L,\alpha\beta}[k]) \quad (3.64)$$

Applying (3.24) to (3.64) to convert from the $\alpha\beta$ reference frame to the DQ reference frame gives:

$$\begin{aligned} v_{Cf,dq}[k+1] &= j e^{-j\omega k T_s} \cdot v_{Cf,\alpha\beta}[k+1] \cdot e^{-j\omega T_s} \\ v_{Cf,dq}[k+1] &= (A_d v_{Cf,dq}[k] + B_d i_{dq}[k] - B_d i_{L,dq}[k]) \cdot e^{-j\omega T_s} \end{aligned} \quad (3.65)$$

Due to the presence of the $e^{-j\omega T_s}$ term in (3.65), the dynamics of $v_{Cf,d}$ and $v_{Cf,q}$ are coupled like in the continuous time equation of Chapter 2. To decouple these dynamics and compensate for the current flowing to the load i_{Ld} and i_{Lq} , a derivation of the feedforward terms needs to be performed so that (3.65) becomes:

$$v_{Cf,dq}[k+1] = A_d v_{Cf,dq}[k] + B_d u_{dq}[k] \quad (3.66)$$

where u_{dq} : output of the PI compensators

Equating (3.65) and (3.66) yields:

$$\begin{aligned} (A_d v_{Cf,dq}[k] + B_d i_{dq}[k] - B_d i_{L,dq}[k]) \cdot e^{-j\omega T_s} &= A_d v_{Cf,dq}[k] + B_d u_{dq}[k] \\ i_{dq}[k] &= \frac{1}{B_d} \left([A_d v_{Cf,dq}[k] + B_d u_{dq}[k]] \cdot e^{j\omega T_s} - A_d v_{Cf,dq}[k] \right) + i_{L,dq}[k] \end{aligned}$$

$$v_{t,dq}[k] = u_{dq}[k]e^{j\omega T_s} - \frac{A_d}{B_d}(1 - e^{j\omega T_s})v_{cf,dq}[k] + i_{L,dq}[k] \quad (3.67)$$

Separating (3.67) and replacing $e^{j\omega T_s}$ for its matrix form results in:

$$\begin{aligned} i_d[k] &= u_d[k]\cos(\omega T_s) - u_q[k]\sin(\omega T_s) - \frac{A_d}{B_d} \left[v_{cf,d}[k](1 - \cos(\omega T_s)) + i_q[k]\sin(\omega T_s) \right] + i_{L,d}[k] \\ i_q[k] &= u_q[k]\cos(\omega T_s) + u_d[k]\sin(\omega T_s) - \frac{A_d}{B_d} \left[v_{cf,q}[k](1 - \cos(\omega T_s)) - i_d[k]\sin(\omega T_s) \right] + i_{L,q}[k] \end{aligned} \quad (3.68)$$

Converting (3.68) to the z-domain gives:

$$\begin{aligned} I_d(z) &= U_d(z)\cos(\omega T_s) - U_q(z)\sin(\omega T_s) - \frac{A_d}{B_d} \left[V_{cf,d}(z)(1 - \cos(\omega T_s)) + U_q(z)\sin(\omega T_s) \right] + I_{L,d}(z) \\ I_q(z) &= U_q(z)\cos(\omega T_s) + U_d(z)\sin(\omega T_s) - \frac{A_d}{B_d} \left[V_{cf,q}(z)(1 - \cos(\omega T_s)) - U_d(z)\sin(\omega T_s) \right] + I_{L,q}(z) \end{aligned} \quad (3.69)$$

Let the time constant of the current control loop τ_i and the time constant of the AC voltage control loop τ_v have the following relationship:

$$\tau_i \ll \tau_v \quad (3.70)$$

If the condition in (3.70) is fulfilled, $I_{dq}(z) = I_{dqref}(z)$ and both inner and outer control loops are decoupled. Thus, the discretized plant state space equation in the DQ reference frame (3.66) can be used to derive the control plant in the z-domain since the feedforward terms have been derived. Applying Z transform to (3.66) yields:

$$zV_{cf,dq}(z) = A_d V_{cf,dq}(z) + B_d U_{dq}(z)$$

$$V_{cf,dq}(z) = \frac{B_d}{z - A_d} U_{dq}(z) \quad (3.71)$$

Therefore, the discretized control plant becomes:

$$G_{Pd}(z) = \frac{B_d}{z - A_d} = \frac{T_s/C_f}{z - 1} \quad (3.72)$$

Let the compensator be a PI controller of the following form:

$$G_{Cd}(z) = \frac{k_{pd}(z-1) + k_{id}T_s}{z-1} \quad (3.73)$$

Next, the d-axis closed-loop transfer function will be derived with reference to Fig. 3.11.

The open-loop gain of the control diagram shown in Fig. 3.11 is:

$$\begin{aligned} G_{ol}(z) &= G_{Cd}(z)G_{Pd}(z) \\ G_{ol}(z) &= \frac{k_{pd}(z-1) + k_{id}T_s}{z-1} \cdot \frac{B_d}{z - A_d} = \frac{B_d(k_{pd}z - k_{pd} + k_{id}T_s)}{z^2 - (A_d + 1)z + A_d} \end{aligned} \quad (3.74)$$

Then, the closed-loop gain is given by:

$$\begin{aligned} G_{cl}(z) &= G_v(z) = \frac{G_{ol}(z)}{1 + G_{ol}(z)} \\ G_{cl}(z) &= \frac{B_d(k_{pd}z - k_{pd} + k_{id}T_s)}{z^2 + (B_d k_{pd} - A_d - 1)z + (A_d - B_d k_{pd} + B_d k_{id}T_s)} \end{aligned} \quad (3.75)$$

Since (3.75) has a numerator of first order, a pre-filter will be implemented to cancel this term and be able to match (3.75) with the standard second-order transfer function which was given by (2.30); that is:

$$G_{PF}(z) = \frac{k_{id}T_s}{(k_{pd}z - k_{pd} + k_{id}T_s)} \quad (3.76)$$

Consequently multiplying (3.75) and (3.76) yields:

$$G_v(z) = \frac{B_d k_{id} T_s}{z^2 + (B_d k_{pd} - A_d - 1)z + (A_d - B_d k_{pd} + B_d k_{id} T_s)} \quad (3.77)$$

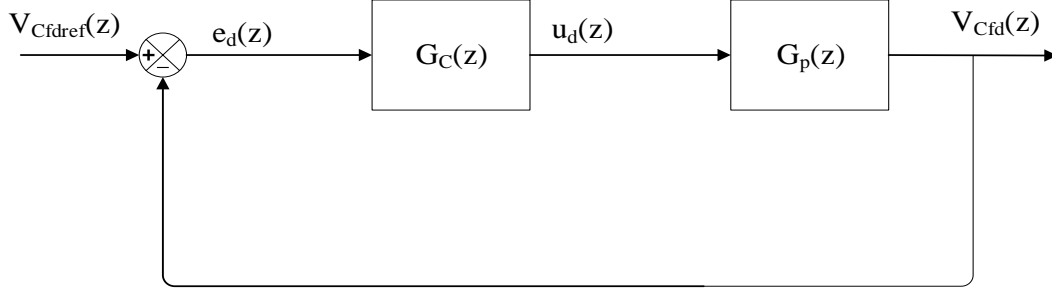


Figure 3.11: Simplified block diagram for AC voltage loop of the VSC in the z-domain

Matching the denominator coefficients of (3.77) with (3.15) and solving for the proportional and integral controller gains results in:

$$k_{pd} = \frac{-2e^{-\zeta\omega_n T_s} \cos\left(\omega_n T_s \sqrt{1-\zeta^2}\right) + A_d + 1}{B_d} \quad (3.78)$$

$$k_{id} = \frac{e^{-2\zeta\omega_n T_s} - A_d + B_d k_{pd}}{B_d T_s} \quad (3.79)$$

Therefore, the settling time of this second-order closed-loop system is given by:

$$\begin{aligned} \tau_v &= \frac{1}{\zeta\omega_n} \\ t_{v,settling} &= 4.6 \cdot \tau_v \end{aligned} \quad (3.80)$$

To confirm that the discrete-time control gains derived above lead to a second-order time response just as that of the classical second-order transfer function and the continuous-time gains derived in the previous chapter, a step response test of the AC voltage controllers is performed with the parameters presented in Table 3.3 and utilizing the Simulink model shown in Fig. 3.12. The step response results for different sampling frequencies are shown in Fig. 3.13. It can be noted that the results are very similar to those in presented for the DC-bus voltage loop because both control loops follow the same condition (3.70) and therefore the conclusion is the identical.

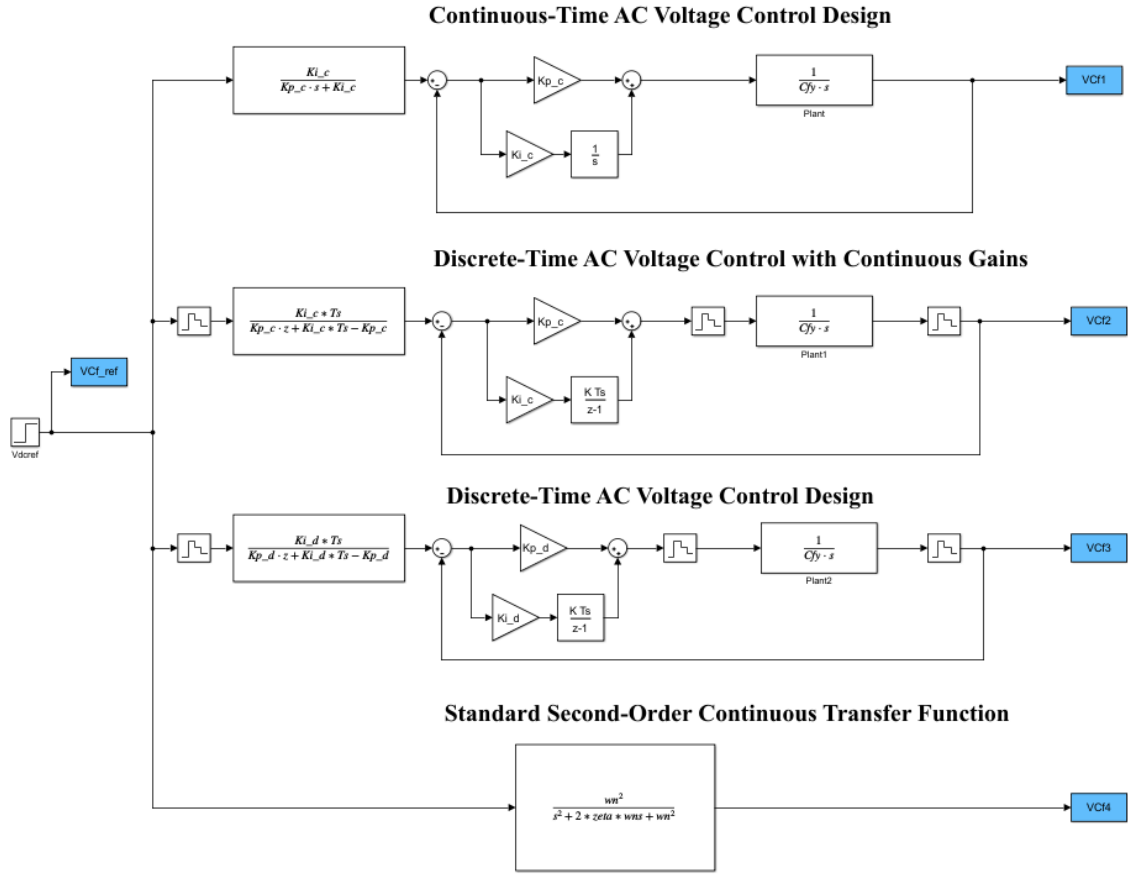
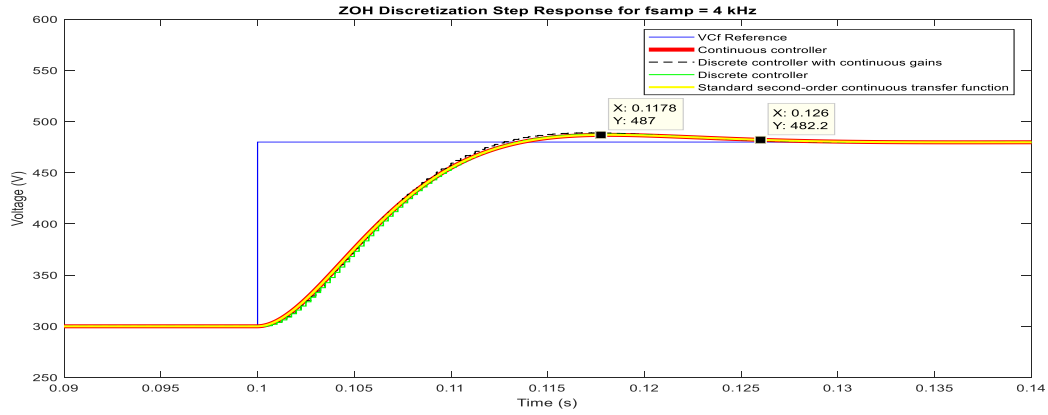


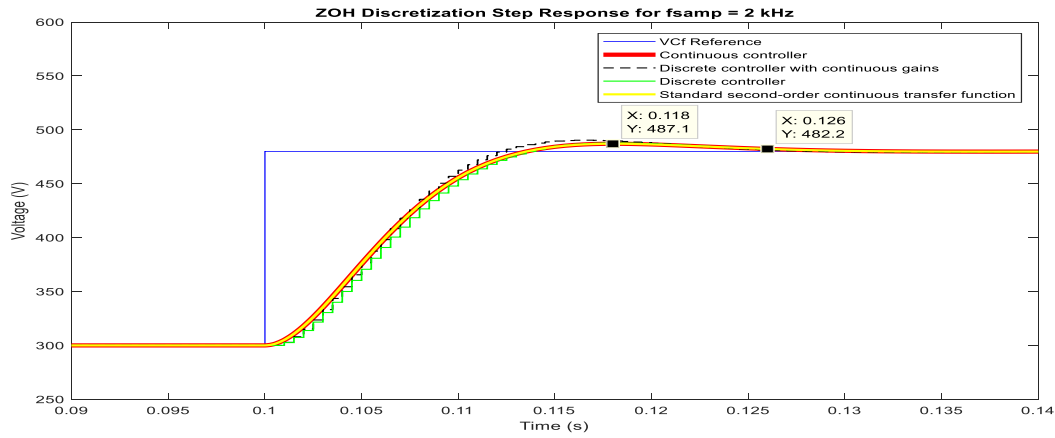
Figure 3.12: Simplified block diagram for AC voltage loop for the VSC systems Simulink model

Table 3.4 Test parameters of the AC voltage control loop step response

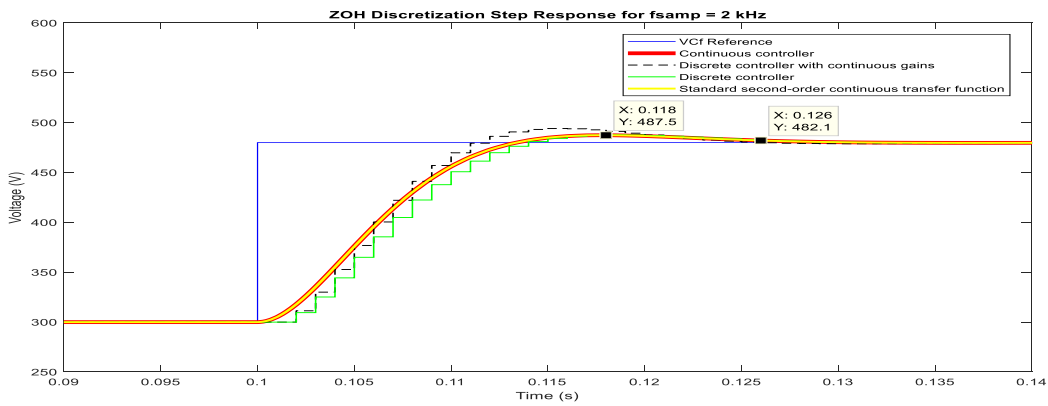
Parameter	Symbol	Value
Sampling Frequency	f_s	4 kHz, 2 kHz, 1 kHz
Settling Time	$t_{v,settling}$	25.9 ms
Step Change Time	t_{step}	0.1 s
Step Magnitude	M_{step}	180 V
Filter Capacitance	C_{DC}	1440 μ F
Percentage Overshoot	PO	5%
Damping Factor	ζ	0.707
Natural Frequency	ω_n	251.33 rad/s
Proportional Gain – Continuous Controller	K_p	0.5117
Integral Gain – Continuous Controller	K_i	90.9583
Proportional Gain – Discrete Controller	K_{pd}	0.5114, 0.5105, 0.5068
Integral Gain – Discrete Controller	K_{id}	87.0061, 83.2257, 76.1506



(a)



(b)



(c)

Figure 3.13: Step response comparison of the closed-loop AC voltage controls at different sampling frequencies: (a) 4 kHz, (b) 2 kHz and (c) 1 kHz

3.6 Concluding Remarks

This chapter has reviewed the derivation of the control design in z-domain and conversion from the s-domain to the z-domain utilizing the zero-order discretization method. This included the phase lock loop, current control loop, DC bus control loop and AC voltage control loop design derivation. Also, the step response comparison between the continuous and discrete time domain implementation of the control loops was performed and it can be concluded that the discretization method used in this chapter is valid and a good approximation of the standard second-order transfer function time response. Moreover, utilizing the continuous gains derived in the previous chapter in a discrete controller results in a satisfactory performance as long as the sampling frequency is high enough and the discrete controller approximates to the continuous controller. The next chapter will focus on the implementation of the Simulink model and simulation of a high power microgrid testbed.

3.7 References

- [1] Phillips, Charles L., and H. Troy. Nagle. "System Time-Response Characteristics." *Digital Control System: Analysis and Design*, Prentice-Hall, 1995.
- [2] Dorf, Richard C., et al. "The Performance of Feedback Control Systems." *Modern Control Systems*, Pearson, 2011.
- [3] Åström Karl J. and Wittenmark Björn, *Computer-controlled systems theory and design*. Mineola, NY: Dover Publications, 2011.

CHAPTER 4

MICROGRID PRIMARY AND SECONDARY CONTROLLERS

4.1 Introduction

This chapter deals with the implementation of the primary controller for different microgrid applications as well as the demonstration of a role of the secondary controller for a distribution-level microgrid.

The primary controller is in charge of regulating locally low-level variables such as frequency, voltage and current injection in the VSCs. The control of these variables is also known as the “zero-level microgrid control” which corresponds to the various modes that power converters can be controlled depending on their operation in the AC microgrid. These modes are classified as grid-feeding, grid-forming and grid-supporting in [1], and are made of cascading the voltage and current control loops derived in Chapter 3. The primary controller also deals with ensuring a proper power sharing between multiple DERs and a stable microgrid operation [2]. Therefore, it manages the load sharing among the DERs of the microgrid by implementing independent active and reactive power sharing methods such as droop and virtual impedance techniques as well as active load sharing algorithms in order to avoid undesired circulating currents [3].

The secondary controller works as a “centralized automatic controller” that compensates for the frequency and voltage deviations in the microgrid by using low-bandwidth communication systems to sense these parameters at specific points of the microgrid and comparing them with the reference values [4]. It then utilizes communications and wide-area monitoring systems to send output reference commands to the primary controllers of each DER

to ensure that the microgrid remains within its operational limits at any point of the structure. The secondary control coordinates these actions with a time response in the range of minutes, thus having slower dynamics than the primary control [1].

4.2 Grid-Feeding Mode

A converter operating in grid-feeding mode acts as a current source with a high parallel impedance that injects power into the grid at PCC. This mode is very common in grid-tied applications and consists of cascading several control loops and a PLL loop to synchronize with the grid voltage in order to regulate the power injected. Therefore, this mode relies in the inner current control loop for its fast response and uses the outer loop to produce the current reference commands that are fed to the inner loop. The most broadly used controllers for this implementation in three-phase systems are the PI controllers that are designed in the DQ synchronous reference frames because they have the particular advantage of controlling the active and reactive currents directly as shown in Chapter 3.

The power reference is usually provided by the primary controller based on load sharing techniques, the Maximum Power Point Tracking (MPPT) algorithm to extract the most power from the energy source, the secondary controller for microgrid voltage and frequency regulation or the tertiary controller for optimization purposes. Two implementations of the grid-feeding mode are presented below: the PQ Open-loop Control and the DC Voltage Regulator.

4.2.1 PQ Open-loop Control

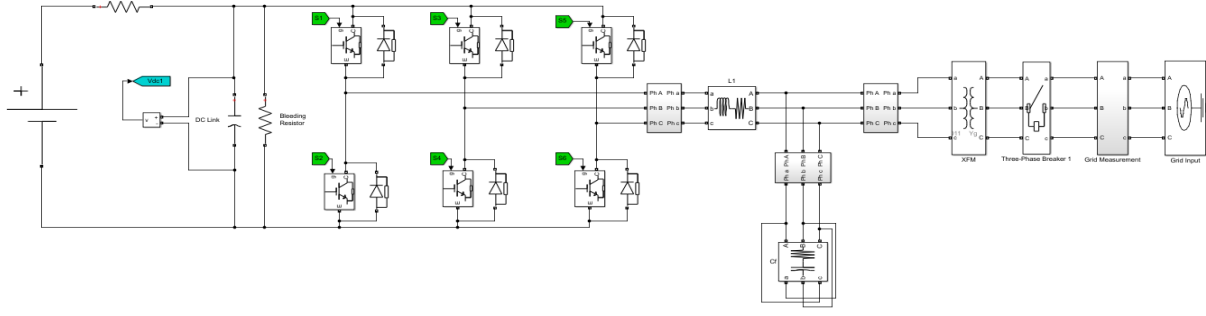


Figure 4.1: PQ grid-feeding Simulink model

This grid feeding method consists of converting the active and reactive power references into the references for the inner current control loop with the equations shown in section 3.3 and have the PI controller regulate the output current. However, this implementation does not include a DC-Bus voltage control loop and therefore its DC voltage should be controlled by another converter or provided by a stiff DC source as shown in the simulation model in Fig. 4.1. Prior to the realization of the PQ control, the voltage feedback signals have to be measured and fed to the PLL to calculate the angle theta θ in order to perform the ABC-DQ transformation of the current feedback signal and the feed-forward voltage. The control diagram for the PQ open-loop control is shown in the figure below:

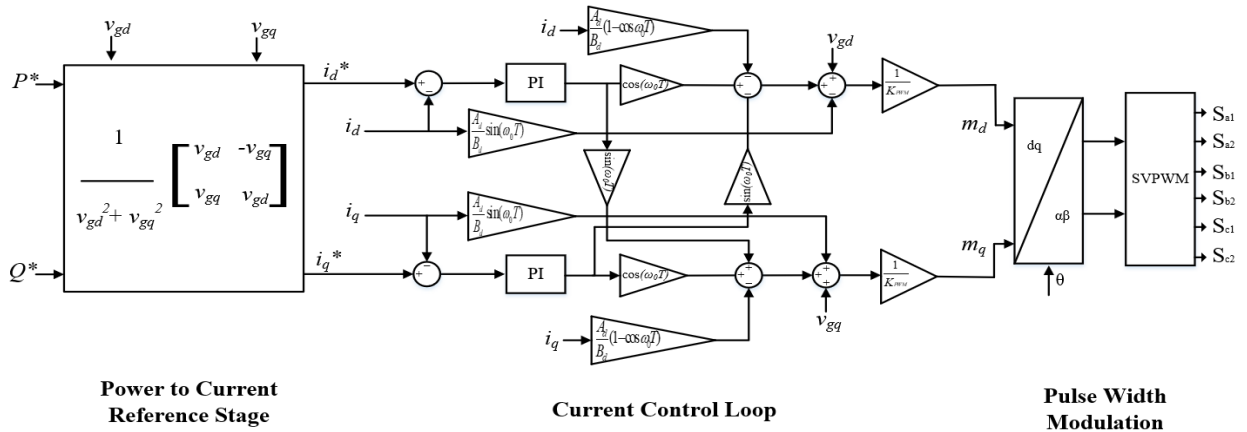


Figure 4.2: PQ grid-feeding control diagram

This control diagram shows that PQ open-loop implementation of the grid-feeding mode consists of three main stages: the power to current reference phase that converts the active and reactive power references given by higher a level controller into a current reference in the DQ frame that is fed to the current control loop phase. This second phase uses a PI controller to adjust the modulation index which is given to the PWM algorithm until the current feedback signal becomes the same as the reference signal. Then, the SVPWM phase creates the corresponding pulses that are sent to the gates of the transistors of the VSC.

The simulation model shown in Fig. 4.1 which is composed of a three-phase converter with a LC filter, a transformer and the utility grid is used to validate the control diagram shown in Fig. 4.2 in which a converter injects the commanded power to the grid. The parameters for the components of the simulation are presented in the table below:

Table 4.1 Test Parameters for the PQ open-loop control simulation

Parameter	Symbol	Value
Main Grid Line to Line Voltage	V_{PCC}	13.8 kV
Inverter Rated Output Voltage	V_o	480 V
DC Link Capacitor Voltage	V_{DC}	750 V
Inverter Rated Power	S_B	2 MVA
Fundamental Frequency	f_B	60 Hz
Switching Frequency	f_s	4 kHz
Controller Sampling Frequency	f_{smp}	8 kHz
DC-Link Capacitor	C_{DC}	37.8 mF
AC Filter Capacitor Delta Connection	C_f	480 μ F
AC Filter Capacitor ESR	RC_f	0.2 m Ω
AC Filter Inductor Converter-Side	L_{f1}	46 μ H
AC Filter Inductor Converter-Side ESR	RL_{f1}	1.6 m Ω
Transformer Equivalent Series Inductance	L_{f2}	13 μ H
Transformer Equivalent Series Resistance	RL_{f2}	0.26 m Ω
Current Loop Proportional Gain	K_{pcd}	0.0689
Current Loop Integral Gain	K_{icd}	2.7060
PLL Settling Time	T_{s_PLL}	30 ms
Active Power Reference	P_{ref}	2 MW
Reactive Power Reference	Q_{ref}	0 VAR

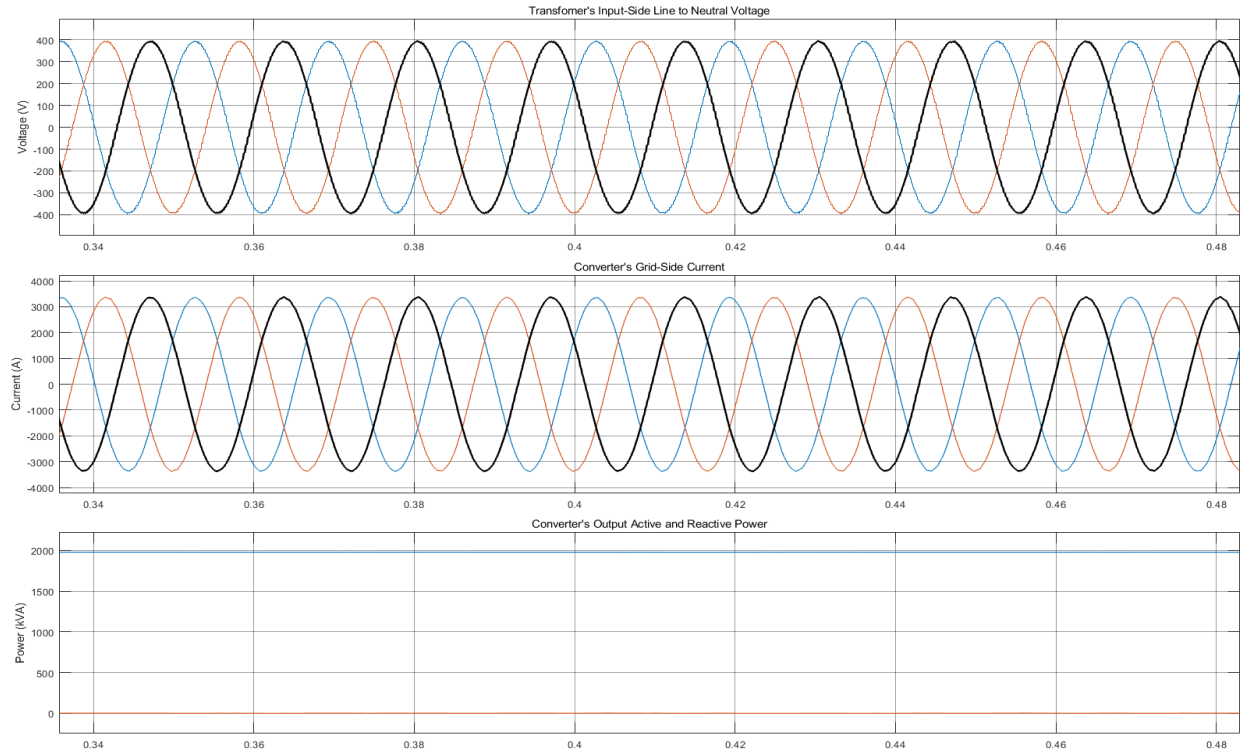


Figure 4.3: PQ grid-feeding simulation results

The results of the PQ grid-feeding test are shown in the figure above in which the output voltages and currents have sinusoidal waveforms with very low harmonic contents and the correct amount of power is fed to the grid.

4.2.2 DC Voltage Regulator

While the PQ controllers deal with the AC power injection directly and leave the DC link voltage regulation to a stiff DC source, these sources are not always available; particularly, for distributed renewables resources, a power converter such as a DC/DC converter is needed to regulate the DC link voltage. Alternatively, the voltage regulation of the DC bus can be achieved by the same inverter utilizing the control diagrams shown below. This technique is used when inverters are connected directly to intermittent energy sources such as PV arrays, or indirectly in wind turbines through another converter that controls the generator.

Table 4.2 Perturb and observe algorithm process

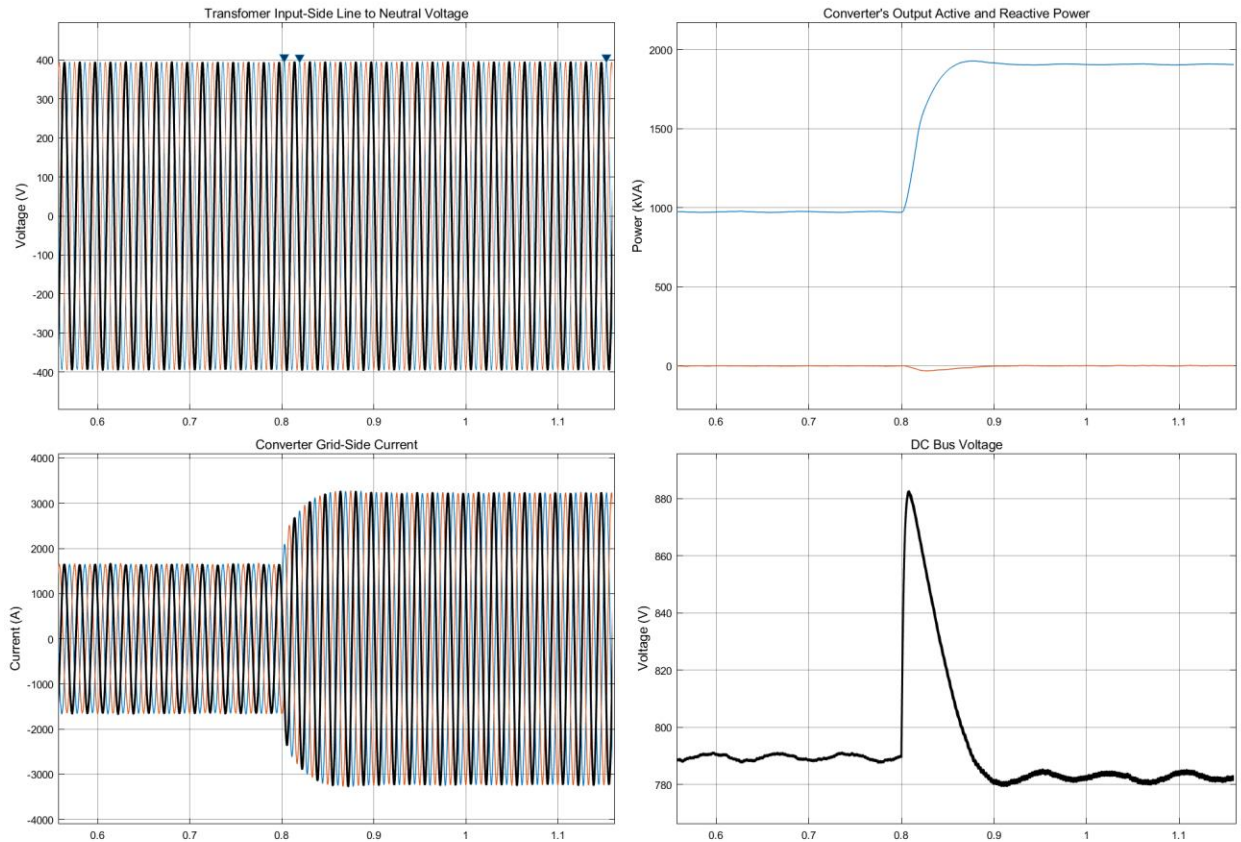
Voltage Perturbation	Change in Power	Next Perturbation
Positive	Positive	Positive
Positive	Negative	Negative
Negative	Positive	Negative
Negative	Negative	Positive

In the case of PV arrays, the current and voltage vary depending on the sun irradiance and cell temperature. Therefore, these energy sources are not stiff and require a DC regulator to adjust the voltage level depending on the conditions at different points in time in order to extract the most power from the array. The DC voltage reference is given by an MPPT algorithm that finds the maximum power point (MPP) voltage at a given instance. The Perturb & Observe (P&O) MPPT method works by varying the voltage and observing the power output. Thus, if there is an increase in power, the subsequent perturbation is kept in the same directions increasing it, and if there is a decrease in power, the perturbation is reversed [5]. This algorithm is summarized in Table 4.2 and this process is repeated periodically until the MPP is reached. There are some tradeoffs with this technique because the system then oscillates about the MPP voltage. The oscillation can be minimized by reducing the perturbation step size. Nevertheless, a smaller perturbation size slows down the MPPT settling time. There are optimized versions of this algorithm that deal with that situation [6-7]. However, their implementation is out of the scope of this thesis.

The control diagram in Fig. 4.4 shows the DC voltage regulator implementation for the grid-feeding mode consisting in cascading the DC bus voltage and current control loops presented in Chapter 3 and a MPPT algorithm that provides the DC bus voltage reference.

Table 4.3 Test parameters for the DC voltage regulator control simulation

Parameter	Symbol	Value
Inverter Rated Output Voltage	V_o	480 V
Inverter Rated Power	S_B	2 MVA
Fundamental Frequency	f_B	60 Hz
Switching Frequency	f_s	4 kHz
Controller Sampling Frequency	f_{samp}	8 kHz
DC-Link Capacitor	C_{DC}	37.8 mF
AC Filter Capacitor Delta Connection	C_f	480 μF
AC Filter Inductor Converter-Side	L_{f1}	46 μH
Transformer Equivalent Series Inductance	L_{f2}	13 μH
Current Loop Proportional Gain	K_{pcd}	0.0689
Current Loop Integral Gain	K_{icd}	2.7060
DC Voltage Control Loop Proportional Gain	K_{pvdc}	-6.9421
DC Voltage Control Loop Integral Gain	K_{ivdc}	-432.82
Sun Irradiance	I_r	500, 1000 W/m^2
Cell Temperature	T	25 $^{\circ}\text{C}$
MPP Voltage	V_{MPP}	780 V
Maximum Power	P_{MAX}	1.94 MW

**Figure 4.6: PQ grid-feeding simulation results**

The results shown in Fig. 4.5 illustrate, at 0.8 there is a step increase in the irradiance that translates into an increase of power generation and a spike in the voltage. Therefore, the MPPT controller starts to decrease the voltage until the power change becomes negative and the new MPP voltage is determined. Then, the voltage oscillates around this point due to the nature of the algorithm.

4.3 Grid-Forming Mode

When the microgrid is disconnected from the main network and works in the island mode, a grid-forming converter is in charge of setting the frequency and voltage of the microgrid. The operation principle for this converter comes from an uninterrupted power source (UPS) with energy storage capability to supply the electrical loads without power from the grid [8]. The control structure of a grid-forming power converter consists of two cascaded loops, as depicted in Fig. 4.7. The external loop is in charge of regulating the output AC voltage by varying the inner loop current reference just as the DC voltage regulator mode shown previously. Since this mode creates its own reference frequency, other grid-feeding and grid-supporting inverters must synchronize by means of the PLL algorithm with the output voltage of this inverter.

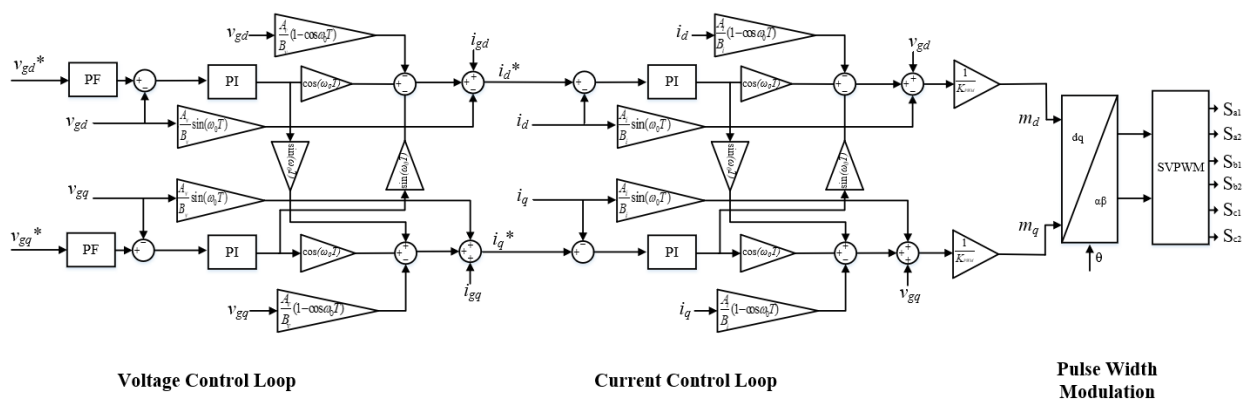


Figure 4.7: Grid-forming Control Diagram

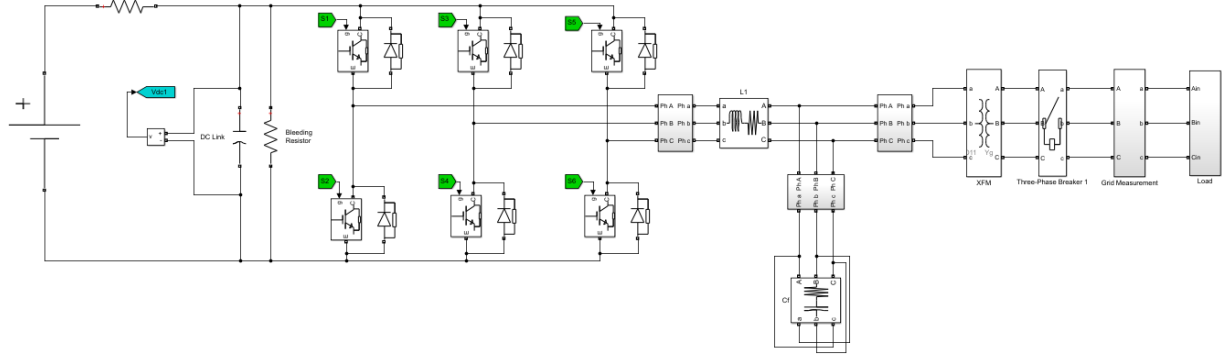


Figure 4.8: Grid-forming Simulink model

The simulation model shown in Fig. 4.8 shows an inverter in grid-forming mode connected to a transformer to step up the voltage from 480 V to 13.8 kV in order to provide the proper voltage to the load. The inverter is supplied by a DC source that can mimic the energy storage system of an UPS. Also, the parameters used in this simulation are presented in Table 4.4 which are most of the converter values used in past tests.

Table 4.4 Test parameters for the grid-forming simulation

Parameter	Symbol	Value
Main Grid Line to Line Voltage	V_{PCC}	13.8 kV
Inverter Rated Output Voltage	V_o	480 V
DC Link Capacitor Voltage	V_{DC}	750 V
Inverter Rated Power	S_B	2 MVA
Fundamental Frequency	f_B	60 Hz
Switching Frequency	f_s	4 kHz
Controller Sampling Frequency	f_{samp}	8 kHz
DC-Link Capacitor	C_{DC}	37.8 mF
AC Filter Capacitor Delta Connection	C_f	480 μ F
AC Filter Capacitor ESR	RC_f	0.2 m Ω
AC Filter Inductor Converter-Side	L_{fl}	46 μ H
AC Filter Inductor Converter-Side ESR	RL_{fl}	1.6 m Ω
Current Loop Proportional Gain	K_{ped}	0.1987
Current Loop Integral Gain	K_{icd}	8.9182
AC Voltage Control Loop Proportional Gain	K_{pvdc}	2.8062
AC Voltage Control Loop Integral Gain	K_{ivdc}	1367.2
Load Active Power	P_L	1.2 MW, 0.8 MW
Load Reactive Power	Q_L	0.3 MVAR, 0.57 MVAR

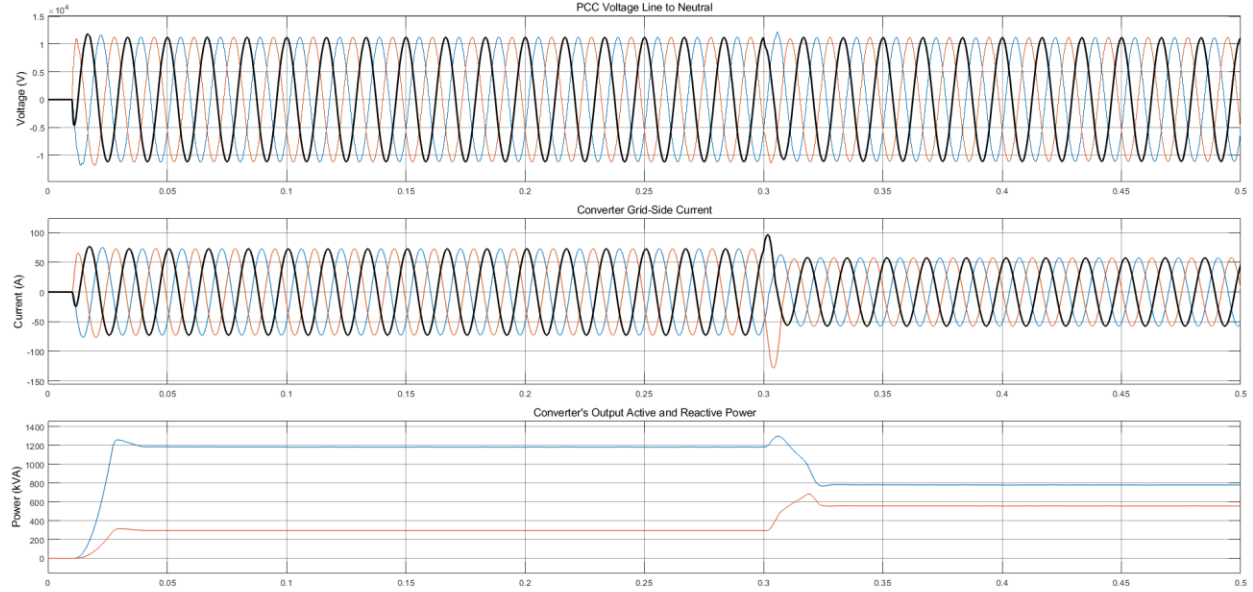


Figure 4.9: Grid-forming simulation results

The grid-forming converter provides the right frequency and voltage with good power quality to the load before $t = 0.3$ s. Then, the load is changed to demonstrate the converter's performance to changes in the load while providing the right voltage. The waveforms above in Fig. 4.9, shows that the disturbance produced by the load change has been dealt with in half a fundamental cycle, and the voltage returns to its regular quality. The converter's output power shows that the converter provides the necessary power to the load in order to regulate the frequency and voltage as it can be seen in the control diagram of Fig. 4.7 where the outer loop varies the current references to the required values to maintain the desired AC voltage reference.

4.4 Grid-Supporting Mode

The active load sharing method provides tight current sharing and high-power quality; however, it requires communication links and high bandwidth control loops. Alternatively, the droop methods provide local controls without any communication infrastructures. The implementation of these droop loops in the control diagrams shown in previous sections is known as the grid-supporting mode that can be divided into two implementations: current source

and voltage source. The current source grid-supporting mode can be used for frequency and voltage regulation at the point where this converter is connected. The voltage source grid-supporting mode is used to share a load among parallel converters based on each converter's power rating.

Considering the case shown in Fig. 4.10 where a voltage source, \vec{E}_{Vs} , is connected to the PCC, \vec{V}_{PCC} , through a line impedance, \vec{Z}_{LINE} , the complex power transfer equation can be derived:

$$\vec{S}_{Vs} = \vec{E}_{Vs} \times \vec{I}_{LINE}^* = \vec{E}_{Vs} \times \left(\frac{\vec{E}_{Vs} - \vec{V}_{PCC}}{\vec{Z}_{LINE}} \right) \quad (3.1)$$

Converting (3.1) to its equivalent complex form yields:

$$\vec{S} = E_{Vs} e^{j\delta} \times \left(\frac{E_{Vs} e^{-j\delta} - V_{PCC}}{Z_{LINE} e^{-j\theta}} \right) = \frac{E_{Vs}^2}{Z_{LINE}} e^{j\theta} - \frac{V_{PCC} E_{Vs}}{Z_{LINE}} e^{j(\delta+\theta)} \quad (3.2)$$

Separating (3.2) into active and reactive power equations as follows:

$$\begin{aligned} P_{Vs} &= \frac{E_{Vs}^2}{Z_{LINE}} \cos \theta - \frac{V_{PCC} E_{Vs}}{Z} \cos(\delta + \theta) \\ Q_{Vs} &= \frac{E_{Vs}^2}{Z_{LINE}} \sin \theta - \frac{V_{PCC} E_{Vs}}{Z_{LINE}} \sin(\delta + \theta) \end{aligned} \quad (3.3)$$

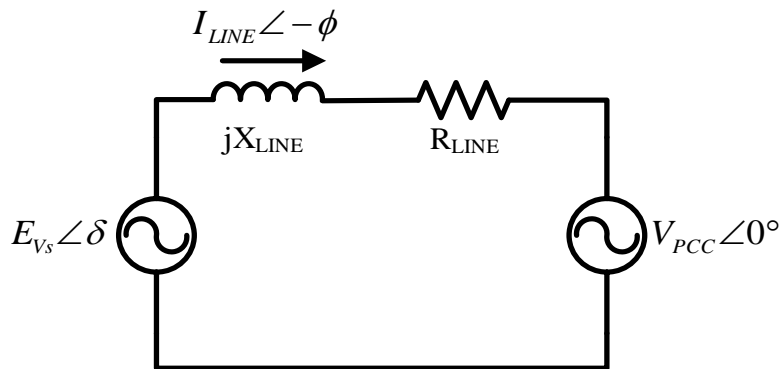


Figure 4.10: Equivalent circuit of an inverter connected to a common AC bus

Since $R_{LINE} = Z_{LINE} \cos \theta$ and $X_{LINE} = Z_{LINE} \sin \theta$, (3.3) becomes,

$$\begin{aligned} P_{Vs} &= \frac{E_{Vs}^2}{R_{LINE}^2 + X_{LINE}^2} \left[R_{LINE} (E_{Vs} - V_{PCC} \cos \delta) + X_{LINE} V_{PCC} \sin \delta \right] \\ Q_{Vs} &= \frac{E_{Vs}^2}{R_{LINE}^2 + X_{LINE}^2} \left[-R_{LINE} V_{PCC} \sin \delta + X_{LINE} (E_{Vs} - V_{PCC} \cos \delta) \right] \end{aligned} \quad (3.4)$$

From (3.4) it can be concluded that the line impedance plays a significant role in the power transferred from source to load.

The main idea to support the droop control comes from mimicking the self-regulation capability of a synchronous generator in the grid-connection mode, increasing the injected active power when the grid frequency decreases and increasing the injected reactive power when the grid voltage magnitude decreases [4]. This relationship holds when the line impedance is mainly inductive like in the case of MV and HV networks which translates to neglecting the resistance term in (3.4) and assuming a very small power angle δ . Thus, leading to the following equations:

$$\begin{aligned} \delta &\approx \frac{X_{LINE}}{E_{Vs} V_{PCC}} P_{Vs} \\ E_{Vs} - V_{PCC} &\approx \frac{X_{LINE}}{E_{Vs}} Q_{Vs} \end{aligned} \quad (3.5)$$

Equation (3.5) shows direct relationships between the power angle and the active power as well as between the voltage difference and the reactive power. Therefore, the regulation of frequency and voltage in a mainly inductive network can be related to the equation below:

$$\begin{aligned} \omega - \omega^* &= -m(P_{Vs} - P^*) \\ E_{Vs} - E^* &= -n(Q_{Vs} - Q^*) \end{aligned} \quad (3.6)$$

where ω^* and E^* are the output AC voltage frequency and magnitude at no load, and m and n are the frequency and voltage droop coefficients, respectively.

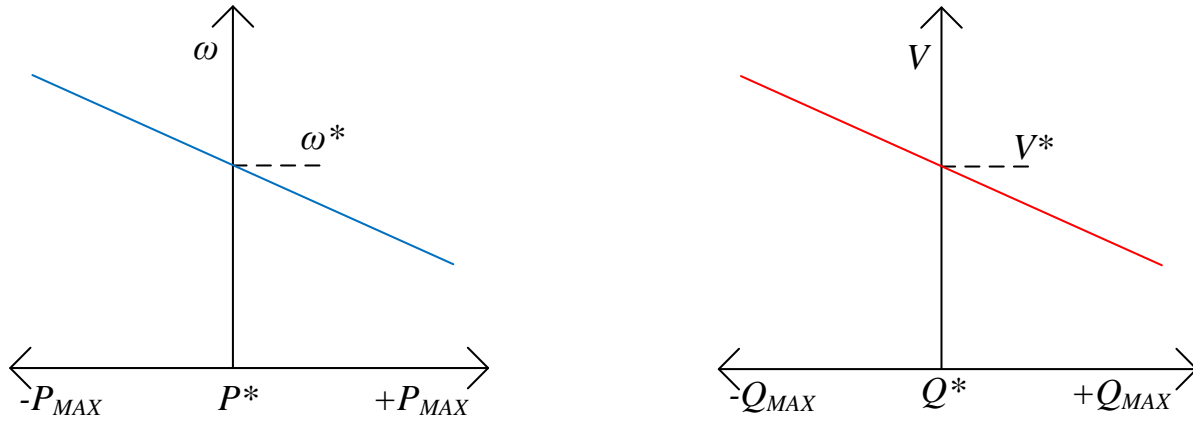


Figure 4.11: Frequency and voltage droop characteristics for inductive networks

The relationship shown in (3.6) is represented in the graphs shown in Fig. 4.11 where the droop characteristic behavior is inductive, and the droop coefficients m and n represent the slope of the droop lines. Moreover, the contribution of each grid-supporting power converter in the regulation of the frequency and voltage magnitude alone can be adjusted by changing the individual droop coefficients.

4.4.1 Current Source

The voltage quality in a microgrid does not exclusively depend on the performance of the grid-forming converter because the connection of loads and other DERs to the microgrid distribution lines can modify substantially the voltage profile along the microgrid. Therefore, the presence of current source grid-supporting converters contributes positively to improve the voltage quality along the microgrid distribution lines, in both grid-connected and island modes. The control diagram of the grid-supporting as a current source is very similar to the one of the grid-feeding with only the addition of a droop control loop as presented in Fig. 4.12.

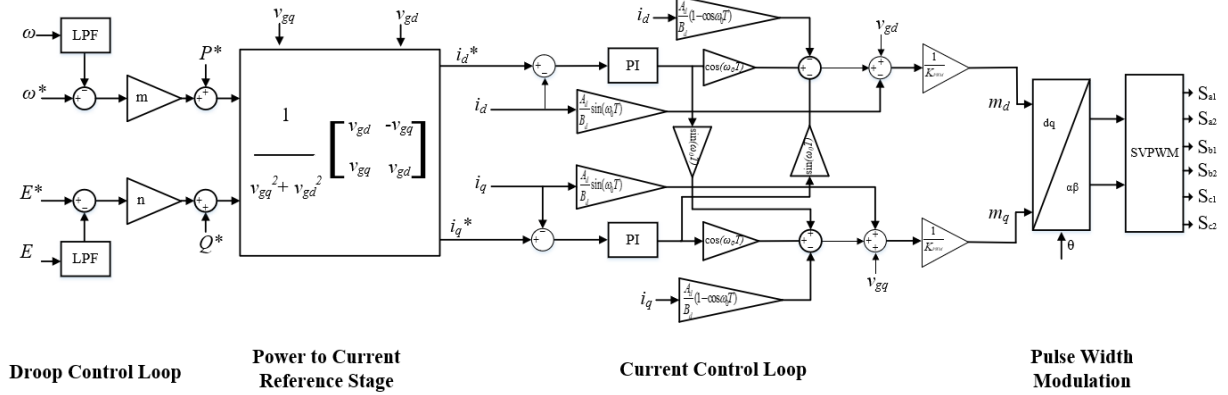


Figure 4.12: Grid-supporting as current source control diagram

The droop control is constituted by the following steps: the system frequency is measured with a PLL, then it is compared with a reference value and the frequency deviation is filtered using a low-pass filter (LPF) and multiplied by a gain constant [9]. The bandwidth of the LPF must be much slower than that of the current controller so that the reference current does not changes too fast for the current controller to handle just as in the cascade-loop control implementation. A simulation is not presented in this section because an appropriate scenario for this control mode will be developed in section 4.5.

4.4.2 Voltage Source

When the microgrid enters into emergency island mode due to a utility supply contingency, one grid-forming converter might not have the capabilities to maintain the frequency and voltage within the required margins. Therefore, multiple converters need to work together to supply the load in this emergency condition. According to the authors of [2], it is not possible to connect multiple grid-forming units with the predefined reference voltage to a single network; grid-supporting converters operating as voltage sources must be deployed to share the

microgrid load to maintain the frequency and voltage of the microgrid without needing any kind of communication with other converters or with the central controller. However, the conventional droop technique presented above has an inherent tradeoff between load sharing accuracy and frequency/magnitude output-voltage regulation, and consequently is not enough for this task [10]. Moreover, high circulating currents may be caused by power angle and voltage deviations between converters and may exceed the rated currents of the converters [11]. From (3.5), it should be noted that active and reactive powers of the converter are not only affected by the output-voltage magnitude and frequency but also by the system's impedance. Therefore, the high circulating currents can be diminished by increasing the output impedance of the converter and the network characteristics can also be altered. The use of large inductors between parallel converters will reduce the coupling between converters but the high voltage drop of this passive technique will render this solution not efficient [1]. Nevertheless, the implementation of this high impedance can be done actively by adapting the control loop of the grid-supporting converters in order to include this effect with a technique called virtual output impedance which does not incurs power losses.

The virtual output impedance should be larger than the combined values of the converter's output and the maximum power line impedance [4]. This way, the total equivalent output impedance is mainly dominated by this control variable. The implementation of the virtual output impedance can be performed by using the following equation:

$$v_{ref} = v_{ref}^* - Z_V(z) \cdot i_o \quad (3.7)$$

where $Z_V(z)$ is the transfer function of the virtual output impedance, v_{ref}^* is the voltage reference calculated by the P/Q sharing droop loop, and v_{ref} is the modified output voltage reference provided to the voltage control loop as shown in Fig. 13

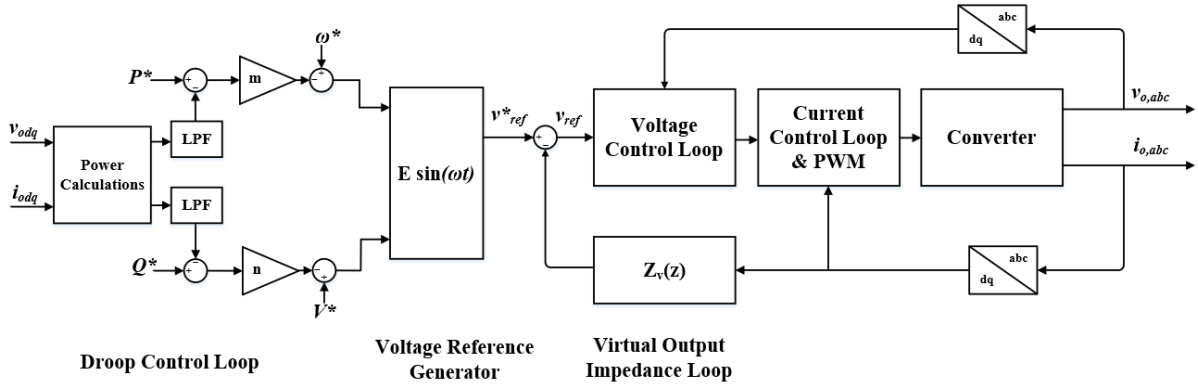


Figure 4.13: Grid-supporting as voltage source control diagram

For the control of multiple grid-supporting converters in parallel, control variables such as droop coefficients and virtual output impedances should be selected according to the nominal power of each converter utilizing the following relationships [12]:

For the P/Q sharing droop loop:

$$\begin{aligned} m_1 S_1 &= m_2 S_2 = \dots = m_N S_N \\ n_1 S_1 &= n_2 S_2 = \dots = n_N S_N \end{aligned} \quad (3.8)$$

where the m is the frequency droop coefficient and n is voltage magnitude droop coefficient. For the virtual impedance loop:

$$Z_{V1} S_1 = Z_{V2} S_2 = \dots = Z_{VN} S_N \quad (3.9)$$

where the Z_v is the virtual output impedance and S_N is the apparent power of converter N.

The simulation model shown in Fig. 4.14 consists of two converters in grid-supporting mode representing two UPSs in parallel that share a load without communication links when the microgrid is in island mode. Therefore, the control diagram in Fig. 4.13 has been implemented in the simulation following the equations (3.8) and (3.9) because these converters have different power ratings.

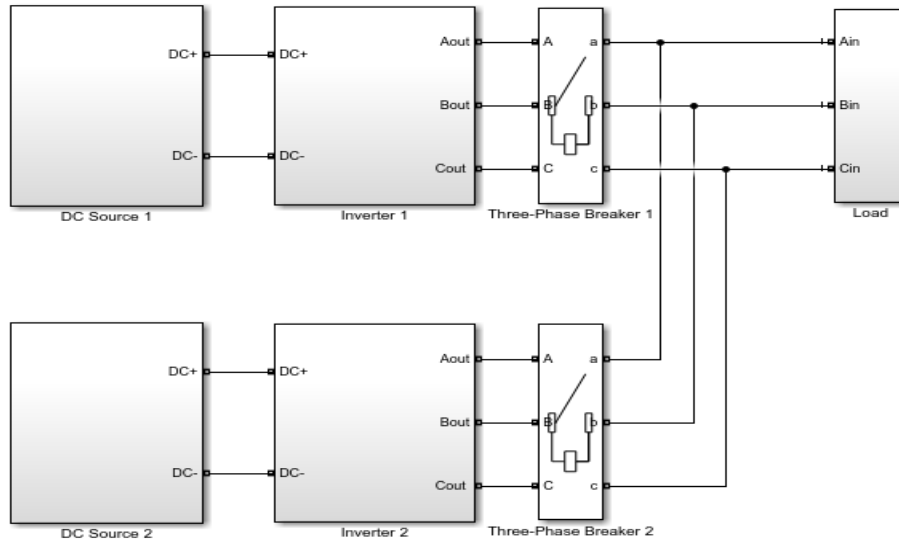


Figure 4.14: Grid-supporting as voltage sources Simulink model

The parameters for this test are presented in Table 4.5 where it can be highlighted that each inverter has different LC filter parameters and power ratings. However, they have been given the same time constant for their control loops as well as switching frequency.

Table 4.5 Test Parameters for the load sharing simulation

Parameter	Symbol	Value
Inverter Rated Output Voltage	V_o	480 V
DC Link Capacitor Voltage	V_{DC}	750 V
Inverter 1 Rated Power	S_{1B}	2 MVA
Inverter 2 Rated Power	S_{1B}	1 MVA
Fundamental Frequency	f_B	60 Hz
Switching Frequency	f_s	4 kHz
Controller Sampling Frequency	f_{smp}	8 kHz
AC Filter Capacitor Delta Connection	C_f	480 μ F
AC Filter Capacitor ESR	RC_f	0.2 m Ω
AC Filter Inductor Converter-Side	L_{fl}	46 μ H
Filter Resistance	R_f	1.6 m Ω
Current control Loop Time constant	τ_i	198 μ s
Inverter 1 Frequency Droop Coefficient	$m1$	3.769e-06
Inverter 1 Voltage Droop Coefficient	$n1$	4.8e-06
Inverter 2 Frequency Droop Coefficient	$m2$	7.534e-06
Inverter 2 Voltage Droop Coefficient	$n2$	9.6e-06
Load Active Power	P_L	500 kW
Load Reactive Power	Q_L	500 kVAR

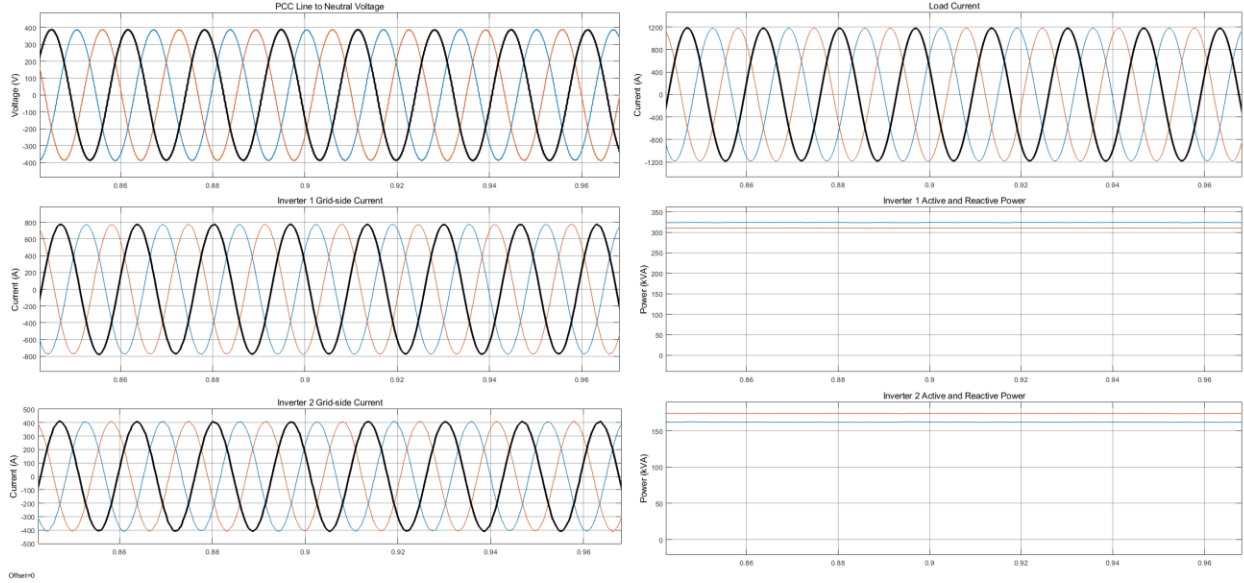


Figure 4.15: Load sharing simulation results

The grid-supporting converter share the load with respect to their power ratings and maintain the required frequency and voltage magnitude. Since the power rating of inverter 1 is twice that of inverter 2, inverter 1 provides around 340 kW and 330 kVARs to the load while inverter 2 is in charge of around 160 kW and 170 kVARs as shown in Fig 4.15. In this way, $2/3$ of the power absorbed by the load will be supplied by Inverter 1 and $1/3$ by Inverter 2 and the load sharing is achieved without any communication links between the converters. This simulation of two parallel converters can be extended to more in parallel and in different locations along the microgrid.

4.5 Volt-VAR Control

The regulation of the voltage profile along the microgrid is one the responsibilities of the secondary controller to ensure proper operation and microgrid reliability. In grid-connected mode the frequency variations are taken care of by the utility itself and the secondary control performs voltage regulation to address adverse issues, due to the line impedance or reactive

power oscillation produced the large numbers of inverters without proper voltage control coordination [11]. Therefore, the secondary control sets the reference voltage value to each grid-supporting converter and the reactive power reference to each grid-feeding converter based on their location in the microgrid. As a result, the secondary controller implements the Volt-VAR control to adjust the measured voltage to the acceptable range of the reference point determined for that converter based in its location in the microgrid. This Volt-VAR control technique consists on increasing or decreasing the value of the amount of reactive power delivered by a converter until the measured voltage reaches the acceptable range or its maximum capacity. The following figure illustrates the changes in the reactive power reference as the measured voltage varies, the maximum voltage deviation limits and the acceptable voltage range which lies within the upper and lower desired voltage limits (V_b & V_c) [13].

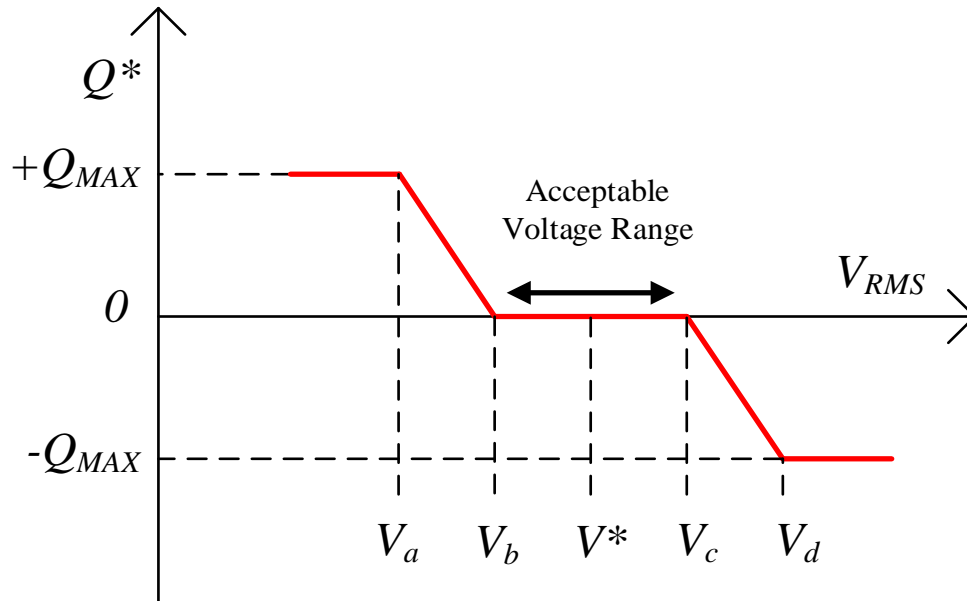


Figure 4.16: Volt/VAR control graph [13]

Table 4.6 Volt/VAR algorithm process

Case	Reactive Power Reference	Saturation $ Q[k] > Q_{MAX}$
$V^* < V_a$	Q_{MAX}	$Q[k] = Q_{MAX}$
$V_a > V^* < V_b$	$Q[k] = Q[k-1] + \Delta Q$	$Q[k] = Q_{MAX}$
$V_b \geq V^* \geq V_c$	$Q[k] = Q[k-1]$	N/A
$V_c > V^* < V_d$	$Q[k] = Q[k-1] - \Delta Q$	$Q[k] = -Q_{MAX}$
$V^* > V_d$	$-Q_{MAX}$	$Q[k] = -Q_{MAX}$

The Volt/VAR algorithm executed by the secondary controller is summarized in the Table 4.6 to determine the reactive power reference sent to the grid-feeding converter.

A case of Volt-VAR control regarding one grid-feeding converter in a simplified radial distribution feeder with balance loads and a line impedance to show a voltage drop at bus 2 from the nominal voltage at bus 1 is developed in this section as depicted in Fig 4.17 for simplicity purposes. This model comprises of a three-phase voltage source and a utility transformer that represent the power substation of a distribution feeder, a fixed load at bus 1 and a changing load at bus 2 to represent the normal, heavy and light loading conditions experienced in a distribution feeder which leads to different voltage drops due to the line impedance.

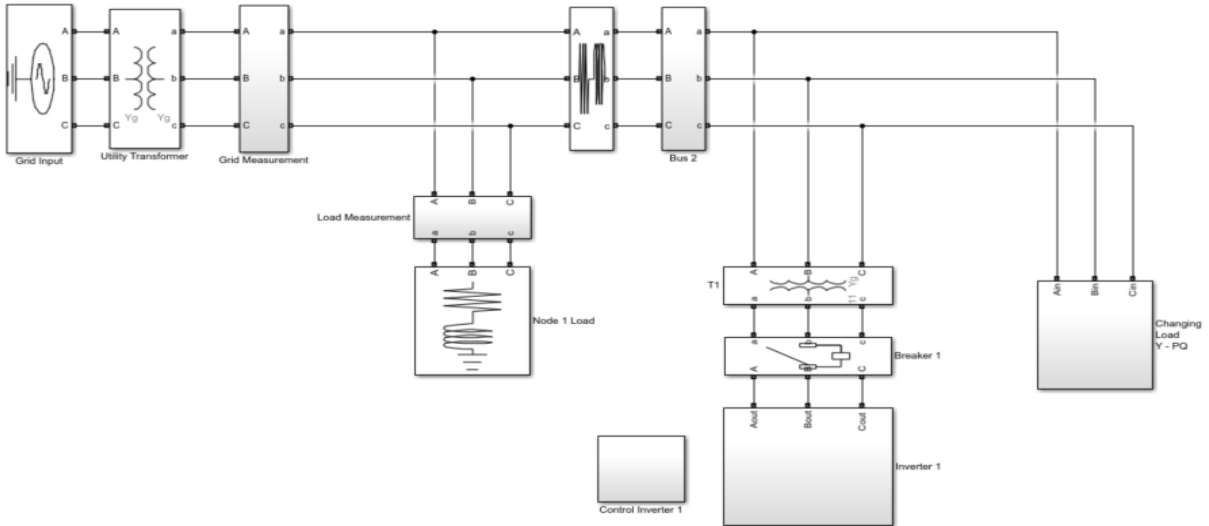


Figure 4.17: Volt/VAR control simulation model

The nominal line-to-line voltage of this test was set to 12.47 kV, and the maximum power that could be delivered by the inverter was 2 MVA. Utilizing these parameters, the upper and lower desired voltage limits (V_b , V_c) were set to be within 1% of the nominal voltage value for simplicity sake. Additionally, the maximum magnitude of Q to be delivered is designated as 40% of the maximum inverter power, 800 kVAR which is a realistic magnitude limit since delivering Q to a grid is not profitable. The following table describes the values chosen for the Volt/VAR controller implemented in MATLAB/SimulinkTM including the power references for the inverter and PQ load values for different conditions.

The simulation consisted of a series of events at different times to fully show the concept of inverter-based Volt-VAR control. At the start of the simulation, the fixed load P_{B1} , Q_{B1} , and the changing load that has the value P_{L1} , Q_{L1} , this represents normal conditions. It can be seen from the first interval 1 in Fig. 4.18 the loads are supplied solely by the grid and the voltage remains inside the desired range.

Table 4.7 Test parameters for the Volt/VAR control simulation

Parameter	Symbol	Value
Grid Voltage	V_{PCC}	12.47 kV
Inverter Rated Power	S_B	2 MVA
Fundamental Frequency	f_B	60 Hz
Current Loop Proportional Gain	K_{pcd}	0.0689
Current Loop Integral Gain	K_{icd}	2.7060
Desired Voltage Range	D	$0.01 * V_{PCC}$
Reactive Reference Change	ΔQ	$0.008 * S_B$
Inverter Active Power Reference	P_1	500 kW
Inverter Reactive Power Reference	Q_1	0 VAR
Load at Bus 1 Active Power	P_{B1}	900 kW
Load at Bus 1 Reactive Power	Q_{B1}	400 kVAR
Normal Load Active Power	P_{L1}	300 kW
Normal Load Reactive Power	Q_{L1}	200 kVAR
Heavy Load Active Power	P_{L2}	1500 kW
Heavy Load Reactive Power	Q_{L2}	1000 kVAR
Light Load Active Power	P_{L3}	300 kW
Light Load Reactive Power	Q_{L3}	-500 kVAR

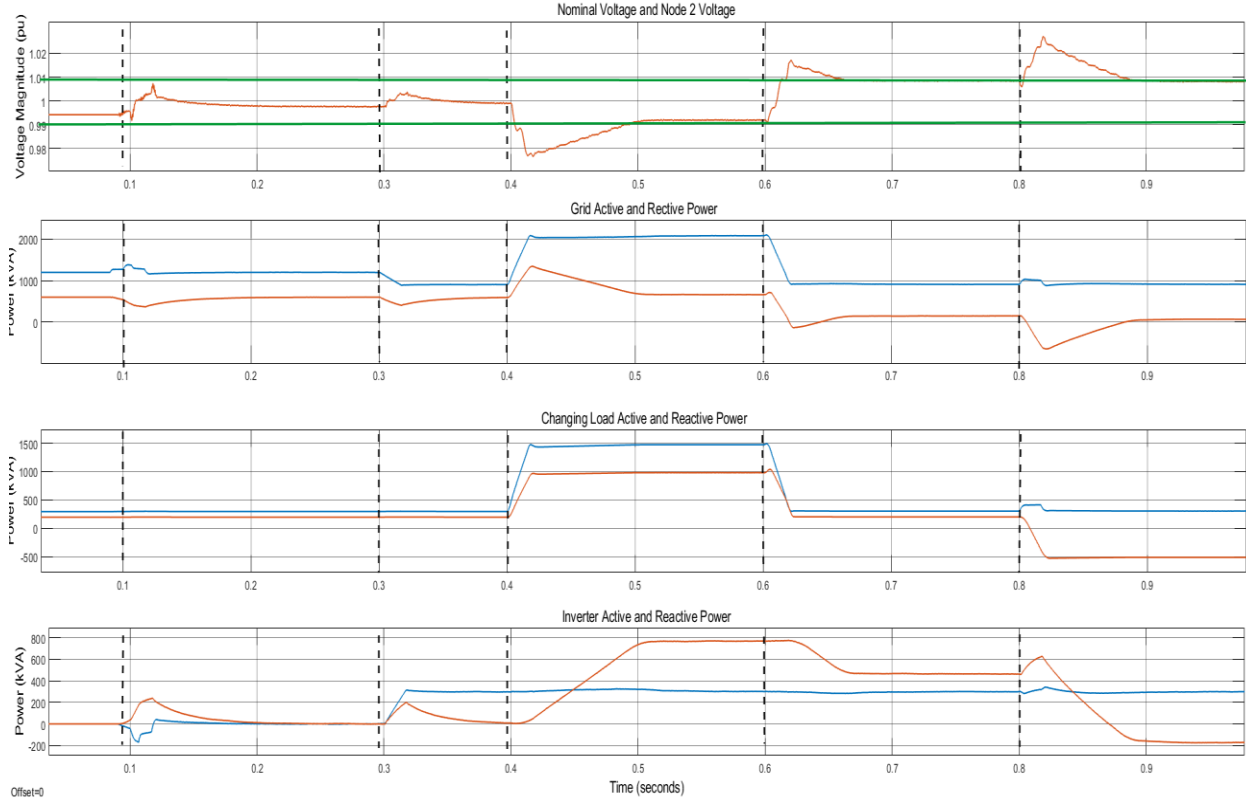


Figure 4.18: Volt/VAR control simulation results

At $t = 0.09$ s, the inverter is connected to the grid and given a reference of PQ of zero so that the effect of Volt/VAR control can be seen in the next interval. At $t = 0.3$ s the active power reference of the inverter is set to 300 kW, so it mimics a DER injecting power to the grid. The Volt/VAR control was started but the reactive power reference remained at zero since the bus 2 voltage was still inside the desired limit. At $t = 0.4$ s the load was switched to P_{L2} , Q_{L2} so that a heavy loading condition of the distribution feeder was experienced and the voltage at bus 2 dropped below the desired limit. Shortly after this load change, the reference of the reactive power was increased by the Volt/VAR controller to return the voltage to the desired limit. At $t = 0.6$ s the load was changed back to the normal loading conditions as a transition interval prior to the light loading condition, leading to slight decrease in the reactive power. At $t = 0.8$ s the load was changed to P_{L3} , Q_{L3} which in this case had a negative reactive power which corresponded to

a RC load. This load was selected because a capacitive load injects VARs and increases the voltage which is a similar result to the one produced by the over generation of DERs in light loading conditions. Since the Volt/VAR controller only checks for the voltage at bus 2, increasing the voltage by a reactive load instead of many DERs injecting active power was a better option due to simplicity of the model and computation time. Consequently, the Volt/VAR controller kept decreasing the reactive power reference of the inverter to a negative value until the voltage was brought back to the desired limit. Thus, the voltage is maintained within the acceptable voltage range for all loading conditions.

4.6 Concluding Remarks

This chapter reviewed the definition and implementation of the several primary control modes for different microgrid scenarios such as grid-connected and island mode. Moreover, a secondary control strategy was explained and implemented to illustrate voltage regulation in a distribution-level microgrid with MV lines. As a result, the necessary tools were presented to develop a complex microgrid with several DERs interfaced with converters operating under different modes to fulfill specific functions such as injecting the maximum power to the grid, regulating the frequency and voltage, or even load sharing without any communications links.

Subsequently, the next chapter will make use of the converter modes presented in this chapter to develop a microgrid case with several DERs so that a tertiary control can be employed in grid-connected mode.

4.7 References

- [1] J. Rocabert, A. Luna, F. Blaabjerg and P. Rodríguez, "Control of Power Converters in AC Microgrids," in *IEEE Transactions on Power Electronics*, vol. 27, no. 11, pp. 4734-4749, Nov. 2012.
- [2] T. L. Vandoorn, J. C. Vasquez, J. De Kooning, J. M. Guerrero and L. Vandevelde, "Microgrids: Hierarchical Control and an Overview of the Control and Reserve Management Strategies," in *IEEE Industrial Electronics Magazine*, vol. 7, no. 4, pp. 42-55, Dec. 2013.
- [3] A. Bidram and A. Davoudi, "Hierarchical Structure of Microgrids Control System," in *IEEE Transactions on Smart Grid*, vol. 3, no. 4, pp. 1963-1976, Dec. 2012.
- [4] J. M. Guerrero, J. C. Vasquez, J. Matas, L. G. de Vicuna and M. Castilla, "Hierarchical Control of Droop-Controlled AC and DC Microgrids—A General Approach Toward Standardization," in *IEEE Transactions on Industrial Electronics*, vol. 58, no. 1, pp. 158-172, Jan. 2011.
- [5] T. Esram and P. L. Chapman, "Comparison of Photovoltaic Array Maximum Power Point Tracking Techniques," in *IEEE Transactions on Energy Conversion*, vol. 22, no. 2, pp. 439-449, June 2007.
- [6] N. Femia, G. Petrone, G. Spagnuolo and M. Vitelli, "Optimization of perturb and observe maximum power point tracking method," in *IEEE Transactions on Power Electronics*, vol. 20, no. 4, pp. 963-973, July 2005.
- [7] K. L. Lian, J. H. Jhang and I. S. Tian, "A Maximum Power Point Tracking Method Based on Perturb-and-Observe Combined With Particle Swarm Optimization," in *IEEE Journal of Photovoltaics*, vol. 4, no. 2, pp. 626-633, March 2014.
- [8] H. M. A. Antunes, S. M. Silva, D. I. Brandao, R. V. Ferreira and B. d. J. C. Filho, "Analysis of a grid-forming converter based on repetitive control in centralized AC microgrid," 2017 *IEEE 8th International Symposium on Power Electronics for Distributed Generation Systems (PEDG)*, Florianopolis, 2017, pp. 1-8.
- [9] Nikos Hatziargyriou, "Intelligent Local Controllers," in *Microgrids: Architectures and Control*, IEEE, 2014.
- [10] J. M. Guerrero, J. Matas, L. Garcia De Vicunagarcia De Vicuna, M. Castilla and J. Miret, "Wireless-Control Strategy for Parallel Operation of Distributed-Generation Inverters," in *IEEE Transactions on Industrial Electronics*, vol. 53, no. 5, pp. 1461-1470, Oct. 2006.
- [11] S. Chowdhury, S. P. Chowdhury and P. Crossley, "Chapter 4: Microgrid and active distribution network management system," in *Microgrids and active distribution networks*, London: Institution of Engineering and Technology, 2009.

- [12] J. M. Guerrero, L. Hang and J. Uceda, "Control of Distributed Uninterruptible Power Supply Systems," in *IEEE Transactions on Industrial Electronics*, vol. 55, no. 8, pp. 2845-2859, Aug. 2008.
- [13] P. Jahangiri and D. Aliprantis, "Distributed Volt/VAr control by PV inverters," *2014 IEEE PES General Meeting | Conference & Exposition*, National Harbor, MD, 2014, pp. 1-1.

CHAPTER 5

MICROGRID CENTRAL CONTROLLER

5.1 Introduction

A hierarchical control structure is key to govern a complex microgrid as a single entity that can interact with the current electrical network and aid the transition to the smart grid. The implementation of this control structure is separated into two types of controllers: a central controller and local controllers [1-3]. The local controller manages the power flow of its respective DG unit autonomously by implementing primary layer control techniques as the ones presented in Chapter 4, or by receiving commands from the central controller for power quality, economical optimization or protection purposes depending on the microgrid state and function. Consequently, the central controller executes the secondary and tertiary control layers as well as coordination of protection devices of the microgrid to ensure optimized, reliable operation against different demand and generation conditions, and proper protection against grid faults and outages [4].

The central controller constitutes a SCADA interface that employs communications protocols and necessary sensors to obtain the corresponding measurements and relevant information from every DG unit, load and protection device to oversee the microgrid operation. The central controller is intended to work automatically with provision for manual intervention when necessary [5]. The main tasks of the central controller were presented in Chapter 1. A list of the main controller functions is presented as follows [6-7]:

- Monitoring system diagnostics by collecting information from DG units and loads.

- Frequency and voltage regulation at all points of the microgrid by adjusting active and reactive power references of the DG units.
- To detect islanding conditions based on measurements at the point of common coupling (PCC) and to execute grid resynchronization procedures.
- Perform economic scheduling, energy storage management and demand-side bidding having into consideration weather, load and generation forecasting, and present conditions.

This chapter presents an introduction to the tertiary control layer and a straightforward implementation of an application of this control layer as done in Chapter 4 for the secondary control layer. Thus, the necessary tools for the implementation of a more advanced microgrid structure are covered as introduced in Chapter 1 and this thesis can be used as a base for future microgrid control work.

5.2 Tertiary Control Layer

The tertiary controller makes use of the data obtained by the central controller to perform the economic optimization and energy management functions of the microgrid. This includes of the coordination of DG units, controllable loads and power flow with the main grid to fulfil the microgrid goals. The implementation of the economical dispatch can be divided into three steps: modeling of the microgrid, optimization problem formulation and optimization problem solution.

First, the modeling of the microgrid consists in representing the microgrid components cost considerations and technical constraints by using cost functions and formulas. For instance, the consideration of variables for the startup, operation, shut down, fuel and maintenance costs of a conventional generator. The consideration of renewable sources as non-dispatchable and

constraints associated with the energy storage systems storage maximum capacity, state of charge (SoC), charging and discharging rates and aging costs [8]. Moreover, the load demands are also modeled and classified in critical demands, which are the demand that need to be satisfied, curtailable demands, which are the ones that can be shed, and reschedulable demands, which are the ones that can be supplied at a later time [5].

Second, the optimization problem is formulated according to the market policies and goals assumed for the microgrid. Some of the policies include minimizing the microgrid operational costs to lower electricity prices for the microgrid end-users by determining the optimal generation output for each DG unit, SoC for every energy storage unit and power exchange with the main grid [9]; that is,

$$\min C = \sum_{k=1}^N \left[\sum_{i=1}^G F(P_i)_k + F(P_{grid})_k \right] + \sum_{j=1}^S [F(SoC_j)]_N \quad (5.10)$$

where N is the number of time steps, G is the number of DG units, S is the number of energy storage units, P_i is the power output from each DG unit, P_{grid} is the grid power transfer, and SoC is the energy storage state-of-charge, and F represents the corresponding cost functions. These individual cost functions may consider bidding, forecasting and the model considerations explained in the first step.

Another policy has the goal of maximizing profits for the microgrid by selling active power to both the grid and the microgrid end-users, and enabling demand-side bidding which allows each user to send bids for high- and low-priority loads. If the demand is higher than the production of the DG sources, power is bought from the grid and sold to the end-users of the microgrid to increase profits and cover at least the critical demand [10]; for example,

$$profit = A \sum_{i=1}^G P_i - \sum_{i=1}^G F(P_i) - \sum_{j=1}^L F(P_{Lj}) \quad (5.11)$$

where G is the number of DG units, L is the number of loads, P_i is the power output of each DG unit, A is the open market price of electricity, and F represents the corresponding cost functions.

Furthermore, the constraints policies have an effect in the optimization procedure. These constraints include the power limits of the DG units (5.3), SOC thresholds of the energy storage unit (5.4) and microgrid power balance between supply and demand in the microgrid (5.5) [9].

$$P_i^{\min} \leq P_i \leq P_i^{\max} \quad (5.12)$$

$$SoC_j^{\min} \leq SoC_j \leq SoC_j^{\max} \quad (5.13)$$

$$\sum_{i=1}^G (P_i)_k + (P_{grid})_k + \sum_{j=1}^S (P_{Sj})_k - (P_{loss})_k = L_k \quad (5.14)$$

Last, the tertiary controller solves the respective constrained optimization problem using real-time optimization techniques such as day-ahead economic scheduler [8], real-time economic dispatch and complementary quadratic programming [9], or heuristic approaches like particle swarm optimization [12] and ant colony optimization [13], among other artificial intelligence methods. The implementation of these optimization techniques is out of the scope of this thesis.

5.3 Central Controller Implementation

A real-time simulation tool is selected to implement the central controller for a microgrid because the response time is in the range of minutes. Typhoon Hardware-in-the-loop (HIL) has been selected because it allows controller HIL testing by allowing power-converter control through its digital signal processor (DSP) interface card [14-15]. Moreover, Typhoon HIL software toolchain features a SCADA panel that is essential to monitor microgrid operations and send commands to the local controllers.



Figure 5.1: Typhoon HIL setup for controller HIL testing

The primary controller of each DG unit is implemented by the TMS320F28335 DSP that acts as the local controller; please refer to [16] for an implementation of the primary controller. The power converters and loads are simulated in real time by the Typhoon HIL 602+ device. The central controller is run by the SCADA interface of the Typhoon HIL software that sends commands through serial communication to the DSP of the energy storage unit to charge and discharge the battery.

For the case presented in this section the central controller has the goal of satisfying the demand with its own resources, reducing the power exchange with the main grid. The simulation model presented in Fig. 5.1 consists of a renewable resource-based DG unit which is non-dispatchable, the local demand is a critical load that needs to be supplied all the time and an energy storage unit that is in the grid-feeding mode and regulated by the central controller.

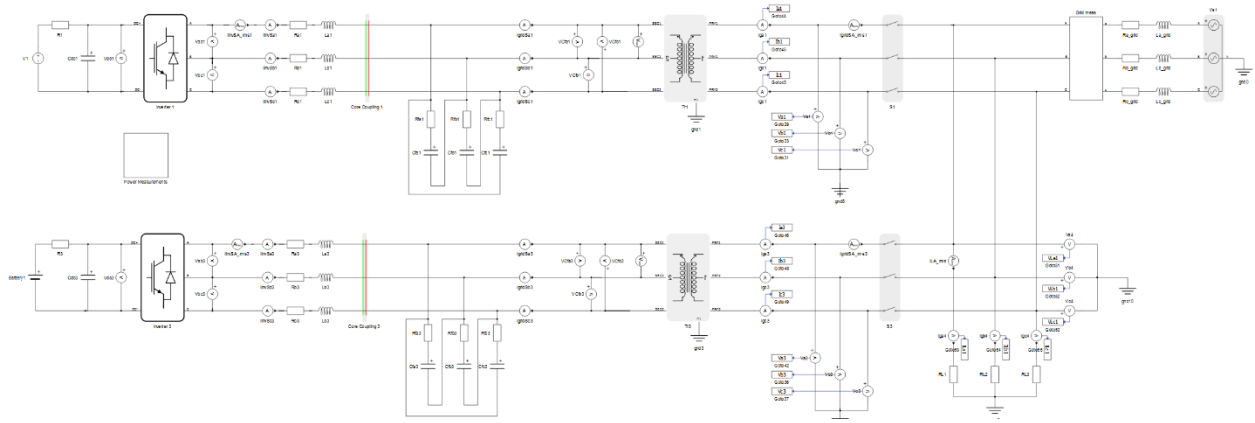


Figure 5.2: Typhoon HIL simulation model

The equation to determine the power reference command sent to the energy storage unit is given below:

$$P_{diff} = P_{inv1} - P_{L1} \quad (5.15)$$

Also, the constrain equation to guarantee good performance of the battery is defined as follows:

$$0.2 \text{ p.u.} \leq SoC_B \leq 1 \text{ p.u.} \quad (5.16)$$

On one hand, the lower limit was chosen to be 20% according to the Fig. 5.3 to ensure that the battery voltage was higher than the equivalent voltage of the grid voltage reference to the low-voltage side of the transformer in the discharging mode. On the other hand, the upper limit was chosen 100% so the battery can be charged to its rated capacity and not beyond which could shorten the battery life and degrade its performance. The flowchart in Fig. 5.4 depicts the energy storage management strategy implemented in the central controller for this simulation, considering (5.6) and (5.7). The test parameters for the components for the simulation are presented in the Table 5.1.

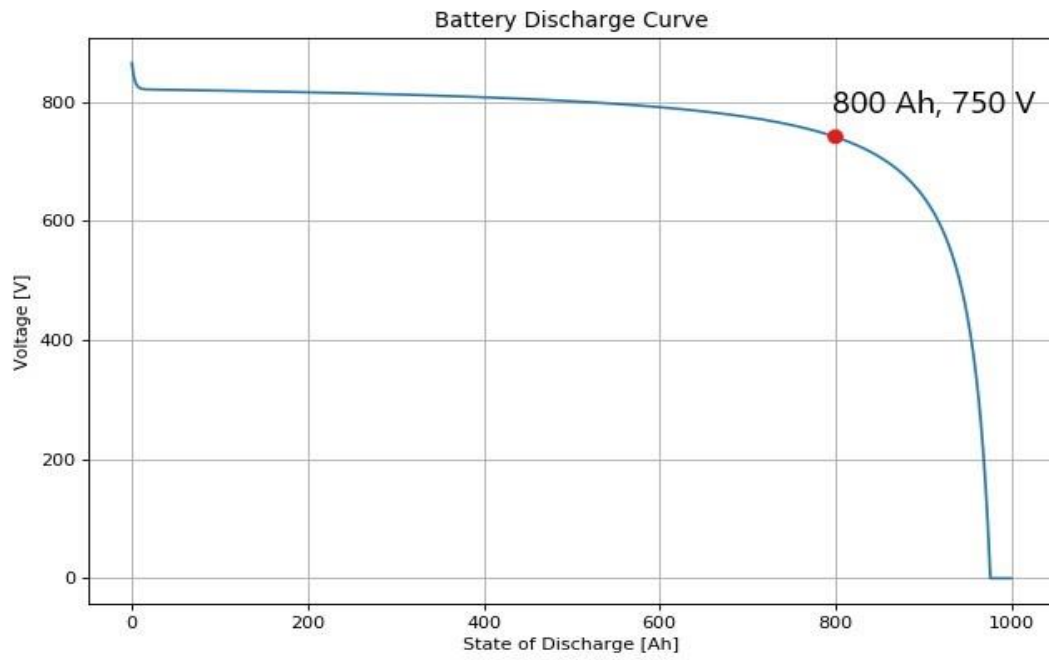


Figure 5.3: SoC curve of the energy storage unit

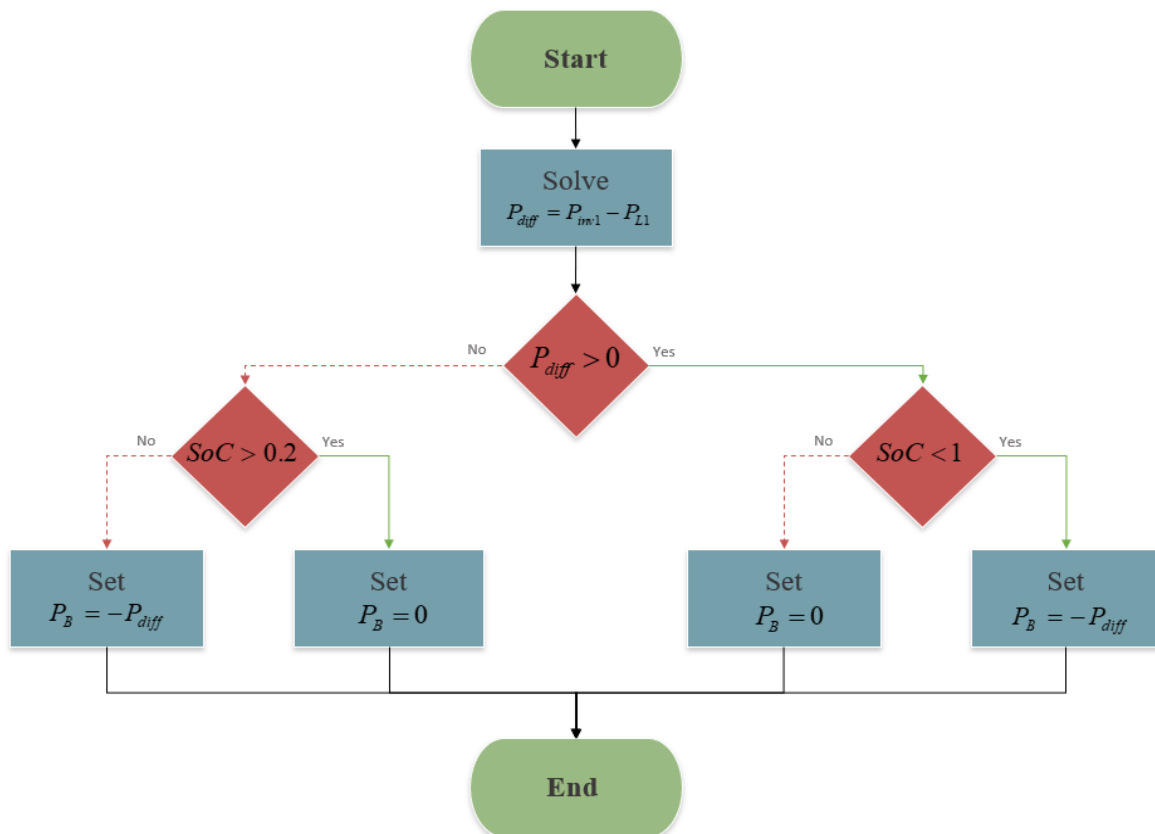


Figure 5.4: Flowchart of the energy storage management technique

Table 5.1 Test parameters for the HIL simulation

Parameter	Symbol	Value
Main Grid Line to Line Voltage	V_{PCC}	13.8 kV
Inverter Rated Output Voltage	V_o	480 V
DC Link Capacitor Voltage	V_{DC}	750 V
Battery Rated Voltage	V_{BR}	800 V
Battery Capacity	B_{Ah}	1000 Ah
Inverter Rated Power	S_B	2 MVA
Load Active and Reactive Power	P_{L1}, Q_{L1}	1 MW, 0 VAR
Fundamental Frequency	f_B	60 Hz
Switching Frequency	f_s	4 kHz
Controller Sampling Frequency	f_{samp}	8 kHz
DC-Link Capacitor	C_{DC}	37.8 mF
AC Filter Capacitor Delta Connection	C_f	480 μ F
AC Filter Capacitor ESR	RC_f	0.2 m Ω
AC Filter Inductor Converter-Side	L_{f1}	46 μ H
AC Filter Inductor Converter-Side ESR	RL_{f1}	1.6 m Ω
Transformer Equivalent Series Inductance	L_{f2}	13 μ H
Transformer Equivalent Series Resistance	RL_{f2}	0.26 m Ω
Current Loop Proportional Gain	K_{pcd}	0.0689
Current Loop Integral Gain	K_{icd}	2.7060
PLL Settling Time	T_{s_PLL}	30 ms

The SCADA panel that represent the main interface of the central controller is presented in the figure below. All the basic components such as measurements meters, measurement display tabs, command tabs, scopes and real time graphs are integrated in the HIL SCADA panel of the Typhoon software. The energy storage management technique is deployed from this interface and a set of slider widgets are used to send power reference commands manually to the local controllers if needed. Moreover, the active and reactive power graphs show that when the renewable-based DG unit changes its power output, the energy management system regulates the power absorbed or delivered by the energy storage unit in order to minimize the power exchange with the main grid. In fact, the power meter readings show that less than 10% of the total power is traded with the main grid.

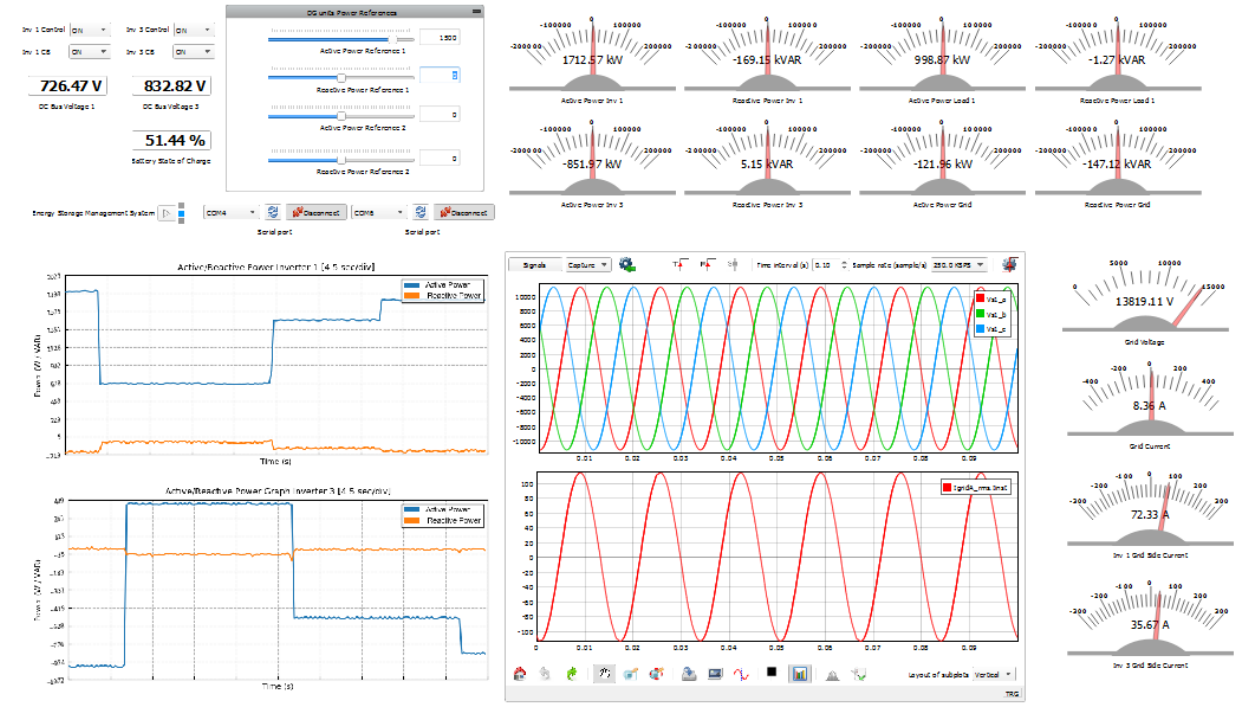


Figure 5.5: Typhoon HIL SCADA panel and simulation results

5.4 Concluding remarks

This chapter reviewed the definition and implementation of a basic central controller for AC microgrids using a real-time simulation tool. Moreover, this centralized approach optimizes the microgrid operation according to the desired goals and the collected data such as open market prices, demand-side bidding and forecasting from generation units and loads. This led to conclude that the central controller has the potential to see the bigger picture and coordinate generators considering present demands and anticipating future demands. However, one of the drawbacks is that the central controller represents a single point failure that is enough to stop the whole microgrid operation. Furthermore, a surge of microgrid participants increases the required computational load of the central controller as well as the number of communication and measurement channels. Hence, a decentralized approach might be a better solution in this regard [17-21].

5.5 References

- [1] T. L. Vandoorn, J. C. Vasquez, J. De Kooning, J. M. Guerrero and L. Vandevelde, "Microgrids: Hierarchical Control and an Overview of the Control and Reserve Management Strategies," in *IEEE Industrial Electronics Magazine*, vol. 7, no. 4, pp. 42-55, Dec. 2013.
- [2] F. Katiraei, R. Iravani, N. Hatziargyriou and A. Dimeas, "Microgrids management," in *IEEE Power and Energy Magazine*, vol. 6, no. 3, pp. 54-65, May-June 2008.
- [3] D. E. Olivares *et al.*, "Trends in Microgrid Control," in *IEEE Transactions on Smart Grid*, vol. 5, no. 4, pp. 1905-1919, July 2014.
- [4] A. G. Tsikalakis and N. D. Hatziargyriou, "Centralized control for optimizing microgrids operation," *2011 IEEE Power and Energy Society General Meeting*, San Diego, CA, 2011, pp. 1-8.
- [5] S. Chowdhury, S. P. Chowdhury and P. Crossley, "Chapter 4: Microgrid and active distribution network management system," in *Microgrids and active distribution networks*, London: Institution of Engineering and Technology, 2009.
- [6] S. Chowdhury, S. P. Chowdhury and P. Crossley, "Chapter 1: Distributed Generation and Microgrid Concept," in *Microgrids and active distribution networks*, London: Institution of Engineering and Technology, 2009.
- [7] M. Rasheduzzaman, S. N. Bhaskara and B. H. Chowdhury, "Implementation of a microgrid central controller in a laboratory microgrid network," *2012 North American Power Symposium (NAPS)*, Champaign, IL, 2012, pp. 1-6.
- [8] W. Hu, P. Wang and H. B. Gooi, "Toward Optimal Energy Management of Microgrids via Robust Two-Stage Optimization," in *IEEE Transactions on Smart Grid*, vol. 9, no. 2, pp. 1161-1174, March 2018.
- [9] D. McLarty, N. Panossian, F. Jabbari, and A. Traverso, "Dynamic economic dispatch using complementary quadratic programming," *Energy*, vol. 166, pp. 755–764, Oct. 2018.
- [10] Nikos Hatziargyriou, "Microgrids Control Issue," in *Microgrids: Architectures and Control*, IEEE, 2014.
- [11] A. Borghetti, M. Bosetti, C. Bossi, S. Massucco, E. Micolano, A. Morini, C. Nucci, M. Paolone, and F. Silvestro, "An energy resource scheduler implemented in the automatic management system of a microgrid test facility," in *Proc. IEEE International Conference on Clean Electrical Power (ICCEP '07)*, May 2007, pp. 94–100.
- [12] C. Colson, M. Nehrir, and S. Pourmousavi, "Towards real-time microgrid power management using computational intelligence methods," in *Proc. IEEE Power and Energy Society General Meeting*, July 2010, pp. 1–8.

- [13] C. Colson, M. Nehrir, and C. Wang, "Ant colony optimization for microgrid multi-objective power management," in *Proc. IEEE Power Systems Conference and Exposition (PSCE '09)*, Mar. 2009, pp. 1–7.
- [14] Typhoon HIL, "HIL602," *Hardware in the Loop 602 / Typhoon HIL*. [Online]. Available: <https://www.typhoon-hil.com/products/hil602>. [Accessed: 15-Apr-2019].
- [15] Typhoon HIL, "HIL uGrid DSP Interface," *Hardware in the Loop Microgrid DSP Interface / Typhoon HIL*. [Online]. Available: <https://www.typhoon-hil.com/products/hil-ugrid-dsp-interface>. [Accessed: 15-Apr-2019].
- [16] D. Carballo, "Stability Analysis of a High-Power Microgrid" (2018). MSEE Thesis, University of Arkansas.
- [17] D. McLarty, N. Panossian, F. Jabbari, and A. Traverso, "Dynamic economic dispatch using complementary quadratic programming," *Energy*, vol. 166, pp. 755–764, Oct. 2018.
- [18] K. De Brabandere, K. Vanthournout, J. Driesen, G. Deconinck and R. Belmans, "Control of Microgrids," *2007 IEEE Power Engineering Society General Meeting*, Tampa, FL, 2007, pp. 1-7.
- [19] A. Bani-Ahmed, A. Nasiri and H. Hosseini, "Design and development of a true decentralized control architecture for microgrid," *2016 IEEE Energy Conversion Congress and Exposition (ECCE)*, Milwaukee, WI, 2016, pp. 1-5.
- [20] J. M. Guerrero, M. Chandorkar, T. Lee and P. C. Loh, "Advanced Control Architectures for Intelligent Microgrids—Part I: Decentralized and Hierarchical Control," in *IEEE Transactions on Industrial Electronics*, vol. 60, no. 4, pp. 1254-1262, April 2013.
- [21] A. Vaccaro, V. Loia, G. Formato, P. Wall and V. Terzija, "A Self-Organizing Architecture for Decentralized Smart Microgrids Synchronization, Control, and Monitoring," in *IEEE Transactions on Industrial Informatics*, vol. 11, no. 1, pp. 289-298, Feb. 2015.

CHAPTER 6

CONCLUSIONS AND RECOMMENDATIONS FOR FUTURE WORK

6.1 Conclusions

Microgrids are playing an important role in the transition of passive traditional power systems to active and intelligent electric networks that integrate distributed generation as well as improve reliability and sustainability of the system. The control of these microgrids as single entities is a crucial factor to the realization of this great undertaking as explained in Chapter 1. Therefore, a hierarchical structure of the control of these microgrids is imperative to the distribution of tasks in the microgrid.

The control design of the PI controller in the z-domain and the step response comparison between the z- and s-domain implementations were demonstrated in Chapter 3. Consequently, the zero-order-hold discretization method was proven to be a valid and good approximation of the standard second-order transfer function time response. Besides, utilizing the gains derived in the s-domain in a discrete controller resulted in a satisfactory performance as long as the sampling frequency is high enough to approximate the discrete plant as a continuous plant. However, the discrete PI controller design implementation that accounts for changes in the sampling frequency works for all cases.

The application of the primary control strategies using the PI regulator for different AC microgrid applications presented in Chapter 4 rely heavily in the good performance of the PLL algorithm presented in Chapter 2. This makes the resiliency and robustness of this control strategy some of the most decisive factors for the operation of power converters in the DQ-reference frame.

The implementation of an energy storage management technique in the central controller led to conclude that communication and measurements channels that connect the SCADA panel and the local controllers are crucial for the operation of the microgrid as pointed out in Chapter 5. However, this approach makes the central controller a single point of failure to the whole microgrid operation and increases the computational load of the central controller as well as the number of communication and measurement channels when new microgrid components are integrated to the system. Hence, a decentralized architecture can be employed to overcome this potential vulnerability.

6.2 Recommendations for Future Work

The recommendations for future work are presented as follows:

- Explore the implementation of multi-level inverters to increase power efficiency and voltage output quality in microgrid applications as presented in [1-2].
- Investigate more advanced PWM techniques to optimize system efficiency such as a DPWM [3] and to reduce common-mode voltages such near-state PWM [4] and active zero-state PWM [5].
- Update the synchronous reference frame phase-lock-loop (PLL) presented in Chapter 2 with more advanced strategies such as the multiple reference frame PLL [6] and the dual second-order generalized integrator based PLL [7] which are more robust towards voltage unbalances and harmonics.
- Implement harmonic compensation techniques applicable to the PI-control loops designed in Chapter 3 such as PI controllers with multiple rotating integrators [8], PI with resonant regulators [9] and hybrid Fuzzy-PI controllers [10].

- Explore more advanced current and voltage control strategies for power converters such as proportional-resonant [11], deadbeat [12], and model predictive control [13].
- Apply a soft-start algorithm using the virtual-impedance method [14].
- Switch to more efficient and optimized maximum power point tracking techniques [15-16].
- Implement microgrid unbalance factor compensation in the secondary [17] and tertiary controllers [18].
- Investigate emergency energy reserves management techniques in the island mode as presented in [19] and economical dispatch optimization algorithms [20-21].
- Explore the option of the decentralized microgrid structure to increase system reliability even if communication is lost [22-25].

6.3 References

- [1] Haitham Abu-Rub; Mariusz Malinowski; Kamal Al-Haddad, "Multilevel Converter/Inverter Topologies and Applications," in *Power Electronics for Renewable Energy Systems, Transportation and Industrial Applications*, IEEE, 2014.
- [2] Euzeli dos Santos; Edison R. da Silva, "Power Electronics Converters Processing AC Voltage and Power Blocks Geometry," in *Advanced Power Electronics Converters: PWM Converters Processing AC Voltages*, IEEE, 2014.
- [3] I. P. Tsoumas and H. Tischmacher, "Influence of the Inverter's Modulation Technique on the Audible Noise of Electric Motors," in *IEEE Transactions on Industry Applications*, vol. 50, no. 1, pp. 269-278, Jan.-Feb. 2014.
- [4] E. Un and A. M. Hava, "A Near-State PWM Method With Reduced Switching Losses and Reduced Common-Mode Voltage for Three-Phase Voltage Source Inverters," in *IEEE Transactions on Industry Applications*, vol. 45, no. 2, pp. 782-793, March-april 2009.
- [5] Yen-Shin Lai, Po-Sheng Chen, Hsiang-Kuo Lee and J. Chou, "Optimal common-mode voltage reduction PWM technique for inverter control with consideration of the dead-

- time effects-part II: applications to IM drives with diode front end," in *IEEE Transactions on Industry Applications*, vol. 40, no. 6, pp. 1613-1620, Nov.-Dec. 2004.
- [6] P. Xiao, K. A. Corzine and G. K. Venayagamoorthy, "Multiple Reference Frame-Based Control of Three-Phase PWM Boost Rectifiers under Unbalanced and Distorted Input Conditions," in *IEEE Transactions on Power Electronics*, vol. 23, no. 4, pp. 2006-2017, July 2008.
 - [7] P. Rodríguez, R. Teodorescu, I. Candela, A. V. Timbus, M. Liserre and F. Blaabjerg, "New positive-sequence voltage detector for grid synchronization of power converters under faulty grid conditions," *2006 37th IEEE Power Electronics Specialists Conference*, Jeju, 2006, pp. 1-7.
 - [8] Remus Teodorescu; Marco Liserre; Pedro Rodriguez, "Grid Current Control," in *Grid Converters for Photovoltaic and Wind Power Systems*, , IEEE, 2007, pp.
 - [9] M. Liserre, R. Teodorescu and F. Blaabjerg, "Multiple harmonics control for three-phase grid converter systems with the use of PI-RES current controller in a rotating frame," in *IEEE Transactions on Power Electronics*, vol. 21, no. 3, pp. 836-841, May 2006.
 - [10] R. R. Nasyrov and R. I. Aljendy, "Comprehensive comparison between hybrid fuzzy-PI and PSO-PI controllers based active power filter for compensation of harmonics and reactive power under different load conditions," *2018 IEEE Conference of Russian Young Researchers in Electrical and Electronic Engineering (EIConRus)*, Moscow, 2018, pp. 725-730.
 - [11] Amirnaser Yazdani; Reza Iravani, " Grid-Imposed Frequency VSC System Control in $\alpha\beta$ -Frame," in *Voltage-Sourced Converters in Power Systems: Modeling, Control, and Applications*, , IEEE, 2010.
 - [12] Y. Abdel-Rady Ibrahim Mohamed and E. F. El-Saadany, "An Improved Deadbeat Current Control Scheme With a Novel Adaptive Self-Tuning Load Model for a Three-Phase PWM Voltage-Source Inverter," in *IEEE Transactions on Industrial Electronics*, vol. 54, no. 2, pp. 747-759, April 2007.
 - [13] Jose Rodriguez; Patricio Cortes, "Model Predictive Control," in *Predictive Control of Power Converters and Electrical Drives*, IEEE, 2012.
 - [14] J. M. Guerrero, J. C. Vasquez, J. Matas, L. G. de Vicuna and M. Castilla, "Hierarchical Control of Droop-Controlled AC and DC Microgrids—A General Approach Toward Standardization," in *IEEE Transactions on Industrial Electronics*, vol. 58, no. 1, pp. 158-172, Jan. 2011.
 - [15] N. Femia, G. Petrone, G. Spagnuolo and M. Vitelli, "Optimization of perturb and observe maximum power point tracking method," in *IEEE Transactions on Power Electronics*, vol. 20, no. 4, pp. 963-973, July 2005.

- [16] K. L. Lian, J. H. Jhang and I. S. Tian, "A Maximum Power Point Tracking Method Based on Perturb-and-Observe Combined With Particle Swarm Optimization," in *IEEE Journal of Photovoltaics*, vol. 4, no. 2, pp. 626-633, March 2014.
- [17] M. Savaghebi, A. Jalilian, J. C. Vasquez and J. M. Guerrero, "Secondary Control Scheme for Voltage Unbalance Compensation in an Islanded Droop-Controlled Microgrid," in *IEEE Transactions on Smart Grid*, vol. 3, no. 2, pp. 797-807, June 2012.
- [18] L. Meng, F. Tang, M. Savaghebi, J. C. Vasquez and J. M. Guerrero, "Tertiary Control of Voltage Unbalance Compensation for Optimal Power Quality in Islanded Microgrids," in *IEEE Transactions on Energy Conversion*, vol. 29, no. 4, pp. 802-815, Dec. 2014.
- [19] T. L. Vandoorn, J. C. Vasquez, J. De Kooning, J. M. Guerrero and L. Vandevelde, "Microgrids: Hierarchical Control and an Overview of the Control and Reserve Management Strategies," in *IEEE Industrial Electronics Magazine*, vol. 7, no. 4, pp. 42-55, Dec. 2013.
- [20] W. Hu, P. Wang and H. B. Gooi, "Toward Optimal Energy Management of Microgrids via Robust Two-Stage Optimization," in *IEEE Transactions on Smart Grid*, vol. 9, no. 2, pp. 1161-1174, March 2018.
- [21] D. McLarty, N. Panossian, F. Jabbari, and A. Traverso, "Dynamic economic dispatch using complementary quadratic programming," *Energy*, vol. 166, pp. 755–764, Oct. 2018.
- [22] K. De Brabandere, K. Vanthournout, J. Driesen, G. Deconinck and R. Belmans, "Control of Microgrids," *2007 IEEE Power Engineering Society General Meeting*, Tampa, FL, 2007, pp. 1-7.
- [23] A. Bani-Ahmed, A. Nasiri and H. Hosseini, "Design and development of a true decentralized control architecture for microgrid," *2016 IEEE Energy Conversion Congress and Exposition (ECCE)*, Milwaukee, WI, 2016, pp. 1-5.
- [24] J. M. Guerrero, M. Chandorkar, T. Lee and P. C. Loh, "Advanced Control Architectures for Intelligent Microgrids—Part I: Decentralized and Hierarchical Control," in *IEEE Transactions on Industrial Electronics*, vol. 60, no. 4, pp. 1254-1262, April 2013.
- [25] A. Vaccaro, V. Loia, G. Formato, P. Wall and V. Terzija, "A Self-Organizing Architecture for Decentralized Smart Microgrids Synchronization, Control, and Monitoring," in *IEEE Transactions on Industrial Informatics*, vol. 11, no. 1, pp. 289-298, Feb. 2015.